



2  
2009



This is to certify that the  
dissertation entitled

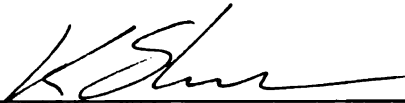
INTERMEDIATE-ENERGY PROTON KNOCKOUT TO  
PROBE SINGLE-PARTICLE STRUCTURE AND NUCLEAR  
SPIN ALIGNMENT IN THE "ISLAND OF INVERSION"  
ISOTOPES <sup>31,33</sup>MG

presented by

David Miller

has been accepted towards fulfillment  
of the requirements for the

Doctoral degree in Physics and Astronomy

  
\_\_\_\_\_

Major Professor's Signature

7/16/09

Date

**PLACE IN RETURN BOX** to remove this checkout from your record.  
**TO AVOID FINES** return on or before date due.  
**MAY BE RECALLED** with earlier due date if requested.

DATE DUE	DATE DUE	DATE DUE

INTERMEDIATE-ENERGY PROTON KNOCKOUT TO PROBE  
SINGLE-PARTICLE STRUCTURE AND NUCLEAR SPIN ALIGNMENT IN  
THE “ISLAND OF INVERSION” ISOTOPES  $^{31,33}\text{Mg}$

By

David Miller

A DISSERTATION

Submitted to  
Michigan State University  
in partial fulfillment of the requirements  
for the degree of

DOCTOR OF PHILOSOPHY

Physics and Astronomy

2009

## ABSTRACT

### INTERMEDIATE-ENERGY PROTON KNOCKOUT TO PROBE SINGLE-PARTICLE STRUCTURE AND NUCLEAR SPIN ALIGNMENT IN THE “ISLAND OF INVERSION” ISOTOPES $^{31,33}\text{Mg}$

By

David Miller

The “island of inversion” isotopes  $^{31,33}\text{Mg}$  were investigated through a proton-knockout reaction from  $^{32,34}\text{Al}$  at 90 MeV/u at National Superconducting Cyclotron Laboratory (NSCL). Single-particle states, with no neutron excitations across the  $N = 20$  shell gap from the  $sd$ -shell, were identified through the determination of the partial cross sections in the residue. The single-particle states identified lie above the ground state agreeing with the placement of these magnesium isotopes in the island of inversion.

Nuclear spin alignment is evident following the reaction as determined by the angular distribution of emitted gamma rays. Angular-distribution analysis constrained by the outgoing residue longitudinal momentum allows for the determination of multipolarity when combined with linear polarization measurements. Incorporating momentum constraints factors out possible systematic uncertainties of determining the in-beam gamma-ray detection efficiency. Development of digital data acquisition systems provides enhanced capabilities for angular distribution and linear polarization measurements. Instrumentation developed for the array of gamma-ray detectors (SeGA) at NSCL and considerations for next-generation gamma-ray detectors are discussed.

## ACKNOWLEDGMENT

I would like to personally thank the members of the committee for their guidance through my trek through the preparation of my thesis: Bill Lynch, Stuart Tesser, Vladimir Zelevinsky, Carl Schmidt, and especially my thesis advisor, Krzysztof Starosta. Their insight has kept me focused on the task at hand through the toilsome years of graduate school. I am also grateful to the support staff that made my experiment run smoothly, and to my fellow graduate students who sat shifts to obtain my data – especially to fellow member of Team Starosta, Phil. The analysis could not have been done without the work of other students who have went before me; Russ Terry’s thesis was particularly helpful in the writing process.

I have enjoyed the camaraderie and benefited from many of my peers. Working through hiccups in problem sets in the early years made things much more pleasant. I’ve had a host of wonderful officemates to provide additional input about lab-related issues, as well as proactively distract me. My fellow housemates at the Neutron Society have made the last couple years here more cheerful than I ever expected, and the crowd across several departments that mobilizes for Sunday evenings has also (generally) made those Mondays just a bit more tolerable.

I am also appreciative of the sanity checks that my “running” club GLH<sup>3</sup> has given me and the support of a number of its members. I’m glad that I’ve left an impact on the club, and hope the friends I’ve coerced (HPP, SBH, UO, SSL, and others yet to be named) enjoy it in my absence. Meeting BS and FR in my first months here was comforting. The Fourth of July shindigs at CBS’s are memorable, and he has also been particularly supportive and entertaining. Without \*HP, it would have been difficult to find the excitement of running, to do something crazy like tackling a marathon, or to rediscover the joy of bicycling (including all those wonderful DALMAC experiences). The physical activity that kept me sane through the years must also give credit to the Tuesday morning basketball gang, even though

I rarely wanted to stir that early in the morning.

My curiosity and thirst for knowledge is clearly accredited to my upbringing. I remember many of my early learning experiences being attributed to interactions with my siblings and parents. I am glad that their intellectual pursuits continue and especially thank the encouragement they have given me throughout the years.

Of course, the National Science Foundation is highly important for the funding of the research; may their budget ever grow. I also should acknowledge Oak Ridge Associated Universities for giving me the most memorable experience of my time at Michigan State by giving me an opportunity to be a participant in the Lindau meeting of Nobel Laureates. I will remember that trip and the people I met there for years to come.

# TABLE OF CONTENTS

<b>List of Tables</b> . . . . .	vii
<b>List of Figures</b> . . . . .	viii
<b>1 Introduction</b> . . . . .	<b>1</b>
1.1 The nucleus . . . . .	1
1.2 Nuclear structure and shell model . . . . .	4
1.3 Shell model near the “Island of Inversion” . . . . .	8
1.4 Nucleon knockout reactions . . . . .	10
<b>2 Methods</b> . . . . .	<b>15</b>
2.1 Overview . . . . .	15
2.2 Isotope production . . . . .	16
2.2.1 Ion source . . . . .	16
2.2.2 Coupled Cyclotron Facility . . . . .	17
2.2.3 A1900 . . . . .	17
2.3 Particle detection . . . . .	18
2.3.1 The S800 focal plane detectors . . . . .	20
2.3.2 Inverse mapping . . . . .	22
2.4 Gamma-ray detection . . . . .	23
2.4.1 Gamma-ray angular correlations . . . . .	25
2.4.2 Gamma ray linear polarization . . . . .	26
2.4.3 Segmented Germanium Array . . . . .	30
2.4.4 Relativistic kinematics . . . . .	31
2.4.5 Velocity determination . . . . .	32
<b>3 Offline Detector Characterization</b> . . . . .	<b>34</b>
3.1 Energy calibration . . . . .	34
3.2 Efficiency calibration . . . . .	37
3.3 Polarization sensitivity determination . . . . .	39
3.3.1 Detector setup . . . . .	40
3.3.2 Gamma-ray angular distribution . . . . .	42
3.3.3 Scattering asymmetry normalization . . . . .	45
3.3.4 Sensitivity determination . . . . .	45
3.3.5 Figure-of-merit discussion . . . . .	48
<b>4 Proton knockout studies</b> . . . . .	<b>51</b>
4.1 Electronics trigger . . . . .	52
4.2 $^{31}\text{Mg}$ . . . . .	53



4.2.1	Beam characteristics and particle ID . . . . .	53
4.2.2	Level scheme . . . . .	56
4.2.3	Inclusive and partial cross sections . . . . .	61
4.2.4	Momentum distribution of residues . . . . .	66
4.2.5	Angular distribution of gamma rays . . . . .	67
4.2.6	Linear polarization of gamma rays . . . . .	70
4.2.7	Spin and parity assignments . . . . .	71
4.3	<sup>33</sup> Mg . . . . .	74
4.3.1	Beam characteristics and particle ID . . . . .	74
4.3.2	Level scheme . . . . .	75
4.3.3	Inclusive and partial cross sections . . . . .	80
4.3.4	Momentum distribution of residues . . . . .	83
4.3.5	Angular distribution of gamma rays . . . . .	84
4.3.6	Linear polarization of gamma rays . . . . .	86
4.3.7	Spin and parity assignments . . . . .	87
<b>5</b>	<b>Commentary . . . . .</b>	<b>90</b>
5.1	<sup>31</sup> Mg . . . . .	90
5.1.1	Calculation of momentum distribution . . . . .	90
5.1.2	Structure of observed excited states . . . . .	91
5.1.3	Spin alignment calculation and angular distribution . . . . .	94
5.2	<sup>33</sup> Mg . . . . .	95
5.2.1	Calculation of the momentum distribution . . . . .	95
5.2.2	Structure of populated states . . . . .	96
<b>6</b>	<b>Outlook . . . . .</b>	<b>102</b>
6.1	Signal decomposition and gamma-ray tracking . . . . .	103
6.2	SeGA digital electronics . . . . .	106
6.3	GRETINA impact . . . . .	112
<b>7</b>	<b>Conclusions . . . . .</b>	<b>116</b>
<b>A</b>	<b>Gamma-ray angular distribution . . . . .</b>	<b>118</b>
<b>B</b>	<b>Relativistic Kinematics . . . . .</b>	<b>125</b>
B.1	Lifetime . . . . .	126
B.2	Angle . . . . .	126
B.3	Energy . . . . .	127
B.4	Polarization . . . . .	127
	<b>Bibliography . . . . .</b>	<b>130</b>

## LIST OF TABLES

3.1	Comparison of SeGA to other detector arrays for polarization measurements. . . . .	49
4.1	Secondary beam characteristics. . . . .	52
4.2	Gamma-ray transition properties in $^{31}\text{Mg}$ . . . . .	57
4.3	$^{31}\text{Mg}$ states with direct feeding from the proton knockout from $^{32}\text{Al}$ . . . . .	65
4.4	Gamma-ray transition properties in $^{33}\text{Mg}$ . . . . .	76
4.5	$^{33}\text{Mg}$ states with direct feeding from the proton knockout from $^{34}\text{Al}$ . . . . .	82
6.1	Relevant quantities for angular distribution measurements for GRETA angles assuming $\beta = 0.4$ . . . . .	113
A.1	Maximum alignment coefficients for different types of alignment. . . . .	120

## LIST OF FIGURES

1.1	Chart of nuclides . . . . .	3
1.2	Single-particle energies in spherical shell model . . . . .	6
1.3	Evolution of the <i>sd-pf</i> shell gap . . . . .	9
1.4	Cartoon of a knockout reaction. . . . .	11
2.1	Schematic of the S800 spectrograph. . . . .	19
2.2	S800 Focal plane coordinate definition . . . . .	23
2.3	Polarization digram . . . . .	28
2.4	Depiction of the segmentation of a SeGA detector. . . . .	31
3.1	<sup>226</sup> Ra energy spectrum for calibration . . . . .	35
3.2	Efficiency of SeGA . . . . .	38
3.3	<sup>249</sup> Cf decay scheme . . . . .	40
3.4	$\alpha$ - $\gamma$ coincidence setup . . . . .	41
3.5	<sup>245</sup> Cm gamma ray energy spectrum following the $\alpha$ decay of <sup>249</sup> Cf . . . . .	43
3.6	$a_2$ coefficient fit for $\alpha$ - $\gamma$ coincidences . . . . .	44
3.7	Scattering relative to reaction plane for a SeGA detector . . . . .	46
3.8	Geometric Compton scattering asymmetry for unpolarized gamma rays . . . . .	47
3.9	Normalized Compton scattering asymmetry for polarized gamma rays . . . . .	48

4.1	Identification of incoming $^{32}\text{Al}$ particles . . . . .	54
4.2	Identification of outgoing residues from incoming $^{32}\text{Al}$ beam . . . . .	55
4.3	$^{31}\text{Mg}$ gamma-ray spectrum . . . . .	56
4.4	Gamma-ray spectrum of $\gamma$ - $\gamma$ coincidences in $^{31}\text{Mg}$ . . . . .	58
4.5	$^{31}\text{Mg}$ level scheme . . . . .	60
4.6	Observed doublets in $^{31}\text{Mg}$ . . . . .	61
4.7	Acceptance cut for $^{31}\text{Mg}$ isotopes . . . . .	63
4.8	Run-by-run inclusive cross section for $^{31}\text{Mg}$ . . . . .	64
4.9	Longitudinal momentum distribution of $^{31}\text{Mg}$ . . . . .	66
4.10	Angular distribution effects of decays from 221 keV state in $^{31}\text{Mg}$ . . . . .	67
4.11	Automatic fitting of gamma-ray peaks in $^{31}\text{Mg}$ . . . . .	69
4.12	Momentum-gated angular distribution of 623 keV gamma rays in $^{31}\text{Mg}$ . . . . .	70
4.13	Compton scattering asymmetry of gamma rays in $^{31}\text{Mg}$ . . . . .	72
4.14	$a_2$ - $P$ diagram for gamma-ray decays in $^{31}\text{Mg}$ . . . . .	73
4.15	Identification of incoming $^{34}\text{Al}$ isotopes . . . . .	75
4.16	Identification of residues resulting from fragmentation of $^{34}\text{Al}$ beam . . . . .	76
4.17	Gamma-ray spectrum for $^{33}\text{Mg}$ . . . . .	77
4.18	Gamma-ray spectrum for $\gamma$ - $\gamma$ coincidences in $^{33}\text{Mg}$ . . . . .	79
4.19	$^{33}\text{Mg}$ level scheme . . . . .	80
4.20	Acceptance cut for $^{33}\text{Mg}$ isotopes . . . . .	81
4.21	Run-by-run inclusive cross section for $^{33}\text{Mg}$ . . . . .	82
4.22	Longitudinal momentum distribution for $^{33}\text{Mg}$ residues . . . . .	83

4.23	Momentum-gated angular distribution for $^{33}\text{Mg}$ gamma rays . . . . .	84
4.24	Compton scattering asymmetry of gamma rays in $^{33}\text{Mg}$ . . . . .	86
4.25	$a_2$ - $P$ diagram for decays in $^{33}\text{Mg}$ . . . . .	88
5.1	Effect of quadrupole mixing on the angular distribution coefficient . .	93
5.2	Convolution of theoretical momentum distribution and experimental effects . . . . .	96
5.3	Nilsson diagram used for $^{31,33}\text{Mg}$ . . . . .	100
6.1	Induced signals recorded by digital data acquisition system . . . . .	104
6.2	HPGe drift velocities . . . . .	105
6.3	Timing characteristics for different channels of DDAS . . . . .	108
6.4	Energy-time matrix recorded by DDAS . . . . .	109
6.5	Segmentation of SeGA based on the drifting of electron holes to segment electrodes . . . . .	110
6.6	Grid points for waveform sampling . . . . .	111
6.7	Angular distribution sensitivity . . . . .	114
A.1	Angular distribution coefficients and linear polarization values for selected transitions . . . . .	122
A.2	Angular distribution coefficients and linear polarization values for different prolate alignments . . . . .	123

# Chapter 1

## Introduction

### 1.1 The nucleus

One of the aims of science is to understand the composition of matter which makes up our planet, solar system, and universe. With increasing knowledge, mankind has broken matter into its smaller building blocks. Molecules are composed of atoms, and at the heart of every atom lies the nucleus. The properties of the nucleus are determined by its constituent parts which consist of chargeless neutrons and positively charged protons. These constituents are collectively known as nucleons. A nucleus is a quantum many-body system with a given number  $Z$  of protons and  $N$  of neutrons which characterize it as a particular isotope. A specific nucleus is often referenced by  ${}^A_Z\text{X}_N$  where  $A$  is the total number of nucleons and  $X$  is the chemical symbol.

The properties of nuclei are of fundamental interest to understand the underlying forces which are responsible for binding the nucleons together. Nuclei are small dense objects with sizes on the length scale of femtometers ( $10^{-15}$  meters) and masses of approximately  $A \text{ GeV}/c^2$ . Each isotope has a binding energy  $B(N, Z)$  as a result of the forces interacting within the nucleus. In a simple model, these macroscopic properties can be calculated considering the nucleus as a liquid drop [1] including

volume and surface effects. Coulomb repulsion and strong pairing of the nucleons also must be treated to reproduce the observations. The strong pairing of nucleons in time-reversed orbits leads to an enhanced binding of isotopes with an even number of neutrons or protons.

The forces in the nucleus conspire to bind certain nuclei more than others. The nucleus could be more bound if a neutron changed to a proton or vice versa. This process is governed by  $\beta$ -decay and causes some nuclei along a line with the same  $A$  to be stable. Other isobars having the same  $A$  decay towards this valley of stability by sequential  $\beta$  decays. For a given element, only a small number of nuclides are stable while a greater number are unstable. This is shown in the chart of the nuclides (Fig. 1.1) which displays all the isotopes with different neutron and proton numbers. Heavier isotopes can also be unbound through other processes. These include  $\alpha$ -decay where a doubly-charged  ${}^4\text{He}$  tunnels through the nuclear potential and escapes the nucleus as well as fission where the nucleus separates into two or more pieces. For nuclei with extreme proton-to-neutron ratios relative to the valley of the stability, individual nucleons can be unbound and emitted by the nucleus. The proton (or neutron) dripline is where it is no longer possible to add an additional bound proton (or neutron), and the nucleus will decay by particle emission. In part, this can be characterized by the difference of binding energies for neighboring isotopes. These are called the proton separation energies ( $S_p = B(N, Z) - B(N, Z - 1)$ ) and neutron separation energies ( $S_n = B(N, Z) - B(N - 1, Z)$ ). However, the rate of charged particle decay can also be hindered by the probability of tunneling through the Coulomb barrier causing these to be particle-stable and proceed to the valley of stability through beta decay.

Beyond a naïve macroscopic model, microscopic effects must be accounted for which impact the structure of the observed nuclei. The nucleus is a strongly interacting system where several forces of the Standard Model converge. Theoretical models

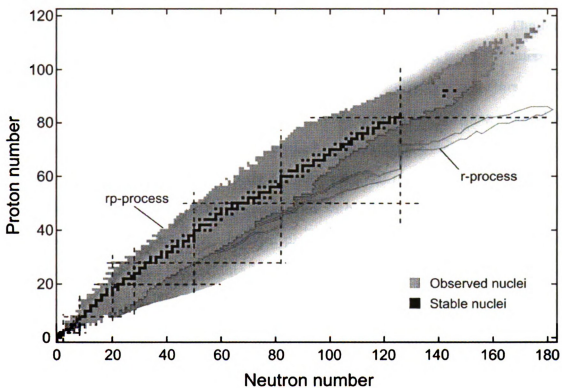


Figure 1.1: Chart of the nuclides with proton number  $Z$  on the ordinate and neutron number  $N$  on the abscissa. Stable isotopes are shown in black while unstable nuclei are shown in grey. Many of these unstable nuclei have been observed (light gray), but a large number of these nuclei are outside the current reach of experimental facilities with the predicted boundaries illustrated in dark gray. Magic numbers with increased binding energy are shown as dashed lines. Several astrophysical processes are also shown which involve nuclei far from the line of stability.



must treat the strong, weak, and electromagnetic interactions to describe the properties of nuclei. Since the strong force acts non-perturbatively, the exact mathematical form of the nucleon-nucleon interaction cannot be calculated explicitly. Instead, the form is determined in the context of several different approaches either theoretical or phenomenological [1]. Different approaches come to comparable results which agree well with nucleon-nucleon scattering data across a wide range of energies. The nucleon potential must be strong and short-ranged on the range of a few  $10^{-15}$  meters. It must also have a repulsive core at small distances. Two important factors which add much to the richness of nuclear structure are the presence of a strong spin-orbit interaction as well as a tensor interaction which allows mixing between states of different orbital angular momenta. Early phenomenological models fit the interaction strength to scattering data with four parameters with quite a bit of success as in the Hamada-Johnston potential [2]. Modern phenomenology has fine tuned to the potential to accommodate further data by adding some further parameters such as the Argonne  $v_{18}$  potential [3]. *Ab initio* approaches attempt to derive properties of nuclei by folding the nucleon-nucleon interaction over all the constituents of the nucleus. However, this becomes computationally intractable for nuclei with masses  $A \gtrsim 10$ . For heavier nuclei, a shell model is often employed which approximates the nucleon-nucleon interactions with a spherical potential well which is phenomenologically fit to reproduce key nuclear properties. Residual interactions are then considered between a selected subset of the nucleons.

## 1.2 Nuclear structure and shell model

Nucleons have an intrinsic angular momentum,  $s = 1/2\hbar$ , known as spin. Inside the nucleus, this spin couples to the orbital angular momentum,  $\ell$ , of the nucleon to form the total angular momentum  $j$ . In the nuclear shell model, these nucleons fill

orbitals denoted by  $\tau n\ell_j$  where  $\tau$  describes the type of nucleon ( $\nu$  for neutrons and  $\pi$  for protons). These single-particle states are bunched in groups according to their principal quantum number  $n$  in a harmonic oscillator potential.

All the nucleon single-particle states for a given nucleus are coupled to a final total angular momentum of  $J$  (colloquially referred to as spin). Due to the strong pairing in nuclei, nuclei with an even number of protons and neutrons always have a ground state spin of  $0^+$ . For odd- $A$  nuclei, the nuclear spin is dominated by the effects of the unpaired nucleon. Furthermore, the single-particle orbitals have a definite parity  $\pi = (-1)^\ell$  which describes the properties of the wavefunction under spatial inversion. The parity of the nucleus is the simple product of all the individual nucleon parities. Measurement of the parity gives access to determining the nature of the orbital angular momentum of the nucleon.

Each of these orbitals also has a corresponding single-particle energy within the mean field of the nucleus. Similar to electron orbitals in the noble gases, certain “magic” numbers of nucleons are considerably more stable [1]. This arises from a gap in the single-particle energies at the top of the Fermi surface. Isotopes which have a magic number of both neutrons and protons are called doubly-magic, while those that have a magic number of one or the other are known as semi-magic. Magic nuclei tend to be more spherical, and for even-even nuclei possess a higher excitation of the first excited state ( $E(2_1^+)$ ) and a smaller reduced transition probability ( $B(E2; 2_1^+ \rightarrow 0_1^+)$ ). These magic numbers (canonically 2, 8, 20, 28, 50, 82, and 126) create a clear division of the single-particle orbitals into different shells as shown in Fig. 1.2. With these magic numbers, there exists a handful of particle-bound doubly-magic nuclei ( $^4\text{He}$ ,  $^{16}\text{O}$ ,  $^{40}\text{Ca}$ ,  $^{48}\text{Ca}$ ,  $^{56}\text{Ni}$ ,  $^{78}\text{Ni}$ ,  $^{100}\text{Sn}$ ,  $^{132}\text{Sn}$ , and  $^{208}\text{Pb}$ ). These shells are referred to by the single-particle orbital angular momentum values included above the previous closed shell; i.e.  $s$ -shell,  $p$ -shell, and  $sd$ -shell for the shells up to 2, 8, and 20 single-particle orbitals, where  $s, p, d, f, g, \dots$  correspond to  $\ell = 0, 1, 2, 3, 4, \dots$

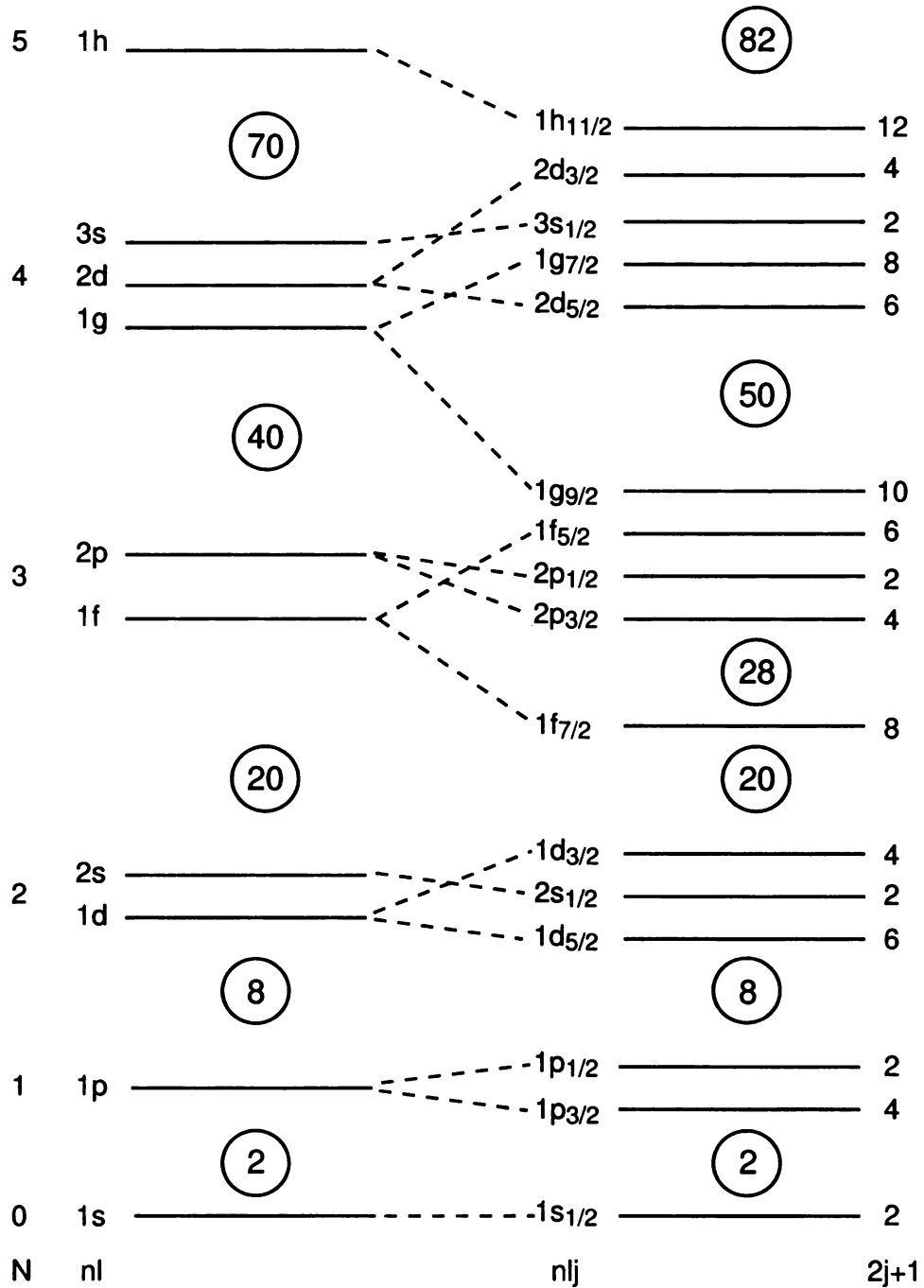


Figure 1.2: Shell model denoting single-particle energies up to the  $h_{11/2}$  orbital before (left) and after (right) including spin-orbit effects [4]. Circled magic numbers correspond to the gaps in the single-particle energies.

respectively. Each orbital has  $2j + 1$  magnetic substates after which the orbital is filled. When all the orbitals in a shell are filled, that shell is closed, and the addition of a further nucleon requires significantly more energy due to the gap in the single-particle energies.

Recent experiments with rare isotope beams have shown that the magic numbers which apply near stability can evolve as one proceeds towards more exotic isotopes [5]. These experiments indicate the weakening of the existing shell closures and the appearance of new magic numbers [6, 7]. Furthermore, the structure of the nuclei near the dripline can exhibit curious effects such as proton/neutron skins or halo states such as in  ${}^{11}\text{Li}$  [8]. Since the nuclear potential is connected to the spatial distribution of the nucleons, these exotic structures cause a modification in the mean field in the nuclear medium.

Due to the short range nature of the strong force, the mean nuclear potential can be approximated by a Woods-Saxon function:

$$f_{\text{WS}}(r) = V_0 / (1 + \exp(\frac{r - r_0}{a})) \quad (1.1)$$

with a depth  $V_0$ , radius  $r_0$  and diffuseness  $a$ . A large spin-orbit term must be included as well in order to reproduce the observed shell gaps shown in Fig. 1.2. The Woods-Saxon potential, particularly the depth, is adjusted to reproduce the observed single-particle energies [5, 9]. Where single-particle energies are not available, they can be extracted in a Hartree-Fock calculation with a self-consistent interaction based on effective energy-density functionals such as the Skyrme SkX interaction [10].

Once the properties of the single-particle orbits are derived, a residual two-body interaction remains in the Hamiltonian which is adjusted to reproduce other experimental observables. The nuclear wavefunctions are determined by diagonalization of this Hamiltonian. The residual two-body off-diagonal matrix elements between

single-particle orbitals result in an additional correlation energy for a given eigenstate. To allow calculations to be computationally feasible, approximations about the single-particle states must be made. Generally, the nucleus is considered to have an inert core where the orbitals are fully occupied and interactions are minimal such as in a nearby doubly-magic nucleus. The additional neutron and proton particles or holes are then built onto this inert core. Furthermore, the number of single-particle states must be truncated to a certain valence space. The two-body matrix elements are then calculated phenomenologically within the model space outside the inert core. However, the assumptions about the core and valence space depend on the nucleus of interest, so the derived effective interaction is only applicable to a certain region of the nuclear landscape [5]. In the present work, the region of interest is centered around  $Z = 12$  and  $N = 20$ . To describe states with normal single-particle ordering (as in Fig. 1.2), the Universal SD (USD) interaction [11] is used which assumes an inert core of  $^{16}\text{O}$  or  $^{40}\text{Ca}$  and includes the  $1d_{5/2}$ ,  $2s_{1/2}$  and  $1d_{3/2}$  orbitals in its model space.

### 1.3 Shell model near the “Island of Inversion”

For the isotopes with  $Z \approx 8$  to  $Z \approx 13$ , the shell structure evolves considerably for neutron-rich nuclei. Here, the  $N = 20$  shell closure is considerably weakening, while experiments show a pronounced  $N = 16$  subshell closure [7] (see Fig. 1.3). With the weakening of the  $N = 20$  shell gap, neutron excitations across the gap appear at relatively low excitation energies. The states built on these neutron excitations are called intruder states, and are referred to as  $npmh$  states by the number of neutrons  $n$  excited into the  $fp$ -shell and remaining  $m$  holes in the  $sd$ -shell. To treat these states properly, the  $1f_{7/2}$  and  $2p_{3/2}$  orbitals must be included in calculations greatly increasing the model space.

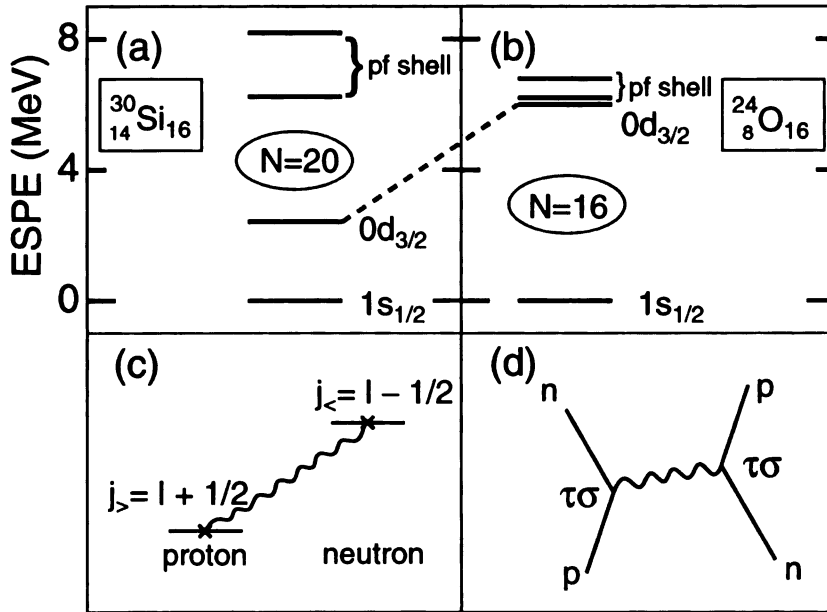


Figure 1.3: Effective single-particle energies for  $N = 16$  isotones for silicon (a) and oxygen (b). Note the shift in the  $0d_{3/2}$  orbital which is driven by the interaction shown in (c) between protons and neutrons with the same orbital angular momentum but opposite spins. This proceeds through the  $\sigma\tau$  operator (d) (adapted from Otsuka et al. [12])

For the nuclei with  $Z \approx 11$  and  $N \approx 20$ , the correlation energy from the residual two-body interactions makes these intruder states the energetically preferred configurations. This region is known as the “island of inversion” [13] where the ground-state wavefunction is dominated by particle-hole excitations across the  $N = 20$  shell gap. Experimental evidence of the breakdown of the  $N = 20$  shell closure is given by a small  $2_1^+$  energy in  $^{32}\text{Mg}$  [14] and an increase in collectivity [15,16]. Furthermore, excitation across the  $N = 20$  shell gap are necessary to appropriately describe the mass systematics in the region [17]. To describe these cross-shell excitations, the  $T = 0$  proton-neutron interaction is a major factor especially between the  $d_{5/2}$  protons and  $d_{3/2}, f_{7/2}$  neutrons [13]. The mechanisms that influence this region are also believed to be important in other regions of the nuclear landscape where inversion has been

observed, such as in  $^{12}\text{Be}$  [18, 19], or is theoretically predicted to occur [13].

The boundaries of the island of inversion have been proposed by including the entire  $fp$ -shell into the model space [13] and deducing that increased pairing and proton-neutron interactions play a significant role in the region. Theoretically, the extent was originally suggested to lie between  $10 \leq Z \leq 12$  and  $20 \leq N \leq 22$ . However, recent measurements of the ground state spins of magnesium isotopes ( $Z = 12$ ) have contributed information about the energetically favored configurations in this region [20–22]. With the additional information provided by data from neutron knockout [23] and Coulomb excitation [15, 16], the isotones with  $N = 19$  are also included in the island of inversion. Furthermore, recent results indicate intruder configurations in more neutron-rich  $^{36}\text{Mg}$  [24] and less neutron-rich  $^{28}\text{Ne}$  [16, 25] extending the reach of the island further than originally anticipated [13]. Determining the boundaries and mechanisms in the island of inversion is an important test of theoretical models which predict properties far from stability.

## 1.4 Nucleon knockout reactions

Nucleon knockout reactions are a powerful spectroscopic tool at intermediate energies to study nuclei. After the removal of a nucleon from an incoming projectile, the longitudinal momentum distribution of the residue is sensitive to the orbital angular momentum of the removed nucleon [26] as well as the distribution of magnetic substates in the residue. The partial cross sections to states populated in the residue also contain information about the wavefunction overlap between the neighboring nuclei. In the transitional region near the island of inversion, this can selectively probe states with intruder-like or normal configurations.

In a typical neutron-knockout reaction (Fig. 1.4), a nucleus of mass  $A$  impinges on a light nuclear target (such as  $^9\text{Be}$  or  $^{12}\text{C}$ ) and the reaction residue of mass  $A - 1$

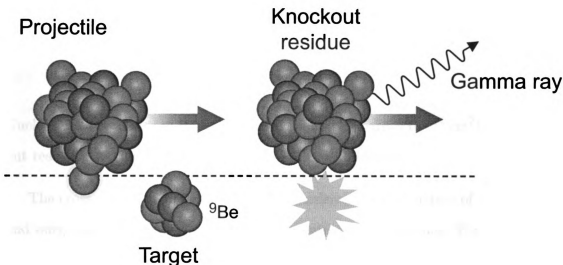


Figure 1.4: Cartoon of a knockout reaction.

exit moving at nearly the same velocity of the original projectile. The change in velocity is related to the momentum of the removed nucleon. The residue frequently leaves in an excited state which decays by gamma-ray emission. For energies above 50 MeV/nucleon, the reaction mechanism is simplified and can be considered to proceed in a single step. If the removed nucleon is not observed, the reaction encompasses a number of breakup channels. The dominant processes are diffractive breakup and stripping. For the stripping reaction, the nucleon is absorbed by the target as opposed to diffractive breakup where the nucleon and core interact elastically in the nuclear mean field of the target. Knockout is predominately a peripheral processes which probes the nuclear surface removing the most weakly-bound valence nucleons.

For a given reaction on a single scattering center, the cross section relates the rate of outgoing flux per unit surface area relative to the incoming flux of particles. Given a target of thickness  $T$  and density  $\rho$  with molar mass  $m \approx A \cdot 10^3$  mg, the number of scattering centers per unit area is  $\rho T N_0 / m$  where  $N_0$  is Avogadro's number. The nominal thickness  $t$  is often quoted in units of  $\text{mg}/\text{cm}^2$  or  $t = \rho T$ . If there are  $N_i$



incoming particles and  $N_f$  outgoing residues, the total cross section is then

$$\sigma = \frac{N_f}{N_i} \frac{m}{N_0 t}. \quad (1.2)$$

Nuclear cross sections are typically quoted in units of barns ( $10^{-24} \text{ cm}^2$ ) with knock-out reactions having cross sections around several millibarn.

The cross section to individual states is sensitive to the structure of the incoming and outgoing nuclei, including angular momentum selection rules. For the removal of a nucleon with total angular momentum  $j$ , the final states in the nucleus,  $(J^\pi)_f$  must follow the selection rules:

$$\begin{aligned} |J_i - j| < J_f < |J_i + j| \\ \pi_f &= \pi_i (-1)^\ell \end{aligned} \quad (1.3)$$

For the population of different final states, the reaction can proceed by the removal of different valence nucleons with quantum numbers  $\kappa = (n\ell_j)$ . For an initial spin of  $0^+$  and final spin of  $J^\pi$ , one only consider contributions from single-particle states which can couple to a total spin of  $J^\pi$ . This allows for the deduction of spectroscopic factors,  $C^2 S_i(\kappa)$ , for the  $i$ th excited state of the core. The total cross section,  $\sigma_i$ , can then be determined by summing the contributions from different valence nucleons given single-particle cross sections,  $\sigma_{\text{sp}}$ , calculated by a reaction theory.

$$\sigma_i = \sum_{\kappa} C^2 S_i(\kappa) \sigma_{\text{sp}}(S_n, \kappa) \quad (1.4)$$

The cross sections to individual magnetic substates,  $\sigma_m$ , for a given  $J^\pi$  are of particular interest in the current work. The distribution of magnetic substates is used to calculate the alignment parameters for  $\gamma$ -ray angular distribution and linear polarization discussed in Sec. 2.4. Here the coupling of the core spin to the valence

nucleon becomes important. Consider the core spin  $(c, \gamma)$  where  $\gamma = c_z$  coupled to the valence nucleon  $(j, m)$  resulting in a total spin of  $(J, M)$ . For a core with  $(c, \gamma) = (0, 0)$ , the cross section for the removal of a valence nucleon with a particular substate can be written

$$\sigma_m(j) = \sum_{\lambda, \sigma} \frac{2\ell + 1}{2j + 1} (\ell \lambda s \sigma | j m)^2 \sigma_\lambda(\ell) \quad (1.5)$$

with the sum taken over the projections of the angular momentum,  $\lambda = \ell_z$ , and spin,  $\sigma = s_z$ , of the valence nucleon onto the quantization axis which is taken as the velocity of the outgoing residue. The cross sections with respect to the substates of  $\ell$ ,  $\sigma_\lambda(\ell)$ , are extracted from the reaction theory assuming an interaction of the valence nucleon with the target nucleus which is independent of spin coupling and angular momentum coupling. Then given a core with  $(c, \gamma) \neq (0, 0)$ , the cross section to the core magnetic substates is

$$\sigma_\gamma(c) = \sum_{m, M} \frac{2j + 1}{2J + 1} (j m c \gamma | J M)^2 \sigma_m(j). \quad (1.6)$$

Evoking (Eq. 1.5) this is expressed as:

$$\sigma_\gamma(c) = \sum_{m, M, \lambda, \sigma} \frac{2\ell + 1}{2J + 1} (j m c \gamma | J M)^2 (\ell \lambda s \sigma | j m)^2 \sigma_\lambda(\ell). \quad (1.7)$$

Here the single-particle cross section,  $\sigma_{\text{sp}}$ , can be related to the substate cross sections through

$$\sigma_{\text{sp}} = \sum_{\lambda} \sigma_\lambda(\ell) = \sum_{\gamma} \sigma_\gamma(c) = \sum_m \sigma_m(j) \quad (1.8)$$

and the total cross section determined using Eq. 1.4 by the spectroscopic factors of the individual valence nucleons in the incoming nucleus and single-particle cross sections derived from the reaction theory.

For knockout reactions with intermediate- to high- energy projectiles with velocity  $v$ , the single-particle cross sections are calculated assuming a process that is subject to the sudden and Eikonal approximations. The sudden approximation assumes that the interaction time in the target is short enough that multi-step processes, including excitation of the core or core-nucleon system, can be neglected. In the eikonal approximation, interactions with the target are assumed to not deflect the trajectory of the fast-moving incoming projectile. Following the interaction, the initial state is modified by the Eikonal phases of the core and the nucleon,  $S_c$  and  $S_\kappa$  respectively, determined as a function of impact parameter  $\vec{b}$  by the potential  $V$  for the nucleon-target and core-target systems by

$$S(\vec{b}) = \exp\left(\frac{-i}{\hbar v} \int_{-\infty}^{\infty} V(\vec{b}, z) dz\right). \quad (1.9)$$

The cross section is then determined using the methods described by Tostevin [27] including stripping and diffractive components. The interaction potential is determined by folding the nucleon-nucleon interaction over the densities of the core and the target. These densities are taken from Hartree-Fock calculations which reproduce a number of observables in the area. These knockout cross-section calculations have been instrumental in the interpretation of experiments with exotic nuclei [26,28] agreeing well with data provided by transfer reactions as well as high-energy knockout reactions such as  $(p, 2p)$  and  $(e, e'p)$ .

# Chapter 2

## Methods

### 2.1 Overview

A number of techniques must converge to successfully elucidate the structure of a particular nucleus  ${}^A_ZX$  with  $A$  total nucleons. First, one must produce the nucleus of interest. There are several methods capable of producing exotic nuclei. In the present work, a beam of stable nuclei is fragmented on a beryllium production target. Fragmentation of a stable beam at intermediate energies ( $\sim 100$  MeV/u) is well described by a statistical model [29] producing all lighter nuclei resulting from the stripping of nucleons from the projectile. Once a secondary beam of interest is produced, it impinges on a secondary target where a more direct reaction such as the removal of a single nucleon is analyzed. The nature of the reaction is important to obtain further structural information of both the incoming nucleus as well as the outgoing residue. Therefore, we must detect and identify both the incident and resultant particles. Furthermore, the reaction often leaves the residues in an excited state. The nucleus can then decay by  $\gamma$ -ray emission towards the ground state. The gamma rays emitted contain key information about the fundamental properties of the excited state and must be detected accordingly. Alternatively, the nucleus could decay by

particle emission if excited more than the particle separation energy or by  $\beta$  decay which proceeds slowly by the weak process. For the in-flight techniques discussed here, full relativistic inverse kinematics must be properly taken into account for the analysis as well.

## 2.2 Isotope production

The experiment was performed at the Coupled Cyclotron Facility (CCF) at National Superconducting Cyclotron Laboratory (NSCL). There are several important steps in the isotope production process. A high-quality primary stable beam must be first produced. Generally, a low-energy beam is extracted from an ion source. For heavy-ion beams, an electron cyclotron resonance (ECR) ion source is generally used such as ARTEMIS at NSCL. This beam of nuclei is then accelerated to relativistic speeds in the cyclotrons and finally fragmented on a target in order to produce the particular isotope. The reaction products must be filtered out to obtain a beam of acceptable purity for the experiment. Magnetic separation by the A1900 fragment separator provides the isotope filtering at NSCL.

### 2.2.1 Ion source

The  $^{48}\text{Ca}$  primary stable beam necessary for the experiment was extracted from a room temperature ion source, ARTEMIS [30]. The stable ions are baked off in an oven into a plasma of microwave-driven electrons. The electrons collide with the calcium and ionize them. A bias voltage of up to 30 kilovolts is applied to extract the ions. A single charge state is then selected and injected into the coupled cyclotrons.

### 2.2.2 Coupled Cyclotron Facility

The Coupled Cyclotron Facility [31] allowed for the acceleration of the stable ions. The CCF consists of two superconducting cyclotrons, the K500 and the K1200. The cyclotrons consist of strong magnetic fields such that the particles follow an isochronous path inside the cyclotron. An electric field is applied at a given radio frequency for the acceleration of the nuclei. The ions are extracted from each cyclotron when the magnetic field is no longer strong enough to constrain the particles. For protons, the extraction kinetic energy in MeV is equal to the “K” designation of the cyclotrons. For heavier ions, the limit is related to their charge-to-mass ratio ( $\propto (Q/A)^2$ ). Therefore, a high charge state is preferable, as opposed to the low charge states typically produced in ECR ion sources. To overcome this obstacle, the two cyclotrons are coupled to each other. After being accelerated to about 15% of the speed of light in the K500, the nuclei impinge on a thin carbon foil which strips away remaining electrons. The nuclei can then be accelerated to the highest capability by the second, more-powerful, K1200 cyclotron to a speed of approximately 50% of the speed of light.

### 2.2.3 A1900

After leaving the cyclotrons, the beam impinges on a thick beryllium fragmentation target where nucleons are removed from the nucleus. The smattering of isotopes must then be filtered using the A1900 projectile fragment separator [32] operating on the principle of magnetic separation. The A1900 is a series of four dipole magnets which bend the nuclei according to their magnetic rigidity  $B\rho$ . The magnets are tuned by adjusting the magnetic field such that the particles of interest bend the correct amount in each dipole. The magnetic rigidity is connected to the velocity and

charge-to-mass ratio of the particles.

$$B\rho = \frac{p}{Qe} = \frac{A\gamma\beta c u}{Q e}, \quad (2.1)$$

where  $u/e$  is the mass-to-charge ratio of a proton. However, this effectively transports all nuclei with a similar mass-to-charge ratio leading to contamination of the secondary beam. To ameliorate this situation, a wedge of aluminum is inserted between the second and third dipole magnets of the A1900 to slow down the fragments. At intermediate energies, the stopping power is mostly due to electronic stopping which is primarily sensitive to the charge of the incoming particles and target material properties ( $dE/dx \propto Z^2$ ) [33]. This allows for further separation of isotopes by choosing the proper magnetic rigidity for the dipoles upstream and downstream from the wedge. Slits are placed on the magnets' dispersive axis to select the isotopes of interest.

## 2.3 Particle detection

The particles incident on the secondary target must be identified, and the properties of the emerging residues must be measured in order to correlate emitted gamma rays with the proper reaction channel. The scattering of the residue also is related to the nature of the nuclear reaction as well as the internal structure of the nucleus. To analyze the residual nuclei, the S800 spectrograph was used [34]. The S800 is a large-acceptance, high-resolution magnetic spectrograph with an angular acceptance of 20 msr corresponding to roughly  $7^\circ$  in the dispersive plane and  $10^\circ$  in the non-dispersive plane. In focused mode, it also allows for a momentum acceptance of up to 6%. The secondary beryllium reaction foil was placed at the target position of the S800 (see Figure 2.1).

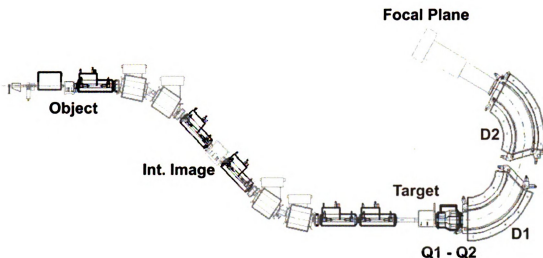


Figure 2.1: Schematic of the S800 spectrophotometer.

A thin plastic scintillator was placed in the object box of the S800 as well as at the end of the A1900 fragment separator. The time of flight between these two scintillators allows the identification of the incoming particles. The electronics for the measurement were triggered by the focal plane detectors of the S800 [35]. At the S800 focal plane, the residue is identified and its properties measured.

The S800 spectrophotometer has two standard operating modes: focused and dispersion-matched. In focused mode, the analysis line is achromatic causing the beam to be focused at the target and dispersed at the focal plane of the S800. This immediately limits the momentum resolution of the spectrophotometer to the incoming momentum width of the beam. The S800 could operate also with the dispersion matched causing the beam optics to be focused at the focal plane, leading to a better momentum resolution. However, in dispersion-matched mode, the beam is dispersed at the target reducing the momentum acceptance for the reaction channel of interest to 0.5% for a 5 cm reaction target since the beam is dispersed according to its incoming momentum at the target position. With this restraint, it was necessary for the current experiment



to run in focused mode.

### 2.3.1 The S800 focal plane detectors

The focal plane of S800 consists of several detectors necessary to measure the properties of the outgoing nuclei. Two position-sensitive cathode readout drift chambers (CRDCs) track each particle's trajectory through the focal plane. These CRDCs are followed by an ion chamber which measures the energy lost by the particle as it passes through a low pressure gas. At the end of the S800 spectrograph are several scintillators which provide a common timing signal to the acquisition electronics.

As the energy loss in the ion chamber depends on the charge of the nucleus, this allows for isotopic identification. The energy loss also depends on the velocity of the nucleus, but this difference in velocities of the transmitted isotopes is small making this dependence negligible compared to the difference in  $Z$ . The time of flight between the scintillator in the object box and the focal plane scintillators allows for a determination of the  $A/Q$  of the projectile residue, which combined with the ion chamber gives the exact particle identity. It is important to note that for the low  $Z$  projectiles at relatively high energies, contributions from different charge states can be neglected in the particle identification as calculated by the CHARGE program [36].

The efficiency of the particle identification must also be determined, taking into account the transmission in the analysis line and the spectrograph. Several normalization runs were performed throughout the experiment where a low-intensity unreacted primary beam was delivered to the focal plane of the S800 spectrograph. The intensity is purposely attenuated as the CRDCs are rate-limited to less than 5000 counts per second. During normal data runs, the high rate of the primary beam would overload the CRDCs, so a blocker is inserted to stop the primary beam from reaching the focal plane. The beam intensity at the target must then be determined by the intensity observed at the scintillators upstream of the target. The normalization runs give the

required relation between the scintillator intensities and the intensity at the reaction target which is necessary to extract the cross section. The number of particles incident on the target on a run-by-run basis is determined from the individual rates on the scintillators prior to the target folded with the analysis line transmission efficiency. Variations in the normalization across the span of the experiment contribute to systematic uncertainties and are discussed in further detail in Sec. 4 and the effects shown in Figs. 4.8 and 4.21.

Outside the identification of the particles, the kinematics of the residues at the target must be reconstructed. The two CRDCs at the focal plane do the lion's share of this task. The CRDCs are filled with a gas which is ionized as the high-energy particles pass through them. A high bias voltage causes the electrons to drift towards an anode wire. The position along the non-dispersive  $y$  axis is determined by measuring the drift time of the electrons to the anode wire. In the dispersive  $x$  direction, the position is determined by examining the charges produced on pads mounted along the anode wire. With these techniques, a 0.5 mm nominal resolution [35] can be achieved in both directions for beams at a low intensity. The two CRDCs are spaced approximately one meter apart which allows for the measurement of the angle of the particles at the focal plane.

The response of the CRDCs must be calibrated with particles with a well-known position in the focal plane. Several calibration runs were taken with a thick mask inserted in front of each CRDC. This collimated the beam to discrete points across the focal plane. The beam of particles was detuned and swept across the focal plane to ensure a comprehensive coverage of the focal plane. The known  $(x, y)$  locations of the holes in the mask were then fit linearly to the CRDC electronics readout to obtain the desired calibration. Over a week of running time, the calibration can drift slightly due to the changes in the operating environment. This motivated several CRDC calibration runs with the interim data calibrated by a linear interpolation of

the parameters determined by the relevant calibration runs which had a difference of about 10%. As the  $y$  position is determined by the drift time of the electrons, this measurement is slightly sensitive to the timing of the trigger which can vary dependent on the triggering conditions. Slightly different calibration parameters were extracted and used for the two sets of triggering conditions (see Sec. 4.1) on a run-by-run basis.

### 2.3.2 Inverse mapping

The position-sensitive CRDCs measure the locations and angles of the particles at the focal plane of the S800 on both the dispersive and non-dispersive axes. For this information to be useful, the tracks of the particles must be traced backward to the target. This is done by an inverse map which is calculated using COSY INFINITY [37] with the known magnetic rigidity of the spectrograph. This connects the four focal plane parameters determined at the CRDCs to the kinematics of the outgoing particle at the target. The map is calculated to the fifth order in the focal plane parameters: dispersive position ( $x_{fp}$ ), non-dispersive position ( $y_{fp}$ ), dispersive angle ( $a_{fp}$ ), and non-dispersive angle ( $b_{fp}$ ) which are shown in Fig. 2.2. Principally, the momentum vector of the particle leaving the target provides the most valuable information. The map therefore calculates the angle of propagation out of the target ( $a_{ta}, b_{ta}$ ) and the energy deviation from the central track in the spectrograph ( $d_{ta}$ ). The non-dispersive position at the target ( $y_{ta}$ ) is calculated as well. Since the track of the particles through the spectrograph depends on their particular  $A$  and  $Q$ , an inverse map was calculated for each reaction channel.

The inverse map only treats the kinematics of the particles exiting the target. To investigate the sensitivity to incoming beam parameters, GEANT4 [38] simulations were performed. Reasonable agreement with the data was reached for the unreacted aluminum isotopes with little change to the ideal incoming beam parameters. The  $b_{ta}$  resolution of the spectrograph in focused mode contributes significantly to the

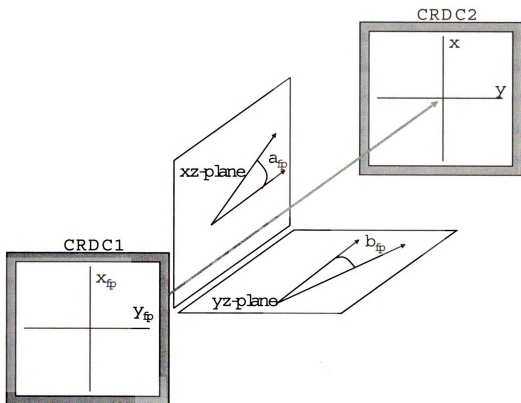


Figure 2.2: S800 Focal plane coordinate definition

observed experimental width. Since the system is azimuthally symmetric about the beam axis, a uniform distribution of the azimuthal angle  $\phi = \tan^{-1}(\frac{\sin b_{fp}}{\sin a_{fp}})$  is also expected and observed in the data.

## 2.4 Gamma-ray detection

The electromagnetic interaction is the best understood of all the fundamental forces. Nuclei excited to an energy below the particle separation threshold predominately decay by gamma-ray emission. These emitted gamma rays are sensitive probes to what is occurring within the nucleus. These nuclear transitions can also be calculated explicitly due to the precise understanding of the interaction allowing for rigorous tests of theory.

The detection of gamma rays in an experiment is a task which must balance the energy resolution of the detectors against the detection efficiency. This is directly related to the importance of detector angular granularity necessary to be able to correct for the Doppler shift for nuclei moving at relativistic speeds in the lab frame. Another factor which plays a large role in gamma-ray detection is the reduction of the signal-to-noise ratio as a significant background of gamma rays exists for in-beam studies. The background comes from several sources including bremsstrahlung of the ions as they traverse the target, naturally occurring radioactive sources, as well as photons which scatter out of the detector without depositing their full energy. Segmented germanium detectors, like those used in the present experiment, have an excellent energy resolution while also allowing for good angular resolution for precise Doppler correction.

In general, the gamma rays emitted in nuclear processes have energies in the range of about 100 keV to several MeV. Gamma rays with these energies interact with a detection material through three processes which deposit energy in the material: photoabsorption, Compton scattering, and pair production. Each of these interaction cross sections has a different energy dependence which divide the energy regime into three general regions. Particularly for interactions in germanium, photoabsorption is the primary process below 150 keV. At medium energies, the Compton scattering cross section increases above the photoabsorption cross section, being an order of magnitude higher around 350 keV. At the electron production threshold (1.022 MeV), pair production becomes possible, but remains a factor of 10 smaller than the Compton scattering cross section until 2.6 MeV [39]. For typical detectors and gamma-ray energies, the cross sections are such that a gamma-ray typically Compton scatters several times before a photoabsorption event.

Emission of the gamma rays from a nucleus depends on the electromagnetic transition matrix elements which are connected to the internal structure of the nucleus.

As these matrix elements are heavily energy dependent ( $\sim E^{2L+1}$ ), additional information can also be extracted based on the lifetimes of the involved excited states. The expected Weisskopf transition rates [40, 41] can provide estimates of the multiplicities of the transition. These estimates can then restrict the possible nuclear spins and parities of the initial  $J_i^\pi$  and final  $J_f^\pi$  states if one of the spins is previously known. This is governed by the selection rules for a gamma ray transition of multipolarity  $L$  and character  $\pi$ ,

$$|J_i - L| \leq J_f \leq J_i + L$$

$$\Delta\pi = \begin{cases} (-1)^L, & \pi \text{ electric} \\ (-1)^{L+1}, & \pi \text{ magnetic.} \end{cases} \quad (2.2)$$

### 2.4.1 Gamma-ray angular correlations

The correlation between the outgoing gamma rays and other observables provides clear information about the nuclear structure. Following a nuclear reaction, the nuclear spin can be aligned along an axis from the selective population of magnetic substates (see Sec. 1.4). This results in angular correlations for gamma rays emitted from an excited state. The angular distribution of a gamma ray transition provides information about the spins of the initial and final states. Furthermore, gamma rays can be emitted linearly polarized which is inherently connected with the difference of parities between the two states. In addition, these observables are related to parameters of the reaction that describe how the initial state is populated. Measuring gamma-ray angular distributions has been an important tool in nuclear structure studies at beam energies near the Coulomb barrier for a long time [42]. Recent investigation has begun to investigate the extension of this to radioactive beams with a velocity  $v \approx 0.4c$  [43]. The ability to measure angular distributions at these intermediate energies provides an opportunity for spin assignment in the most exotic

nuclei at the extremes of isospin. Details of the angular distribution formalism are discussed in App. A and more thoroughly in Refs. [42–44]. In general, the angular distribution of gamma rays,  $W(\theta)$ , can be expanded in terms of Legendre polynomials for a system with azimuthal symmetry. The form of the expansion depends on factors which quantify the amount of initial spin alignment in the system,  $B_\lambda$ , and a factor,  $A_\lambda$ , related to the properties of the particular  $\gamma$ -ray transition:

$$W(\theta) = \sum_{\lambda} A_{\lambda} B_{\lambda} P_{\lambda}(\cos \theta). \quad (2.3)$$

where the coefficient has been factored to separate the alignment which is dependent on the reaction and the transition properties which are related to the structure. Furthermore, higher orders of the angular distribution are often negligible which reduces the above expression to  $W(\theta) = 1 + A_2 B_2 P_2(\cos \theta)$ .

### 2.4.2 Gamma ray linear polarization

One key goal of this experiment was to determine if it was possible to detect the  $\gamma$ -ray linear polarization emitted from a source moving at a sizable fraction of the speed of light. To understand the results, one must have clear knowledge of the intrinsic response of the detector to linear polarized photons emitted from a source at rest.

For photons with energies in the experiment's range of interest, the most sensitive probe of the polarization is due to the asymmetry of the Compton scattering of the photon. The Klein-Nishina differential cross section [45, 46] for the Compton scattering of a photon with initial energy  $E_0$  and final energy  $E$  is:

$$\frac{d\sigma}{d\Omega} = \frac{r_e^2 E^2}{2 E_0^2} \left( \frac{E_0}{E} + \frac{E}{E_0} - 2 \sin^2 \theta \cos^2 \phi \right) \quad (2.4)$$

where  $r_e = e^2/m_e c^2$  is the classical Compton radius of the electron,  $\theta$  is the scattering

angle, and  $\phi$  is the angle of the incoming electric field vector of the incoming photon relative to the scattering plane. A detailed treatment and derivation of the cross section can be found in Heitler [47]. As the Compton scattering is a two-body process, the energy of the scattered photon is completely determined from the kinematics,

$$E = \frac{E_0}{1 + (E_0/m_e c^2)(1 - \cos \theta)}. \quad (2.5)$$

For a photon that interacts in the detector in two places depositing energies  $E_1$  and  $E_2$ , this allows some restriction of events which do not follow the proper kinematic relation based on  $E, E_0 = E_1 + E_2$ , and  $\theta$ . This could result from incomplete absorption of the incoming photon energy or false events caused by coincidence with naturally occurring background.

Polarimeters based on the sensitivity of Compton scattering to the polarization of the incoming photon have been built and used for fifty years [48]. The first and simplest setup consists of two  $\gamma$ -ray detectors where one functions as the scatterer, and a second serves as the analyzer. Since the cross section is most sensitive for scattering angles close to  $90^\circ$  for low-energy ( $< 1$  MeV) photons, an optimal setup consists of four analyzing crystals at an angle of  $90^\circ$  relative to a small scattering crystal [49]. However this results in a low photopeak efficiency which hampers measurements. Composite detectors such as the Clover [50] are natural Compton polarimeters using the scattering between neighboring crystals to determine the incoming polarization. However, the proximity of the analyzing region to the scattering point decreases the sensitivity of these detectors. This is offset, though, by the increased detection efficiency. The development of high-purity segmented germanium detectors has provided a new tool for polarization determination. Similar to composite detectors, segmented detectors successfully confront the difficulties of maintaining sufficient efficiency while the small volume of the segments allows a polarization sensitive detection of low-



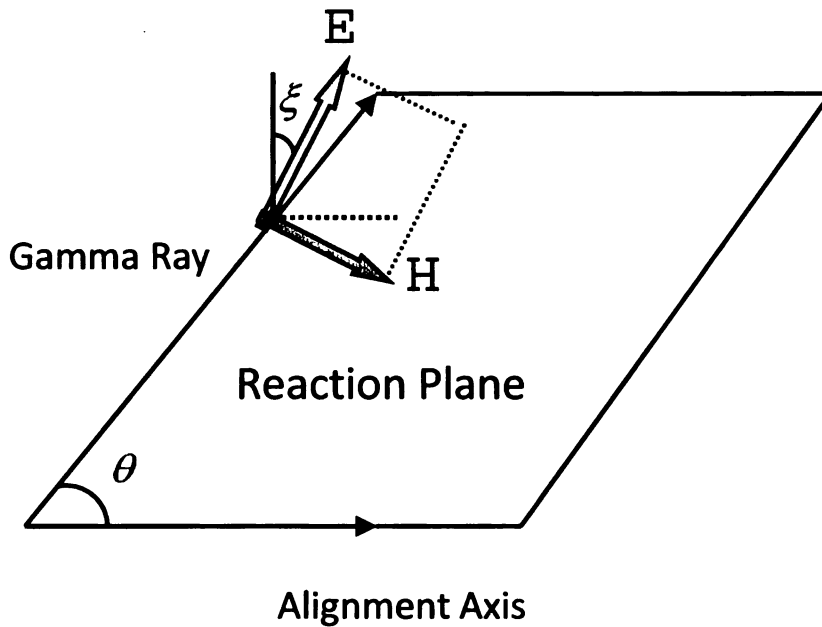


Figure 2.3: Polarization of a gamma ray characterized by the angle  $\xi$  of the electric field vector with respect to the normal of the reaction plane.

energy photons which Compton scatter. The capability of these segmented detectors to make sensitive linear polarization measurements has been demonstrated [49,51,52].

For an axially symmetric system, a spin-aligned nucleus emits gamma rays which are linearly polarized. The axial symmetry requires the necessary population of magnetic substates (i.e.  $w(m) = w(-m)$ ) to produce linear polarization. The polarization of the photon is relative to the reaction plane which is defined by the axis of the nuclear alignment and the photon's direction of propagation as shown in Fig. 2.3. The theoretical linear polarization distribution is defined as:

$$P(\theta) = \frac{W(\theta, \xi = 0^\circ) - W(\theta, \xi = 90^\circ)}{W(\theta, \xi = 0^\circ) + W(\theta, \xi = 90^\circ)} \quad (2.6)$$

where  $W(\theta, \xi)$  describes the likelihood of emitting a photon at an angle  $\theta$  to the axis of alignment and with an electric field vector at an angle of  $\xi$  to the reaction plane. However, the quantity observed in the experiment is the intensity of the energy

peaks of gamma rays which scatter an angle  $\phi$  relative to the reaction plane. The experimental asymmetry is defined as

$$A(\theta) = \frac{N(\theta, \phi = 90^\circ) - N(\theta, \phi = 0^\circ)}{N(\theta, \phi = 90^\circ) + N(\theta, \phi = 0^\circ)} \quad (2.7)$$

where  $N(\theta, \phi)$  is the number of counts in the photopeak. Since the scattering cross-section (Eq. 2.4) is maximized perpendicular to the direction of the electric field, the angles are related via  $\phi = 90 - \xi$ . As these quantities are related, the asymmetry and the polarization can be related for a polarimeter through its sensitivity,  $Q(E_\gamma)$ ,

$$A(\theta) = Q(E_\gamma)P(\theta). \quad (2.8)$$

The sensitivity depends on the incident energy and is limited by the difference in the scattering cross section. For a point-like polarimeter, the sensitivity  $Q_0$  calculated from the Klein-Nishina cross-section is:

$$Q_0(\alpha) = \frac{1 + \alpha}{1 + \alpha + \alpha^2} \quad (2.9)$$

where  $\alpha = \frac{E_\gamma}{m_e c^2}$ . For practical applications, the scattering asymmetry must address the geometric asymmetries of the detector. The asymmetries are compared to those observed from unpolarized gamma rays which are characterized by a parameter  $a$

$$a(E_\gamma) = \frac{N_{\text{unpolarized}}(\theta, \phi = 90^\circ)}{N_{\text{unpolarized}}(\theta, \phi = 0^\circ)} \quad (2.10)$$

$$A(\theta) = \frac{N(\theta, \phi = 90^\circ) - aN(\theta, \phi = 0^\circ)}{N(\theta, \phi = 90^\circ) + aN(\theta, \phi = 0^\circ)} \quad (2.11)$$

To determine the sensitivity of a detector, the analysis is done for gamma rays which have a well known polarization such as for pure dipole transitions which have an

angular distribution

$$W(\theta) = 1 + a_2 P_2(\cos \theta). \quad (2.12)$$

For pure dipole transitions, the polarization distribution reduces to the form [53]

$$P(\theta) = \pm \frac{3a_2 \sin^2 \theta}{2 + 2a_2 - 3a_2 \sin^2 \theta} \quad (2.13)$$

where  $a_2$  is determined from analyzing the angular distribution of gamma rays with a “+” sign for  $M1$  transitions and a “-” sign for  $E1$  transitions.

### 2.4.3 Segmented Germanium Array

The Segmented Germanium Array (SeGA) [54] serves as the workhorse for gamma ray spectroscopy at NSCL. It combines the superb energy resolution of germanium with a modest efficiency afforded by the array of detectors. In addition, angular resolution smaller than the detector size can be achieved using the internal electronic segmentation of the individual crystals. Eighteen detectors of n-type high-purity germanium (HPGe) comprise SeGA. Each is a cylindrical single crystal of germanium cooled by liquid nitrogen to 100 K. The crystal is 8 cm long with a 7 cm diameter. A central core electrode is inserted along the central axis of the crystal. The outside surface is electronically segmented into 32 segments with 4 azimuthal divisions and 8 longitudinal slices (see Figure 2.4). A bias voltage applied to each detector causes electrons liberated by an incoming gamma ray to drift to the center of the detector. The corresponding holes generated drift outward and are collected by electrodes placed on the outer surface for each segment.

The detectors are configurable into several standard arrays. For the present work, the “classic” SeGA configuration was used. This places the detectors in two rings surrounding the target position. Seven detectors are placed in the forward 37 degree ring,

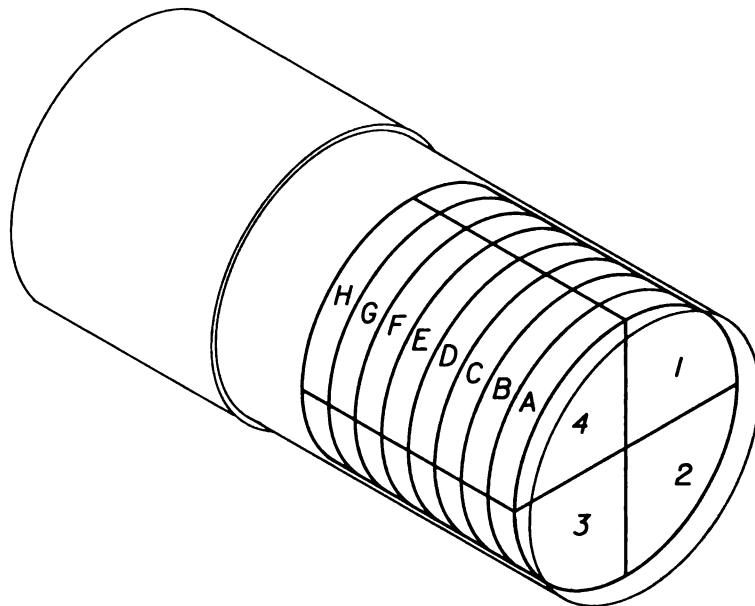


Figure 2.4: Depiction of the segmentation of a SeGA detector.

and ten are placed in the backward 90 degree ring. The crystals are positioned such that the transverse segmentation lies along the  $\theta$  direction defined by the coordinate system with  $z$  along the beam axis.

#### 2.4.4 Relativistic kinematics

Experiments at National Superconducting Cyclotron Laboratory are typically performed with velocities from 30%-50% the speed of light. At these velocities, relativistic effects become considerable and must be accounted for in the analysis. In particular, the velocity of the particle, the energy of emitted radiation, and the angle of the radiation with respect to the nucleus' velocity all become correlated as discussed in detail in Appendix B. Particle tracking in the S800 spectrograph supplies the necessary information about the magnitude and direction of the residual particle's velocity. To be able to precisely measure the gamma ray's energy, the angle of emis-

sion with respect to the beam axis must be known. This is where the segmentation of the detectors is critical, allowing the determination of the first interaction position within a detector based on the energy deposited in the individual segments. Generally, the location of the first interaction is taken as the midpoint of the segment where the most energy was deposited. This algorithm accurately identifies the segment with the first interaction point in most of the cases [55] especially when considering the possibility of having multiple interactions within a segment. However, the precision in the determination of the interaction point is limited by the size of the segment. Furthermore, the exact location where the nucleus was at the time of  $\gamma$ -ray emission is also unknown. Often this occurs within the target where the nucleus is actively slowing down leading to an additional effect related to the velocity uncertainty. These two effects are the major contributors to the limits of the energy resolution obtainable in an experiment with intermediate energy projectiles.

### 2.4.5 Velocity determination

SeGA was centered around the target position of the S800 to detect the gamma rays emitted following the secondary reaction. Gamma-ray spectra were Doppler corrected based on the energies of the fragments of interest at the middle of the target. The velocity of the fragments was determined in several ways which proved to be self-consistent. First, one can get the velocity based on the incoming particle energy and energy losses in the target from LISE++ [56] which uses a model based on the ATIMA 1.2 [57] characterization for heavy ion energy loss in matter. Alternatively, the velocity can be obtained on the downstream side of the target based on the deviation from the central momentum in the S800 spectrograph and back trace to the center of the target using the energy losses of LISE++. Energy losses based on GEANT4 also agree reasonably with those obtained with LISE++. Furthermore, one could estimate the velocity based on the uncorrected Doppler-shifted energy de-

posited in the  $90^\circ$  ring of SeGA which have their first interaction point within a different longitudinal segment and thus a different opening angle. This constrains the velocity if the  $\gamma$ -ray energy and positioning of the detector are well known (see Eq. B.8). Combining the systematic differences using these different methods, one obtains a reasonable estimate of the uncertainty in the velocity.

# Chapter 3

## Offline Detector Characterization

In preparation for the experiment with the beam, several source measurements were used to characterize the response of the detector. These were necessary to establish the calibration parameters for energy and efficiency. Furthermore, the detector's response to linear polarization also had to be investigated and its sensitivity quantified.

### 3.1 Energy calibration

To determine the energy of the gamma rays detected in SeGA, one must know how the detector and the Analog to Digital Converters (ADCs) respond to gamma rays of previously known energies. To accomplish this task, several standard radioactive calibration sources were used. This allows one to characterize the response of the detector across a wide range of energies. Furthermore, the central contact of the detector and the 32 segments have to be calibrated separately as they behave differently to the photon's energy deposit in the detector. For the central contact, the 13-bit channel output,  $x$ , from the ADC was assumed to be quadratically related to the energy of the incoming photon,  $E$ , i.e. for some calibration coefficients  $a_i$ ,

$$E = a_0 + a_1 x + a_2 x^2 \tag{3.1}$$

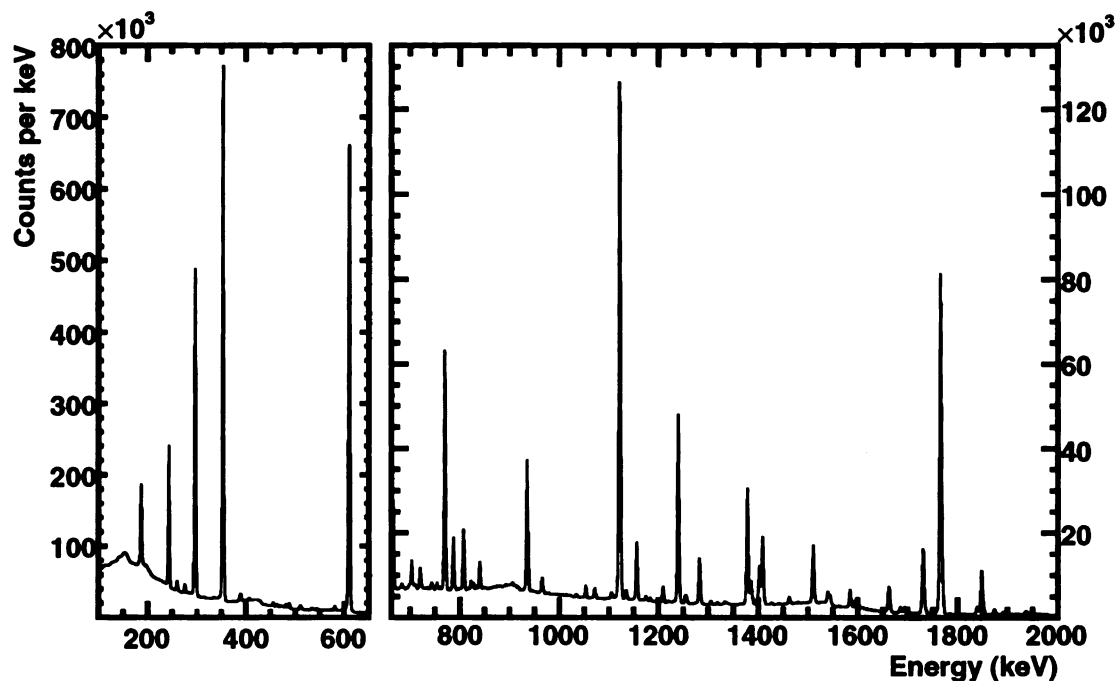


Figure 3.1: Calibrated  $^{226}\text{Ra}$  energy spectrum of all 16 SeGA detectors summed.

To determine these coefficients, a  $^{226}\text{Ra}$  radioactive source was placed in the target position of the array, and the gamma rays with known energies from 186 keV to 2448 keV were detected in the individual detectors. A Gaussian with a quadratic background was fit to each of the photopeaks in the resulting gamma ray spectrum in order to extract the centroid channel of the ADC output. The calibration coefficients for each detector were chosen such that they minimized the chi squared comparing the calculated energies,  $E$ , in the detector and the known peak energies,  $E_i$ .

$$\chi^2 = \sum_i \frac{(E - E_i)^2}{\sigma^2} \quad (3.2)$$

where  $\sigma^2$  is the variation associated with the fitting of the peak. After calibration, the known  $^{226}\text{Ra}$  spectrum is reproduced beautifully as seen in Fig. 3.1. Over the course of the experiment, calibrations parameters may shift slightly. To account



for this possibility, calibration data were taken at the beginning and the end of the experiment. In addition, an abrupt shift in the response of several of the detectors was observed in the middle of the experiment. This was ameliorated by performing a linear correction to the calibration coefficients based on natural background sources in the experiment, in particular the electron-positron annihilation peak and peaks associated with natural potassium decay. These adjustments allowed for an accurate calibration for all the detectors across all the runs.

The proper calibration of the energies deposited in individual segments is also important as the energies of the segments is what the Doppler reconstruction algorithm relies on. The usual technique used is to gain match the segment energies such that it agrees with the central contact energy. One such calibration method is described in Hu et al. [58] where an automated procedure is important as a typical SeGA configuration has  $\sim 500$  segments which need calibration. One benefit to matching with the central contact energies is that all the data including events with incomplete  $\gamma$ -ray absorption can be used in the calibration. However, there are a sizable number of events where the measured energy deposited in the segments is deficient compared to the amount deposited in the central contact. These outliers can cause a simple  $\chi^2$ -analysis to have small negative deviations from the expected results. To alleviate such deviations, an iterative approach was utilized to obtain the segment energy calibration parameters. With each pass, events with large deviations between a single segment energy deposit and the central contact energy were excluded from the analysis. The last pass rejected events which strayed more than 5 keV from the expected value from the central contact. At each pass, parameters were determined for each segment which minimized the  $\chi^2$  of the segment energy relative to the central contact energy. The response of the segments is significantly less linear, so a quartic polynomial was used in the fit to the central contacts. There exists an electrical coupling in between the segments, however, which causes a correlation in the energies determined

from the segments. This can be accounted for by considering additional energy calibration parameters which depend on the coupling between two segments. For events which had interactions in two segments, the calibration included parameters from the cross-terms of the ADC channel outputs  $x_1$  and  $x_2$  up to the fourth power. This can be expanded to the events which interact more than twice in the detectors using the technique discussed in Venutrelli et al. [59].

## 3.2 Efficiency calibration

The efficiency of the detectors must also be accurately determined. This is especially important for the measurement of the partial cross section to the ground state following the knockout reaction. To investigate the  $\gamma$ -ray angular distribution, one also needs to know the relative efficiency of the two rings of detectors in SeGA. The efficiency depends heavily on the energy of the incoming photon and this energy dependence needs to be well understood. The efficiency is also strongly influenced by the geometry of the array relative to the target especially during in-beam experiments where the energy and solid angle depend on the relativistic kinematics and in particular the angle of the detectors with respect to the beam line.

To determine the efficiency, several radioactive sources were placed in the same position as the in-beam target prior to the experiment. For absolute efficiency measurement, the radioactivity of the source must be well-known. To this end, a calibrated source of  $^{152}\text{Eu}$  was used with an activity of  $8.46 \mu\text{Ci}$  measured on 1 May 1978.  $^{152}\text{Eu}$  has a well-known half-life of  $13.537 \pm .006$  years. The intensity of gamma rays,  $I_0$ , emitted can be calculated giving the efficiency,  $\epsilon$ , of the germanium array.  $^{152}\text{Eu}$  only provides a good efficiency calibration for energies up to 1.5 MeV. To determine the efficiency above 1.5 MeV, a  $^{56}\text{Co}$  source was used which has high energy peaks up to 3.5 MeV. The intensity of the cobalt source was not as well known, so a scaling

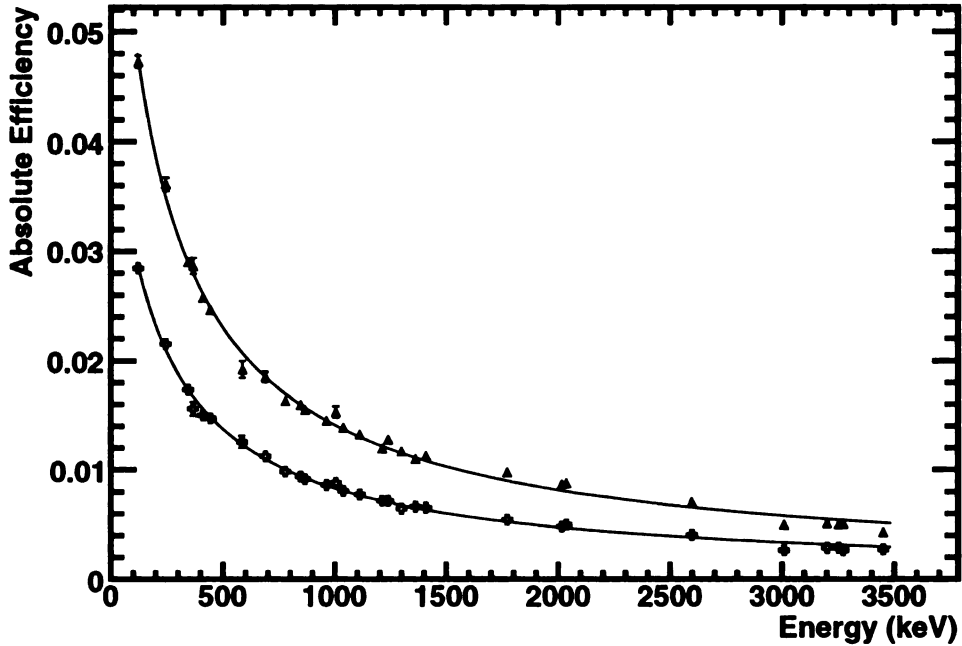


Figure 3.2: SeGA efficiency in the 37° ring (crosses) and the 90° ring (triangles) with associated fits in the form of Eq. 3.3.

factor was applied to agree with the efficiencies in the common energy range with  $^{152}\text{Eu}$ . The energy dependence was then fit as a curve to the discrete data points to get the continuous energy dependence of the efficiency. Several functional forms were tested producing comparable results. The efficiency was finally taken to be of the form

$$\epsilon(E; \epsilon_0, E_0, a) = \epsilon_0(E - E_0 + e^{-0.269E})^{-a} \quad (3.3)$$

with the parameters  $\epsilon_0, E_0, a$  determined by minimizing the chi-squared from the fit. For a 1 MeV photopeak emitted from a source at the target position, SeGA had a 2.2% efficiency. The efficiency was also determined for each ring in the array to understand the dependence of the efficiency on different angles of emission. The measured efficiency is displayed in Figure 3.2. The uncertainty in the efficiency was also determined across the range of energies. If the  $\chi^2$  is minimized at some value

$\chi_0^2$ , then the set of parameters included in the  $n\sigma$  error band are defined as

$$\{\epsilon_0, E_0, a : \chi^2(\epsilon_0, E_0, a) < \chi_0^2 + n^2\}. \quad (3.4)$$

The minimum and maximum values of the efficiency for this set of parameters are then determined for each given energy. Since the fit parameters are highly correlated, an evenly spaced mesh over the parameter space was taken with the variation along the principle axes of the error matrix  $M$ . The error matrix for a set of parameters  $\{c\}$  is defined as:

$$M_{ij} = \frac{\partial^2 \chi^2(\{c\})}{\partial c_i \partial c_j} \quad (3.5)$$

This allows for a more accurate sampling of the parameter space. However, this method always underestimates the width of an error band for a given energy. The granularity of the mesh was made progressively finer until there was a negligible change in the width of the error band. The error in the intensity  $I$  from a source with  $N$  counts in the photopeak is then accordingly

$$f_I(E_i) = \sqrt{f_N(E_i)^2 + f_\epsilon(E_i)^2} \quad (3.6)$$

where  $f_I, f_N, f_\epsilon$  describe the relative errors in the intensity, photopeak counts, and efficiency respectively. The relative uncertainty in the efficiency was reasonably constant over the sampled energy range contributing roughly a 1% additional uncertainty in the determination of the  $\gamma$ -ray intensity in the lab frame.

### 3.3 Polarization sensitivity determination

The sensitivity of SeGA to linear polarization was determined using gamma rays emitted from a  $1 \mu\text{Ci } ^{249}\text{Cf}$  source which provides gamma rays of a known polarization

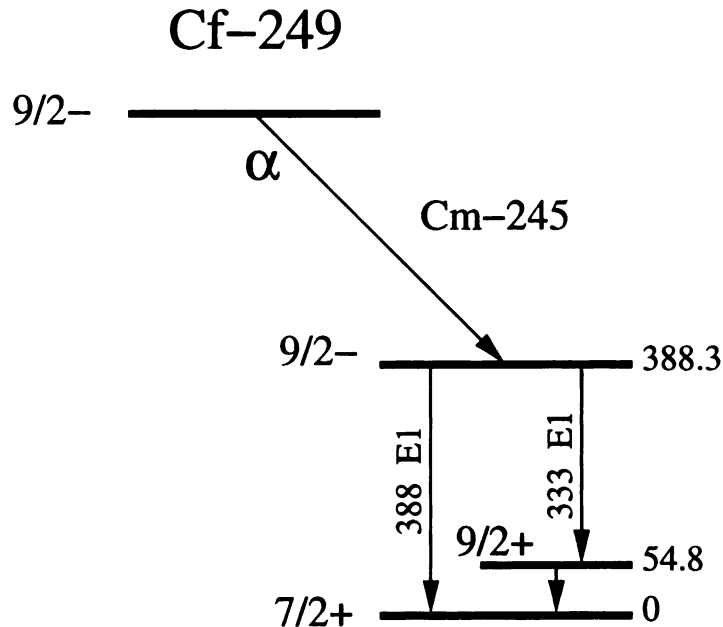


Figure 3.3: Simplified decay scheme of  $^{249}\text{Cf}$  used to produce gamma rays of a known linear polarization.

[53, 60]. Following the  $\alpha$  decay of  $^{249}\text{Cf}$  (see Fig. 3.3), the daughter nucleus  $^{245}\text{Cm}$  emits either a 333 keV or 388 keV gamma ray, both of which are pure electric dipole transitions. The 333 keV and 388 keV gamma rays have an opposite sign for the polarization which allows for control of systematic errors in the measurement.

### 3.3.1 Detector setup

The  $\alpha$  particles were detected with a 400  $\mu\text{m}$  thick silicon surface barrier detector which was located 11 cm from the  $^{249}\text{Cf}$  source. The recoiling heavy ions were stopped in the 2-mil platinum foil backing of the source. Fifteen SeGA detectors were mounted in the classic frame identical to the configuration used in the in-beam experiment as shown in Figure 3.4. Standard analog electronics for SeGA and the silicon detector

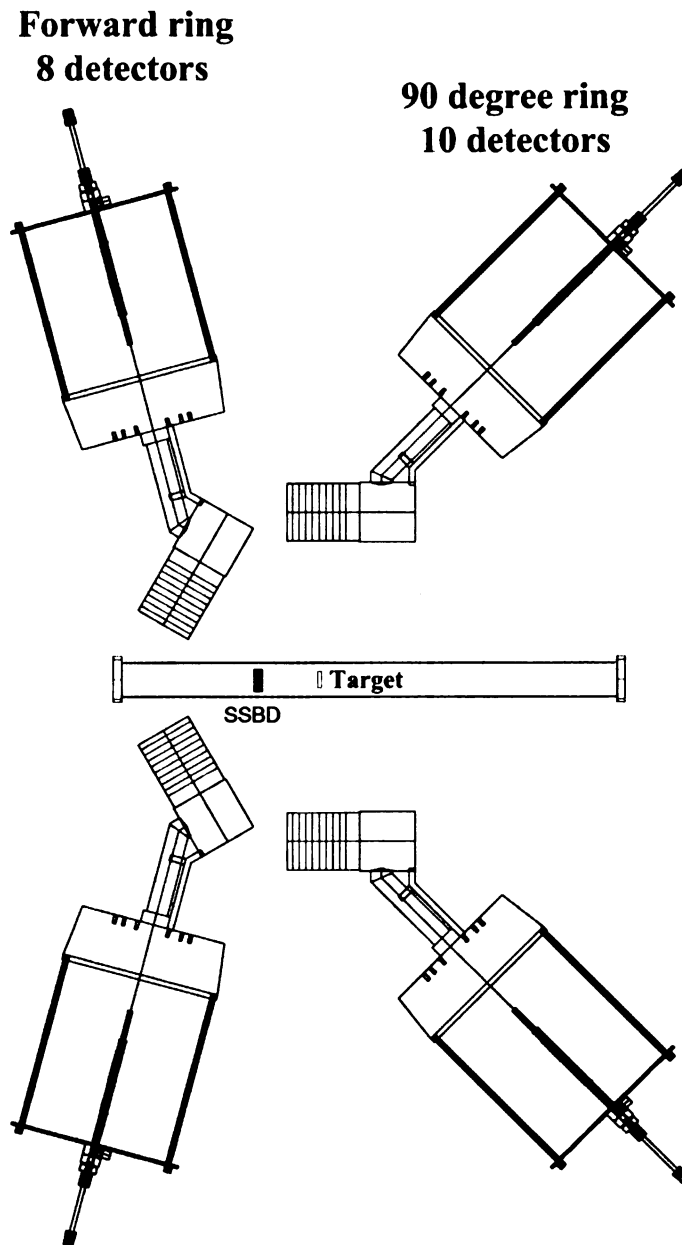


Figure 3.4: The setup used for the  $\alpha$ - $\gamma$  coincidence measurements to determine the polarization sensitivity.

controlled the data acquisition to capture  $\alpha$ - $\gamma$  coincidences as well as gamma rays when the  $\alpha$  particle was not detected. For the 333 keV transition, each detector registered roughly 25,000 gamma ray singles as well as 7,000 coincidences. The more intense 388 keV transition provided four times as much statistics for the analysis. The gamma ray singles provide information about the normalization of the scattering within the detector in response to unpolarized gamma radiation.

### 3.3.2 Gamma-ray angular distribution

The two electric dipole transitions in the daughter nucleus were analyzed for angular distribution. Since these are known to be pure dipole distributions, the  $\gamma$ -ray angular distribution coefficients and linear polarizations are well understood. For pure dipole transitions, the polarization at an angle is completely determined by Eq. 2.13 given the angular distribution coefficient  $a_2$ . The angular distribution can be observed from the spectra for detectors at different angular positions as shown in Figure 3.5. The number of  $\alpha$ - $\gamma$  coincidences in the experiment is given by

$$N_d(\theta) = N_0 \epsilon_{\alpha,\gamma}(E_\alpha, E_\gamma, \theta) (1 + a_2 P_2(\cos \theta)) \quad (3.7)$$

where  $N_0$  is the number of gamma rays emitted and  $\epsilon_{\alpha,\gamma}$  is the efficiency to detect  $\alpha$ - $\gamma$  coincidences for a given combination of energies. This is related to the detection efficiency of the individual detectors:

$$\epsilon_{\alpha,\gamma}(E_\alpha, E_\gamma, \theta) = \epsilon_\alpha(E_\alpha) \epsilon_\gamma(E_\gamma, \theta) \quad (3.8)$$

Singles were also taken concurrently to provide a tool for proper normalization of the relative detection efficiency of each ring. As the number of singles greatly outnumbers the number of coincidences, a down-scaler was used to minimize the dead time of the

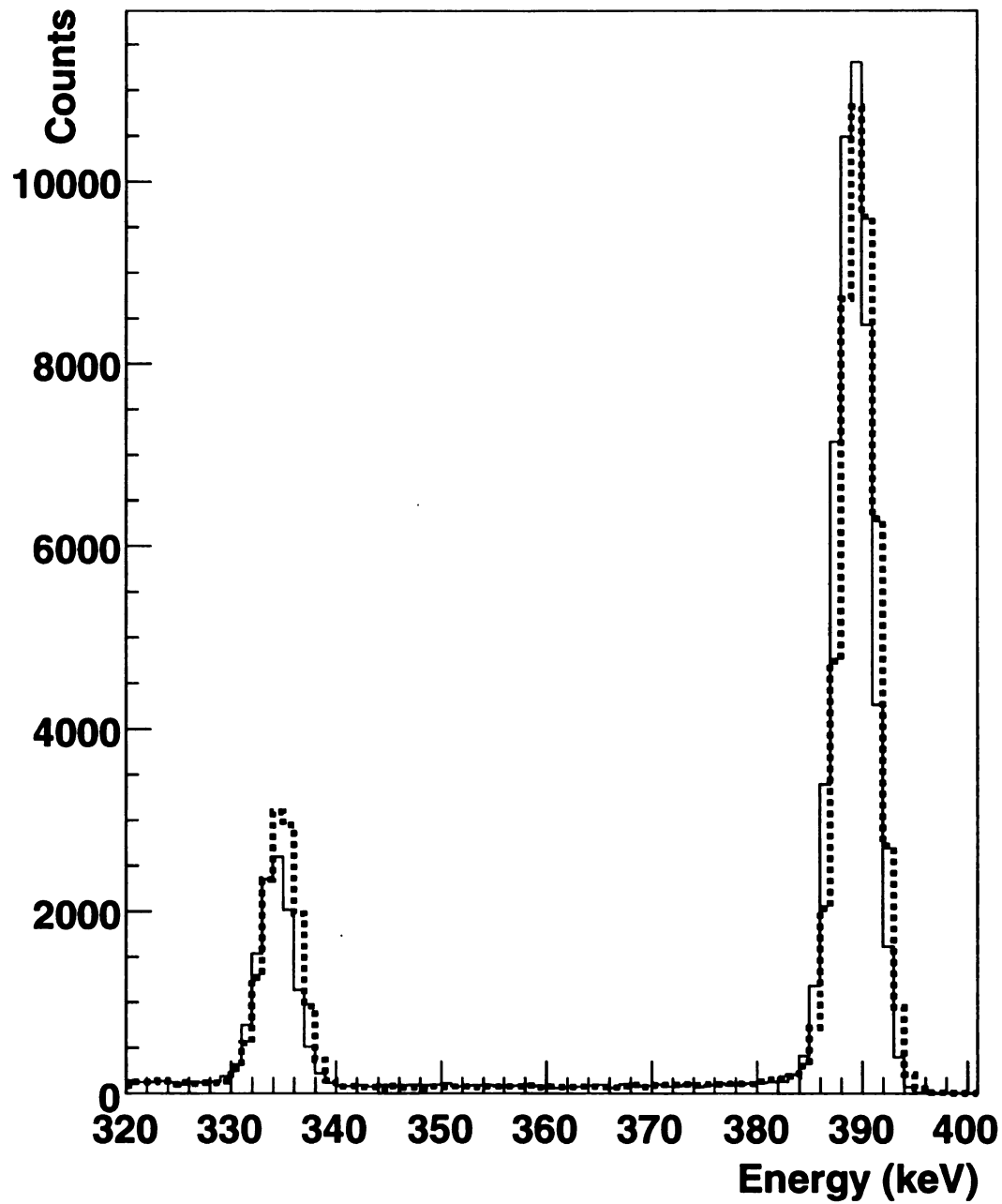


Figure 3.5: Gamma-ray spectrum for a detector in the forward (solid) and backward (dashed) rings in SeGA for the two gamma ray transitions in the  $^{245}\text{Cm}$  following the  $\alpha$  decay of  $^{249}\text{Cf}$  showing the difference in the angular distribution.



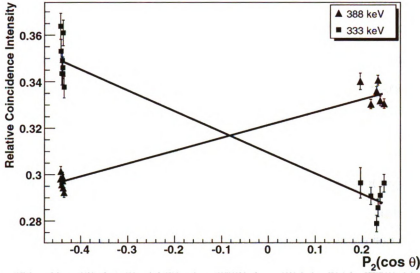


Figure 3.6: The ratio of counts for the  $\alpha$ - $\gamma$  coincidences to singles for each of the detectors in the array with the line fit which determines the angular distribution coefficient  $a_2$  for the two gamma ray transitions of interest.

acquisition system by reducing the  $\gamma$ -ray singles which created a trigger. The number of down-scaled singles is given by

$$N_s(\theta) = \frac{N_0 \epsilon_\gamma(E_\gamma, \theta)}{f_{DS}} \quad (3.9)$$

where  $f_{DS}$  is the downscaling factor. The ratio of the number of coincidences and singles is linear in  $P_2$  considering the attenuation due to the finite angular extent of the detector:

$$\frac{N_d(\theta)}{N_s(\theta)} = f_{DS} \epsilon_\alpha(E_\alpha) W_{av}(\theta), \quad (3.10)$$

where  $W_{av}(\theta)$  is the average of the angular distribution over the detector solid angle. The ratio is independent of the individual detectors' efficiencies. From the analysis of the ratios, the  $a_2$  coefficients for the 333 keV and 388 keV gamma rays are respectively  $-0.29 \pm 0.02$  and  $0.17 \pm 0.01$  from the fit determined in Figure 3.6. This agrees with previous measurements done for the  $^{249}\text{Cf}$  nucleus [60].

### 3.3.3 Scattering asymmetry normalization

The scattering of unpolarized gamma rays was analyzed for the intrinsic asymmetry due to the geometry of the detector. Where no  $\alpha$  particle was detected, the gamma rays emerge unpolarized as there is no axis of alignment in the system. The ratio  $a$  (Eq. 2.10) which describes the geometric asymmetry was measured for both of the gamma rays of interest for each detector. Events were chosen within the photopeak that interacted in only two segments within a single SeGA detector as shown in Figure 3.7. Over this energy range, the change in the asymmetry for unpolarized gamma rays was negligible:  $a(333) = 0.126 \pm 0.007$  and  $a(388) = 0.128 \pm 0.007$  for the weighted average over all the detectors. The uncertainty is dominated by individual differences in the detectors' intrinsic asymmetries. The standard deviation for the sample of detectors for the geometric asymmetry is  $\sigma = 0.009$ . It is important to note that the selection of events which scatter parallel or perpendicular to the reaction plane account for respectively 25% and 3% of the photopeak events in this energy range. The scattering angle is close to  $90^\circ$  where the cross section (Eq. 2.4) is most sensitive to the polarization for low-energy gamma rays.

The dependence of the geometric asymmetry on the energy was also investigated over a larger range by examining gamma rays emitted from a  $^{152}\text{Eu}$  source (see Fig. 3.8). The europium source validates that the change in the intrinsic geometric asymmetry over a narrow energy range is small. The intrinsic asymmetry was characterized by a linear fit  $a = c_0 + c_1 E$  with the energy dependence contained in the  $c_1$  coefficient which was determined to be  $(-1.24 \pm 0.15) \cdot 10^{-5} \text{ keV}^{-1}$ .

### 3.3.4 Sensitivity determination

Using each detector's geometric asymmetry from the singles measurement, the asymmetry  $A$  (Eq. 2.11) in the scattering was observed for the  $\alpha$ - $\gamma$  coincidences. The

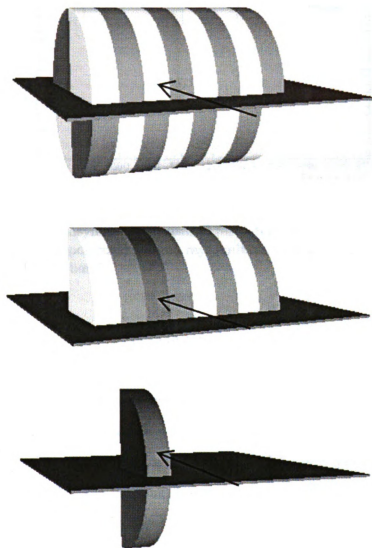
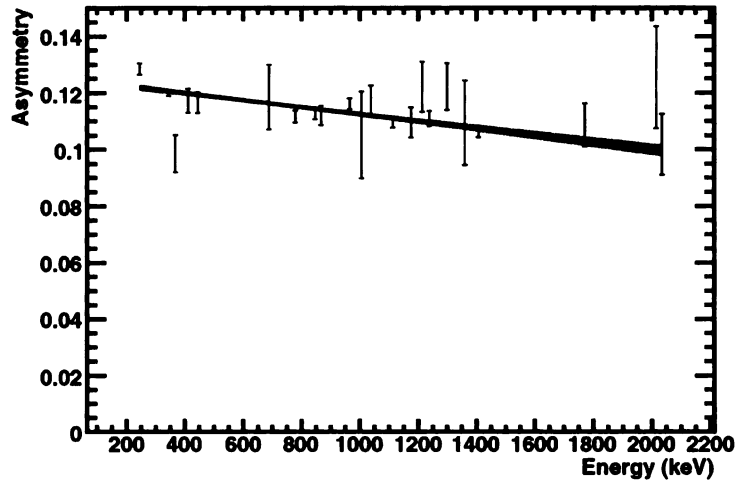


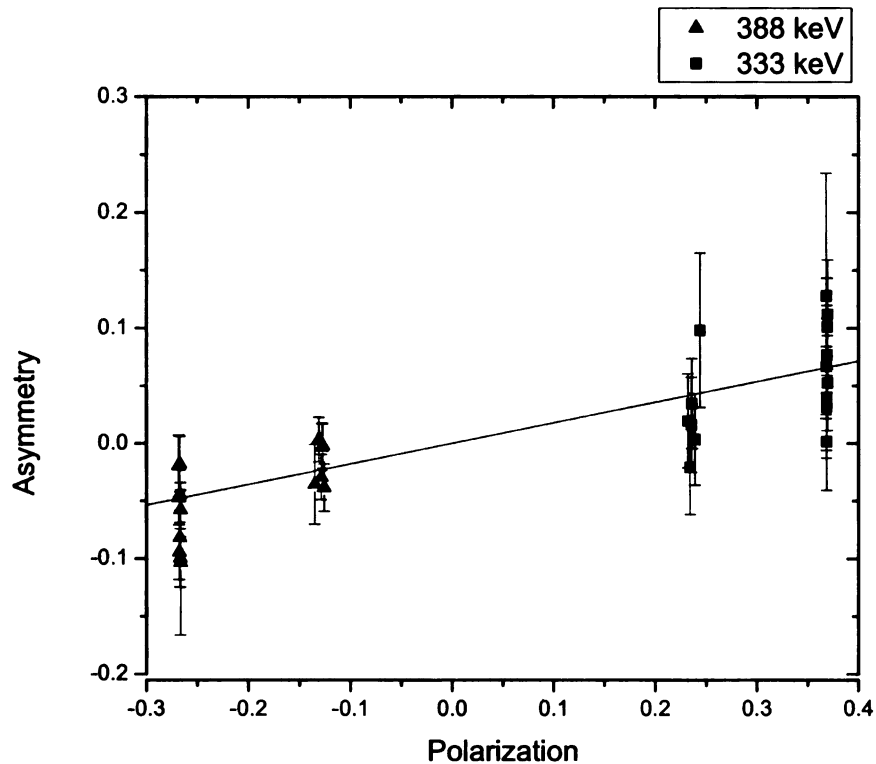
Figure 3.7: (Top) The geometry of a SeGA detector with respect to the reaction plane. Gamma rays irradiate the detector from the side of the cylindrical axis and interact within a given segment and then scatter either parallel (middle) or perpendicular (bottom) to the reaction plane.



**Figure 3.8:** Geometric asymmetry measured for detectors in the forward ring for a range of energies for unpolarized gamma rays emitted from a  $^{152}\text{Eu}$  source. Included is a linear fit and error band.

effect of the finite angle span of the detector causes a small uncertainty of 1% for the polarization of the incoming gamma ray. The incoming polarization determined from the angular distribution coefficient was averaged over the solid angle of the detector. With this correction, the polarization of the two pure dipole transitions of interest was  $-0.267 \pm 0.007$  and  $0.24 \pm 0.02$  for the 388 keV and 333 keV gamma rays detected in the forward ring. For the  $90^\circ$  ring, the incoming polarizations were respectively  $-0.13 \pm 0.02$  and  $0.37 \pm 0.02$  for the transitions.

The observed scattering asymmetry  $A$  in the detectors for the four known gamma ray polarizations was  $-0.08 \pm 0.03$ ,  $-0.02 \pm 0.03$ ,  $0.04 \pm 0.04$ , and  $0.10 \pm 0.04$  (from lowest to highest polarization) for the weighted average over the relevant group of detectors as shown in Figure 3.9. The asymmetries were compared to the maximum analyzing power of an ideal Compton polarimeter (Eq. 2.9). The relative sensitivity,  $Q_{\text{rel}} = Q/Q_0$  was established to be  $0.18 \pm 0.02$ .



**F**igure 3.9: The asymmetry observed in the SeGA detectors for gamma rays of four known polarizations adjusted for the relative analyzing power of the Compton effect for the two different energies.

### 3.3.5 Figure-of-merit discussion

Understanding the true effectiveness of the setup to detect the linear polarization must include the time necessary to make a sensitive measurement. Efficiency of detecting the gamma rays plays an important role here. The figure-of-merit,

$$F = Q^2 \epsilon_c, \quad (3.11)$$

for a Compton polarimeter as defined by Logan et al. [61] takes into consideration the sensitivity  $Q$  as well as the coincidence efficiency,  $\epsilon_c$ , in regard to the intra-detector scattering [62]. The coincidence efficiency takes into account the photopeak efficiency,

Table 3.1: Comparison of SeGA to other detector arrays for polarization measurements.

	$Q_{\text{rel}}$	$Q$	$\epsilon_c \times 10^4$	$F \times 10^6$
POLALI [49]	0.8 <i>2</i>	0.5 <i>1</i>	0.26	7 <i>1</i>
Clover (EUROBALL) [50, 63]	0.29 <i>2</i>	0.23 <i>2</i>	4.8	25 <i>2</i>
Gammasphere [36, 64]	0.08 <i>1</i>	0.052 <i>7</i>	18	4.8 <i>7</i>
SeGA	0.18 <i>2</i>	0.14 <i>2</i>	3.0	5.9 <i>8</i>

$\epsilon_{p\omega}(E_\gamma)$ , of the detector as well as the likelihood of events to scatter in the detector in a manner which contributes to the polarization data.

$$\epsilon_c(E_\gamma) = \frac{(N_{\parallel} + N_{\perp})/2}{N_{\text{tot}}} \epsilon_{p\omega}(E_\gamma) \quad (3.12)$$

For a single SeGA detector in this energy range, the total photopeak efficiency is approximately  $21.2 \cdot 10^{-4}$ . Since 25% and 3% of the events scatter parallel and perpendicular to the reaction plane respectively, the coincidence efficiency for polarization is  $\epsilon_c \approx 2.99 \cdot 10^{-4}$  for a single detector. This gives a figure-of-merit which is  $F \approx 5.9 \cdot 10^{-6}$  which by its definition is inversely proportional to the time necessary to make a measurement of a certain precision with the device.

This figure-of-merit for SeGA detectors is similar within an order of magnitude to other detectors. For some other detectors referenced in the literature, the main values of interest are listed in Tab. 3.1. The sensitivity has been extrapolated from the literature to the same energy range as in the  $^{249}\text{Cf}$  measurement. The photopeak efficiency was estimated based on available efficiency plots and the figure-of-merit has been calculated according to Eq. 3.11. The errors quoted in Tab. 3.1 are based solely on the uncertainties of the sensitivities. Including the uncertainty in the estimation of the efficiency, these figure-of-merit values are gauged to be 30% accurate. Compared to the Clover results [50, 63], an individual SeGA detector has approximately one fifth the sensitivity. A third of this is due to a reduced sensitivity. The remainder is attributed to the decreased photopeak efficiency of the detector due to a smaller

volume. A standard 5-crystal arrangement, such as POLALI, has a worse figure-of-merit due to its limited efficiency. Each of these detectors are particularly suited for specific purposes though, such as SeGA's performance for in-beam  $\gamma$ -spectroscopy. The signal-to-noise ratio in each individual experiment, which is not considered in Tab. 3.1, should also be considered when determining the impact of a detector's figure-of-merit.

## Chapter 4

### Proton knockout studies

After characterization, the detectors were utilized in an experiment to investigate the structure of the island of inversion odd- $A$  isotopes  $^{31,33}\text{Mg}$ . In particular, the magnesium isotopes were populated from proton knockout reactions of a secondary beam of aluminum isotopes which were produced by the methods of Subsection 2.2 at the Coupled Cyclotron Facility at National Superconducting Cyclotron Laboratory. After acceleration, the fully-stripped 80 pA primary beam of  $^{48}\text{Ca}$  had a kinetic energy of 140 MeV/u, corresponding to a velocity approximately 50% the speed of light. The primary beam was fragmented on a  $806.2 \text{ mg/cm}^2$   $^9\text{Be}$  target ( $\sim 4$  mm thick). The A1900 filtered out the  $^{32,34}\text{Al}$  isotopes to investigate the reaction of interest. The secondary beam characteristics are described in Table 4.1. A fraction of the secondary beam was still composed of impurities resulting from the fragmentation process but these can be cleanly separated in the analysis. The magnetic rigidity was chosen in order to select nuclei with kinetic energy of 95 MeV/u corresponding to a velocity  $\beta = v/c = 0.42$ . Each fully-stripped beam of  $^{32}\text{Al}$  and  $^{34}\text{Al}$  was then directed to the S800 spectrograph where they underwent reactions on a secondary beryllium reaction target. The reaction residues were identified in the S800 spectrograph. Particular focus was given to the spin alignment in the magnesium isotopes



Table 4.1: Secondary beam characteristics.

Beam property	$^{32}\text{Al}$ setting	$^{34}\text{Al}$ setting
$(B\rho)_{12}$ (T·m)	3.8143	4.0789
$(B\rho)_{34}$ (T·m)	3.5179	3.7858
$E_{34}$ (MeV/u)	93.84	94.61
Rate (pps/pnA)	2600	153
Purity	71%	50%
$\Delta p/p$	0.5%	0.5%
Transmission to S800	85%	80%

following the reaction by examining the angular distribution of gamma rays emitted from the reaction products. Also, for the first time with intermediate-energy beams, the linear polarization of emitted gamma rays was probed. This allows direct access to information about the structure of the states, separating those with intruder-like configurations from those with standard shell ordering.

## 4.1 Electronics trigger

To successfully probe the structure, one must combine the information from the incoming and outgoing beams as well as any detected gamma rays. It is important to correlate all the constituent parts of each event at the target. The bulk of the information is contained in the gamma-rays correlated with the particles detected in the focal plane of the S800. However, not every reaction will result in emitted gamma rays. Furthermore, the emitted gamma rays may not interact with the SeGA detectors. This is opposed to the particle detection efficiency where the ion chamber of the S800 can be considered to be 100% efficient for residues within the S800 momentum and angular acceptance. To determine an inclusive cross section to all the bound states in the residue, one must consider the total number of particles produced in the reaction whether or not a gamma ray was detected. However, measurement of the partial cross sections to individual states requires accurate determination of the

number of particle- $\gamma$  coincidences.

For the purpose of the above measurement, real-time selection of events is enabled in the hardware through an electronics trigger. After a particle is detected by the E1 scintillator at the end of the S800 focal plane, a coincidence window ( $\sim 400$  ns) is opened. A logical OR of all the gamma-ray detectors produces the coincidence trigger if a gamma-ray interacts with a detector within the coincidence window. The master trigger consisted of all coincidence triggers combined with a fraction of the particle singles where no gamma ray is detected. This master trigger prompted the electronics to be read out. The fraction of particle singles allowed was chosen that the live time of the data acquisition system was not adversely affected ( $\gtrsim 90\%$ ). Slight corrections were made to timing in each trigger scenario due to the different responses of the components of the master trigger.

## 4.2 $^{31}\text{Mg}$

### 4.2.1 Beam characteristics and particle ID

The large secondary beam intensity of  $^{32}\text{Al}$  (see Table 4.1) allowed the use of a thin secondary reaction target of 1 mm ( $185 \text{ mg/cm}^2$ ) beryllium at the S800 target position. At the end of the A1900 fragment separator, the  $^{32}\text{Al}$  secondary beam was 71% pure having a dominant contaminant of  $^{33}\text{Si}$ . This impurity could be clearly separated in the analysis based on the time of flight from the A1900 extended focal plane to the object box of the S800 as shown in Fig. 4.1. The outgoing residues passed through the S800 magnetic dipoles selecting the reaction products of interest. The unreacted  $^{32}\text{Al}$  isotopes are removed in the process. However, the properties of the incoming beam are necessary for the proper analysis of the experiment, so an additional set of data was taken with the S800 tuned to the magnetic rigidity of the unreacted secondary beam. In these runs, the primary beam was attenuated to reduce

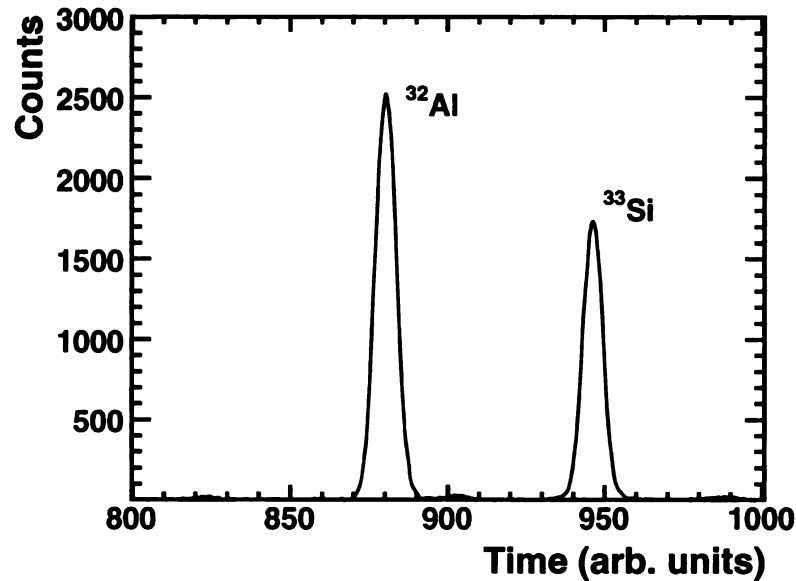
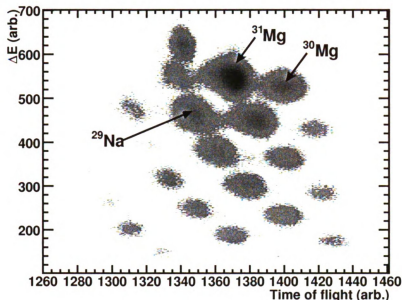


Figure 4.1: The incoming  $^{32}\text{Al}$  particles identified by the time of flight from the extended focal plane of the A1900 magnetic separator to the object box of the S800 spectrograph.

The rate on the focal plane detectors as the high intensity ( $> 5000$  Hz) would impact their performance.

During the magnesium production runs, the outgoing residues were identified on an event-by-event basis using the energy lost in the ion chamber at the focal plane of the S800 as well as the time of flight from the object to the  $E1$  scintillator of the S800. The time of flight was corrected to improve the resolution based on the kinematic information provided by the CRDCs at the focal plane. The outgoing residues can then be clearly identified as shown in Fig. 4.2. The information provided by the CRDCs also allowed the accurate determination of the outgoing momentum vector of the nuclei relative to the central trajectory of the S800.

The mean velocity of the residues in the middle of the target was determined to be  $\beta = 0.404 \pm 0.002$  by the methods discussed in Subsection 2.4.5. For residues with this velocity, the emitted gamma rays detected by SeGA are Doppler broadened



**Figure 4.2:** Outgoing residues for a reaction of an incoming  $^{32}\text{Al}$  beam identified by the S800 spectrograph based on the energy loss in the ion chamber and their time of flight with selected isotopes of interest labeled.

with a FWHM of 48 keV (2.7%) in the downstream ring and 38 keV (2.1%) in the upstream ring for a 1.8 MeV gamma ray. Using the additional information about the outgoing particle momentum from the tracking through the S800, the gamma-ray resolution can be further improved by about 10%. The major improvement was from determining the velocity of the individual particles relative to the central trajectory of the S800.

Also, it is important to note that at this velocity the forward ring of SeGA is located at a center-of-mass angle of  $54^\circ$  where  $P_2(\cos\theta_{c.m.}) = 0.009(3)$ . This limits any effects from the angular distribution in the forward ring allowing for accurate determination of  $\gamma$ -ray branching ratios from excited states. Higher orders of the angular distribution are assumed to be negligible.

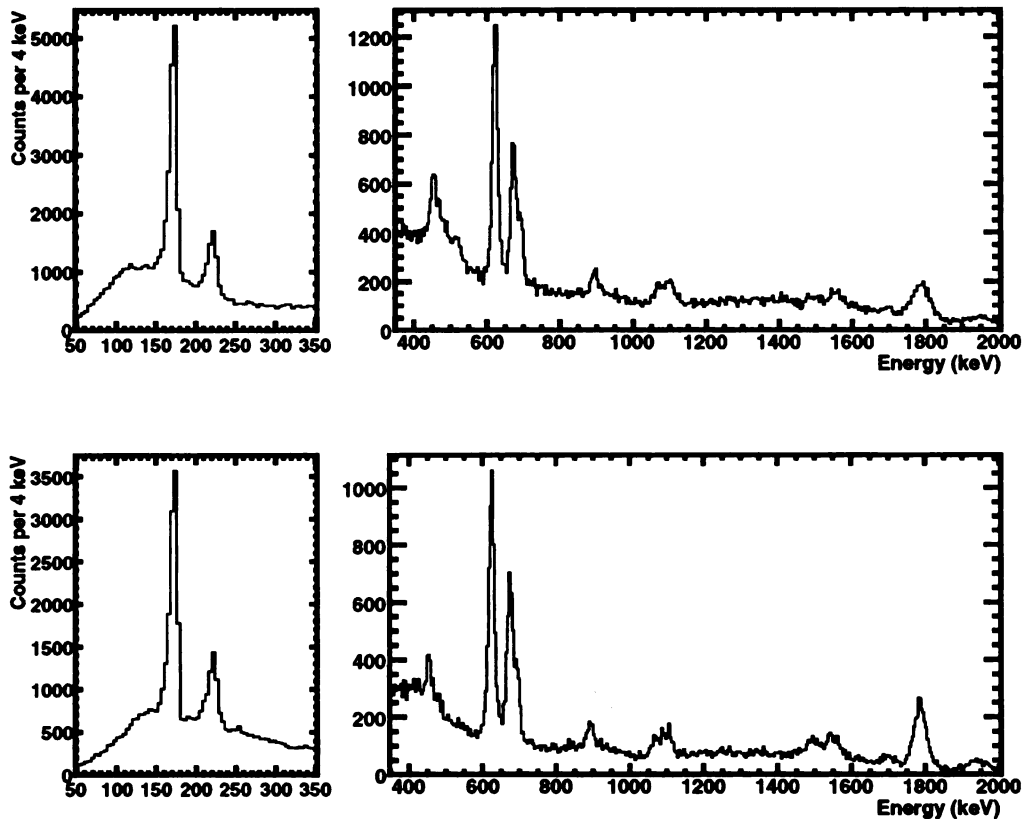


Figure 4.3: Gamma-ray spectrum of  $^{31}\text{Mg}$  in the forward (top) and backward (bottom) rings of SeGA; note the marked increase in resolution in the backward ring for the high energy 1.8 MeV gamma ray.

#### 4.2.2 Level scheme

Gamma rays emitted from  $^{31}\text{Mg}$  were detected in SeGA with the resulting spectrum shown in Fig. 4.3. Detailed information about the gamma rays observed is listed in Table 4.2 where the intensities have been determined using the observed counts and the Doppler-corrected efficiency which accounts for both the Lorentz boost of the solid angle as well as the Doppler shift in the gamma ray's energy. Most of these gamma rays were observed in previous experiments [23, 65, 66]. The energies of these transitions agree well with their formerly established values. Furthermore, the relative intensities of gamma rays originating from an initial state are consistent with the

Table 4.2: Gamma-ray transitions observed in the current experiment with their intensities, angular distribution coefficients, and Compton scattering asymmetries.

$E_i$ (keV)	$E_f$ (keV)	$E_\gamma$ (keV)	$I_\gamma^a$	$a_2$	A
221.1	50.5	171.1 <sup>b</sup>	77 (4)	0.48 (10)	
	0.0	221.1 <sup>b</sup>	24.2 (15)	-0.8 (3)	
673.2	221.1	452.6 (6)	13.2 (18)		
	50.5	623.3 (5)	64 (4)	0.02 (20)	-0.04 (5)
	0.0	673.2 (7)	34.2 (23)	-0.7 (3)	-0.08 (6)
944.5	50.5	894.4 (13)	9.0 (17)	-0.4 (8)	
1154.5	461	692.6 (8)	16.8 (14)	-0.4 (5)	-0.07 (9)
2014.5	944.5	1072.7 (19) <sup>c</sup>	10.1 (16)	0.3 (8)	
	461	1555.7 (22) <sup>c</sup>	24 (3)	0.5 (9)	
	221.1	1793.4 (18)	100	0.29 (18)	
unplaced		1104.0 (16)	13.0 (19)		
		1500.1 (24)	13 (3)		
		1707 (3)	15 (8)		
		1936 (4)	9 (4)		
		1968 (4)	17 (5)		

<sup>a</sup> Normalized to 1793 keV transition

<sup>b</sup> Established values since measured values are subject to effects due to the previously measured lifetime of the state [65]

<sup>c</sup> Tentatively placed in the decay scheme based on energy balance

Branching ratios seen in previous experiments. This gives credence to the established placement of these gamma rays in the level scheme of <sup>31</sup>Mg. However, as the population mechanism is different in this experiment than the neutron-knockout study [23] and  $\beta$ -decay studies [65,66], several gamma rays were seen with a significantly higher intensity than in the previous experiments.

Information available in the experiment allowed for the placement of one new level at 2015 keV. The placement of this level was established based on background-subtracted  $\gamma$ - $\gamma$  coincidences of the 1793 keV gamma ray with decays from the 221 keV state. The coincidence spectrum is shown in Fig. 4.4. The gates for background subtraction were taken below the 171 keV peak and above the 221 keV peak. In the coincidence spectrum, the 453 keV gamma ray which was previously established to feed the 221 keV state [66] is also readily apparent. Also visible is the Compton

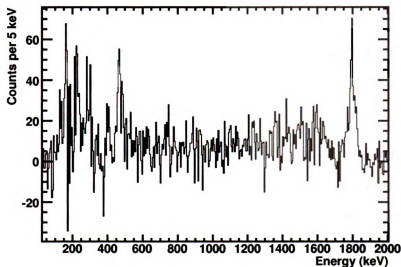


**Figure 4.4:** Background-subtracted gamma-ray spectrum coincident with the known  $\gamma$ -ray decays from the 221 keV state.

edge of the 1.793 MeV gamma rays which interact once within the detector and then Compton scatter outward without depositing their full energy. The Compton scattered gamma rays have a minimum scattering energy according to Eq. 2.5 based on the domain of  $\cos \theta$ :

$$E_{\min} = \frac{E_0}{1 + 2E_0/m_e c^2}. \quad (4.1)$$

In the rest frame, the 1.793 MeV gamma ray emitted towards the forward ring has a Doppler-shifted energy of 2.422 MeV. This corresponds to a minimum energy of 0.231 MeV for the Compton scattered photon, resulting in 2.191 MeV deposited in the detector. When Doppler corrected to the center-of-mass frame, this energy deposit is 1.622 MeV which is where the Compton edge appears in the coincidence spectrum.

No other gamma rays were found to be coincident with the decays from the 221 keV state. As the  $\gamma$ - $\gamma$  coincidence efficiency scales like the singles efficiency squared, only the most intense transitions can provide  $\gamma$ - $\gamma$  data due to the low efficiency of SeGA ( $\epsilon_\gamma \approx 2\%$  implying  $\epsilon_{\gamma,\gamma} \approx 0.04\%$ ). Some gamma rays observed seem to have

energies which are fairly consistent with the difference in between established energy levels and have been tentatively placed in the decay scheme based on this information. The level scheme of  $^{31}\text{Mg}$  with the new information from the present experiment is displayed in Fig. 4.5 including comparisons to the predicted excited states from two theoretical calculations to be discussed in Section 5.1.

Gamma rays which deexcite the 221 keV state have a low-energy tail in the Doppler-corrected peak shape (see Fig. 4.10) that is evidence of a long lifetime which is consistent with the previously measured half-life of 133(8) ps [65]. Given the residue velocity, this corresponds to a traversal distance of 1.76(11) cm in the setup. As the efficiency of SeGA depends directly on the position of the source of  $\gamma$ -ray emission, this contributes an additional systematic uncertainty of about 10% in the intensity which is not quoted in Table 4.2. For the longer-lived 461 keV state, no deexciting 240 keV gamma ray was observed as the 10.5(8) ns half-life corresponds to a long mean flight path of about 3 m which would result in most decays occurring out of the field of view of SeGA.

Several other transitions observed in Terry et al. [23] are also visible in the proton knockout experiment. Five of these remain unplaced in the level scheme which account for a total intensity of 67(11)% of the 1.79 MeV gamma ray transition. Several of these are gamma ray doublets which appear above 1 MeV as shown in Fig. 4.6. There is no clear resolution of the doublet structure for the  $\gamma$ -ray peaks located at 1.1 and 1.9 MeV, but the width of the energy peaks suggest multiple gamma rays with similar energies. These peaks at 1.1 MeV and 1.9 MeV have a FWHM of 4.9% and 3.5% respectively which is considerably larger than the other gamma-ray peaks' characteristic 2.1% relative width. This cannot be solely attributed to the lifetime of the states. The observed FWHM is significantly larger than the estimated 0.5% Doppler broadening resulting from variation of velocity in the target for short-lived states. Longer-lived states decay behind the target at the same post-target velocity with a



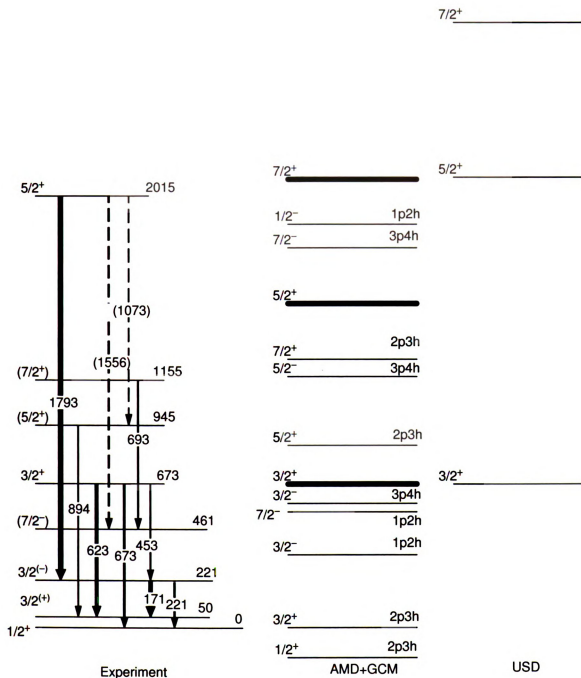


Figure 4.5: (left) The level scheme observed in  $^{31}\text{Mg}$  with suggested spins and parities including tentatively placed gammas (dashed). (middle) AMD+GCM calculations from Kimura et al. [67] with the  $0p1h$  states in bold. (right) The  $0h\omega$  states calculated by the USD shell model interaction. Theoretical calculations have a shift in excitation energy to match the energy of the  $3/2^+$  single-hole state determined by the experiment. See Sections 4.2 and 5.1 for details.

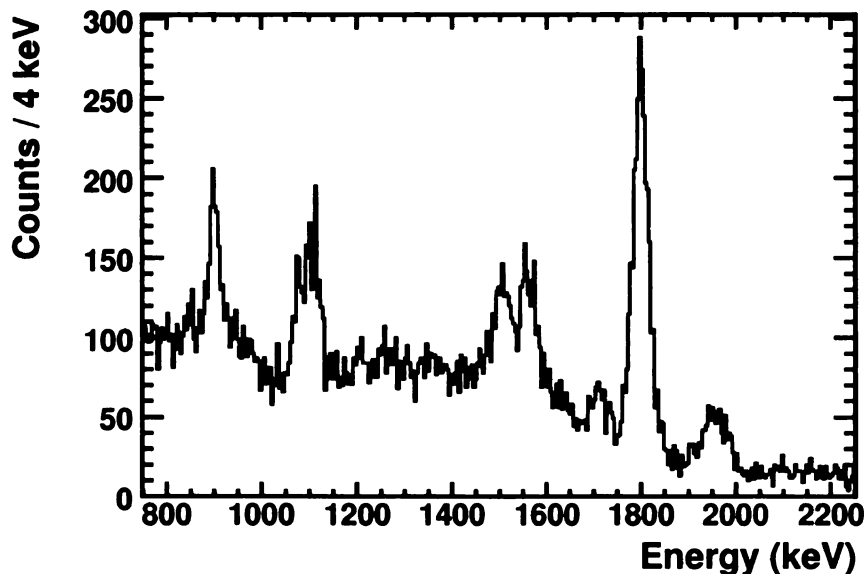


Figure 4.6: Gamma-ray energy spectrum of  $^{31}\text{Mg}$  in the  $90^\circ$  ring of SeGA following Doppler reconstruction, showing several doublets at 1.1, 1.5, and 1.9 MeV.

exponential position distribution downstream of the target. This causes a distinctive  $\gamma$ -ray peak shape (such as in Fig. 4.10) as well as ring-dependent energy shifts in the Doppler-corrected spectrum since the angle changes with the position of the decay. Neither of these effects are apparent, so the additional width indicates the existence of unobserved doublets. The energies of the doublet components were established by a fit which assumed a relative width consistent with that for well-resolved transition in the  $\gamma$ -ray spectrum.

### 4.2.3 Inclusive and partial cross sections

Determination of the knockout reaction cross section requires an accurate measurement of the number of  $^{31}\text{Mg}$  reaction residues, which in turn is related to the number of incoming  $^{32}\text{Al}$  beam particles. In the experiment, there is no direct accurate measurement of the incoming beam particles. However since most of the particles pass through the target without interacting, determining the number of these unreacted

particles after the target yields an accurate measurement of the incoming rate of  $^{32}\text{Al}$  impinging on the target. As the  $^{31}\text{Mg}$  reaction residues cannot be measured at the same time as the unreacted particles, two settings of the S800 spectrograph were used.

In one setting, the S800  $B\rho$  was chosen such that the unreacted particles were centered in the spectrograph. Since the unreacted particles have a small momentum spread and divergence, unreacted particles are detected at the focal plane of the spectrograph with nearly 100% efficiency. The number of particles detected at the focal plane,  $N_i$ , is related to the rate on the scintillator at the extended focal plane of the A1900,  $N_{\text{XFP}}$ , and at the object scintillator,  $N_{\text{OBJ}}$ , via:

$$N_i = \frac{N_{\text{XFP}} + N_{\text{OBJ}}}{2} f, \quad (4.2)$$

with some normalization factor  $f$  which is related to the purity of the beam and the transmission through the S800 analysis line. This normalization factor can then be used to determine  $N_i$  based on the scintillator rates when the S800 is placed on a different  $B\rho$  setting. Two normalization runs were taken with the unreacted incoming  $^{32}\text{Al}$  particles delivered to the S800 focal plane. The normalization factor  $f$  deviated only slightly in the two runs.

For the remainder of the experiment, the S800 was tuned to maximize the acceptance of the  $^{31}\text{Mg}$  reaction products while limiting contamination from the unreacted secondary beam. For a knockout reaction setting, the cross section can then be determined using the scintillator rates and the number of residues detected ( $N_f$ ) in the particle identification plot (Fig. 4.2) using Eq. 1.2. An additional correction had to be applied as the reacted particles have a larger momentum spread and suffer acceptance cuts in the S800 so not all outgoing products are detected. Particles with a low momentum, relative to the central trajectory through the S800, suffer a reduction in angular acceptance in the dispersive direction as displayed in Figure 4.7. To account

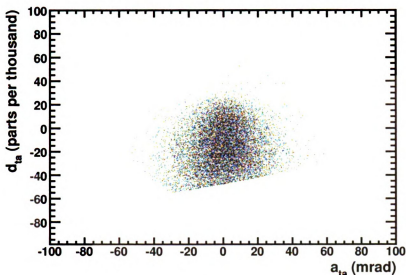


Figure 4.7: The focal plane measurements of  $a_{ia}$  and  $d_{ia}$  showing the acceptance cut for low momentum  $^{31}\text{Mg}$  residues from an incoming  $^{32}\text{Al}$  beam.

for this, a systematic 2.5% correction to the cross section measurements has been made assuming that the angular distribution in the dispersive direction is symmetric with respect to the centroid of the distribution.

The inclusive proton knockout cross section was determined to be 8.7(5) millibarn. Throughout the experiment, the efficiencies of the scintillators were monitored for any change due to irradiation damage which could degrade the particle detection efficiency of the S800 spectrograph or the stability of the normalization factor  $f$ . The stability of  $f$  is further validated by the consistency of the calculated inclusive cross-section on a run-by-run basis (see Fig. 4.8). The systematic uncertainty of 0.5 mb has been determined from the weighted standard deviation of the run-by-run cross sections. This uncertainty is the major constraint on the precision of the measurement, and is related to the consistency of the incoming beam normalization.

The inclusive cross section includes the cross section to the ground state ( $\sigma_0$ ) as well as to excited states ( $\sigma_{ex}$ ). The partial cross sections to excited states were deter-

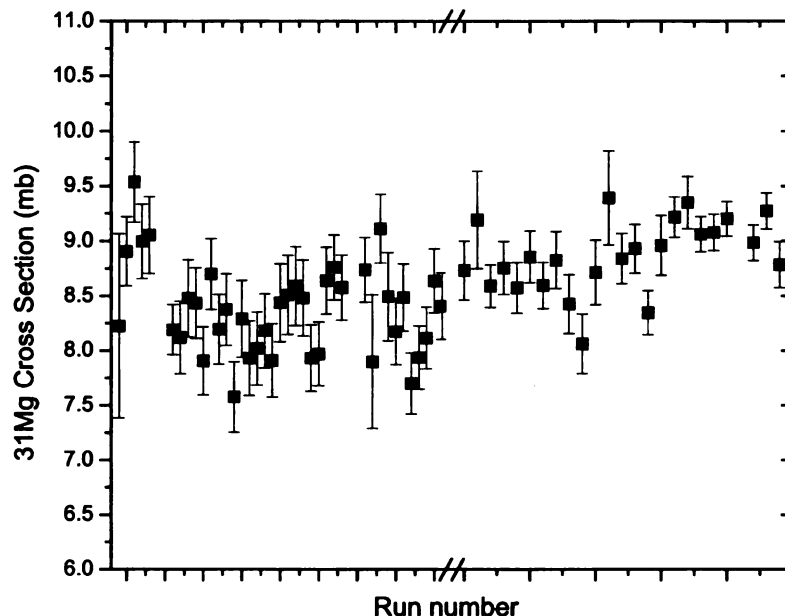


Figure 4.8: Inclusive cross section of  $^{32}\text{Al} \rightarrow ^{31}\text{Mg}$  calculated on a run-by-run basis chronologically from left to right. The experiments with the  $^{32}\text{Al}$  incoming beam were performed in two sets of runs separated by several days corresponding to the break in the abscissa.

mined by particle-gamma coincidences. The cross section to the ground state is the difference between these cross sections to excited states and the inclusive cross section. The direct population to each excited state  $I_j$  was determined by the balancing of  $\gamma$ -ray intensities feeding ( $I_{\text{in}}$ ) and depopulating ( $I_{\text{out}}$ ) each energy level.

$$I_j = I_{\text{in}} - I_{\text{out}}, \quad (4.3)$$

where the intensities are determined from the number  $N$  of observed gamma rays as well as the absolute efficiency of SeGA at the given energy  $E_\gamma$  (i.e.  $I_{\text{in,out}} = N_{\text{in,out}}/\epsilon(E_\gamma)$ ). Due to the statistical nature of the sampling of the incoming and outgoing intensities from a level, negative cross sections consistent with zero can be obtained in the analysis. As a negative cross section is unphysical, these small

Table 4.3:  $^{31}\text{Mg}$  states with direct feeding from the proton knockout from  $^{32}\text{Al}$ .

$E$ (keV)	$J^\pi$	$\sigma_{\text{exp}}$ (mb)	$\sigma_{\text{sp}}$ (mb)	$\sigma_{\text{sp}}C^2S$ (mb)
0.0	$1/2^+$	$0.33 \pm 0.14$		
673.2	$3/2^+$	$3.56 \pm 0.20$	12.5	10.4
1154.5		$0.53 \pm 0.13$		
2014.7	$5/2^+$	$4.27 \pm 0.24$	12.0	8.6
(2787.2)?	$7/2^+$	unobserved	11.7	5.9

negative cross sections were set to be exactly zero. The remaining partial cross sections to excited states were normalized such that their sum was consistent with  $\sigma_{\text{ex}}$  determined by all the assigned gamma ray transitions where  $\sigma_0$  is held constant. Predominately, the knockout reaction directly fed states at 673 keV and at 2015 keV. All states fed directly and their partial cross sections are shown in Table 4.3 with the corresponding theoretical calculation of Sec. 5.1.

Unplaced transitions listed in Table 4.2 can modify  $I_j$  when placed. However the intensity of each unplaced transition is fairly small; the most intense (1968 keV) of these unassigned gamma rays has a maximum contribution of  $0.54 \pm 0.16$  mb to a given state. Also, the unplaced transitions do not likely feed or decay from the same excited state. Fragmentation of the feeding intensities suggests that a sizable modification to any single partial cross section in Table 4.3 is unlikely, though possible. If all unplaced transitions feed or decay from the same excited state, this corresponds to a maximum correction of 2.1 mb which is not quoted in the uncertainties of Table 4.3. The tentatively placed decays from the 2015 keV state were included in the partial cross section and could account for an additional 1.1 mb adjustment to the partial cross section to that state. Future work with greater sensitivity is needed to clarify the placement of these transitions. Next generation gamma-ray detector arrays, such as GRETINA [68], with a higher coincidence efficiency would address this situation.

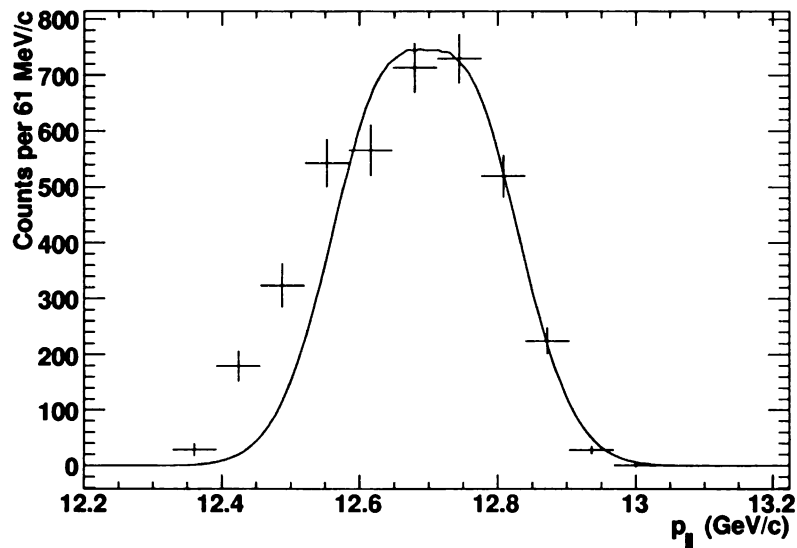


Figure 4.9: (Points) The measured momentum distribution of the  $^{31}\text{Mg}$  residues coincident with the 623 keV  $\gamma$ -ray. (Line) Predicted momentum distribution based on the knockout of a  $d_{5/2}$  proton from  $^{32}\text{Al}$  to the  $3/2^+$  673 keV state in  $^{31}\text{Mg}$  including the effects from the loss of energy in the target as well as the incoming momentum width.

#### 4.2.4 Momentum distribution of residues

Coincident with the gamma rays detected by SeGA, the momentum distribution of the outgoing particles measured at the S800 focal plane contains information about the dynamics of the reaction. The distribution associated with the residues coincident with the 623 keV gamma ray is shown in Fig. 4.9. The contribution from the  $\gamma$ -ray background was subtracted based on the momentum distribution coincident with gamma rays from the spectra above and below the transition of interest. The momentum distribution coincident with the 623 keV gamma ray is representative of all momentum distributions observed for the  $^{31}\text{Mg}$  residues after the knockout reaction, including those coincident with other gamma rays as well as those events where no gamma ray was detected. The shape of the distribution is an indicator of the orbital angular momentum of the removed nucleon and is consistent with

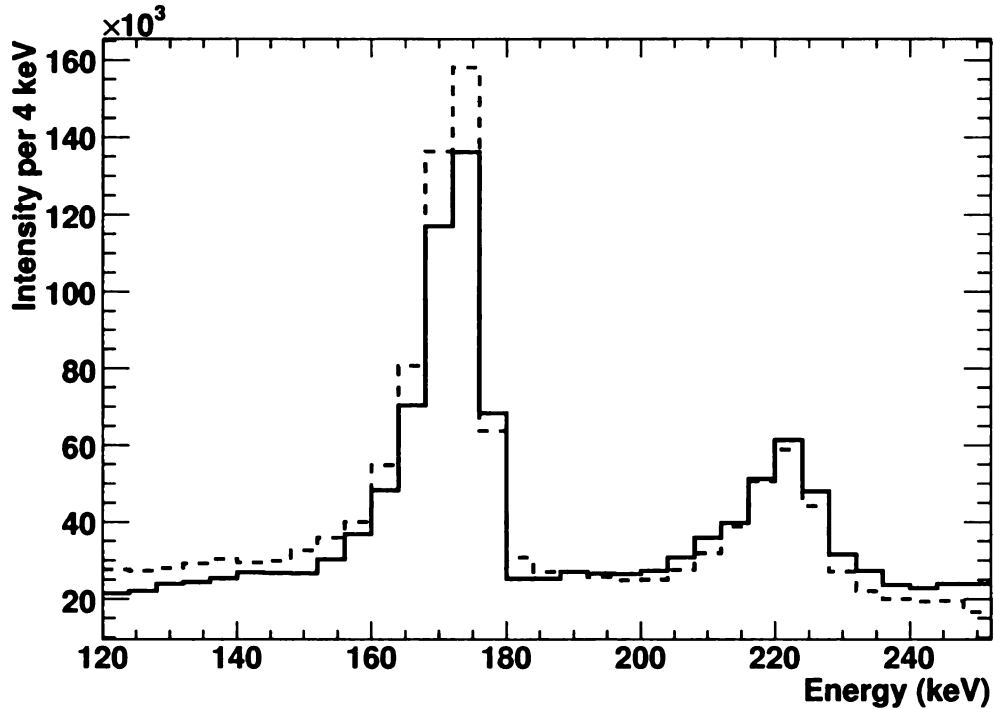


Figure 4.10: Relative intensity of gamma rays emitted from the 221 keV state in  $^{31}\text{Mg}$  as determined by efficiency calibrations (Sec. 3.2) and proper Doppler reconstruction for the forward (dashed) and backward (solid) rings in SeGA.

the knockout of an  $\ell = 2$  proton for the populated states according to the reaction calculations discussed in Subsection 5.1.1.

#### 4.2.5 Angular distribution of gamma rays

In the examination of the decay from the excited states, evidence also exists for the presence of spin alignment along the outgoing direction of the knockout reaction residues (i.e. along the beam axis). In particular, the ratio of gamma rays detected in the forward and backward rings is substantially different for the two transitions which deexcite the 221 keV state as displayed in Fig. 4.10. The difference in the ratio between the transition to the ground state versus the transition to the 50 keV state is greater than  $4\sigma$ . The angular distribution formula can be expanded in terms of



Legendre polynomials (see Eq. A.1). Since there is a noticeable difference in angular distribution, spin alignment must exist in the 221 keV state. From the alignment condition,  $w(m) = w(-m)$ , a preference in the direction of  $\gamma$ -ray emission limits the spin of the initial 221 keV state to  $J \geq 3/2$ . However, previous lifetime measurements [65] and Weisskopf estimates of the electromagnetic transition rates [1] conclude that these are two pure dipole transitions. Given the known ground state spin of  $1/2^+$  [22] and the selection rules for electromagnetic transitions (Eq. 2.2), the spin of the 221 keV state must be either  $1/2$  or  $3/2$ . Combined with the requirements of spin alignment  $B_\lambda \neq 0$ , the 221 keV state must have a spin of  $3/2$ . Furthermore, since the spin alignment of the initial state must be the same for both the 171 keV and 221 keV transitions, any difference in their angular distributions must be attributed to differences in the final state. Particularly for pure dipole transitions,  $A_2 < 0$  for unstretched transitions ( $\Delta J = 0$ ) and  $A_2 > 0$  for stretched transitions ( $\Delta J = \pm 1$ ) where  $A_2$  depends only on the properties of the gamma-ray transition (see Appendix A). This results in a sizable difference in the angular distribution for transitions with different  $\Delta J$ , similar to that observed in the 171 and 221 keV gamma rays. This suggests that the 50 keV state should be an unstretched dipole transition with  $J_f = 3/2$ . This is also supported by the evidence that the 50 keV transition is known to be a dipole transition based on similar lifetime arguments [65].

While there are ample statistics for the angular distribution analysis for these low-lying transitions, the evidence may be affected by the long lifetime of the 221 keV state. Another case was examined which was free from such effects. Though the statistics are not as favorable, the 623 keV transition does not suffer from these issues which obfuscate the interpretation of the transitions from the 221 keV state. The 623 keV  $\gamma$ -ray decays from the 673 keV state which has a short lifetime. The intensity can also be accurately obtained in the spectral fit due to a low background and absence of contamination from the Compton edge of other  $^{31}\text{Mg}$  gamma rays. Figure 4.11

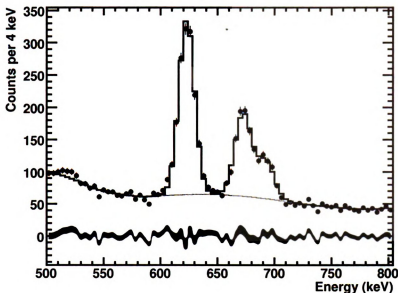


Figure 4.11: Automatic fitting using ROOT of gamma-ray peaks in the 600 keV region, including determination of the background (thin line) as well as the residue between the experimental data (points) and the fit (thick line).

shows the quality of the automatic fitting procedure. In addition, the 673 keV state is directly fed in the knockout reaction making it more amenable to reaction calculations as well as preventing effects from spin dealignment as discussed in App. A. The examination of the evolution of the spin alignment related to the outgoing momentum provides a test of the reaction mechanism. The angular distribution coefficient  $a_2$  was extracted from the experimental data over a range of cuts in the longitudinal momentum, as shown in Fig. 4.12. Given a prolate spin alignment in the most central part of the momentum distribution, the data agree with a transition with  $\Delta J = 0$  including the dipole limitation imposed by the Weisskopf estimates. This suggests an assignment of  $J = 3/2$  to the 673 keV state. It is important to note here that the reaction mechanism produces a strongly prolate spin alignment,  $B_\lambda > 0$ , in the center of the momentum distribution which decreases as more of the central momentum is included. If this qualitatively holds, then the slope alone of the evolution of the

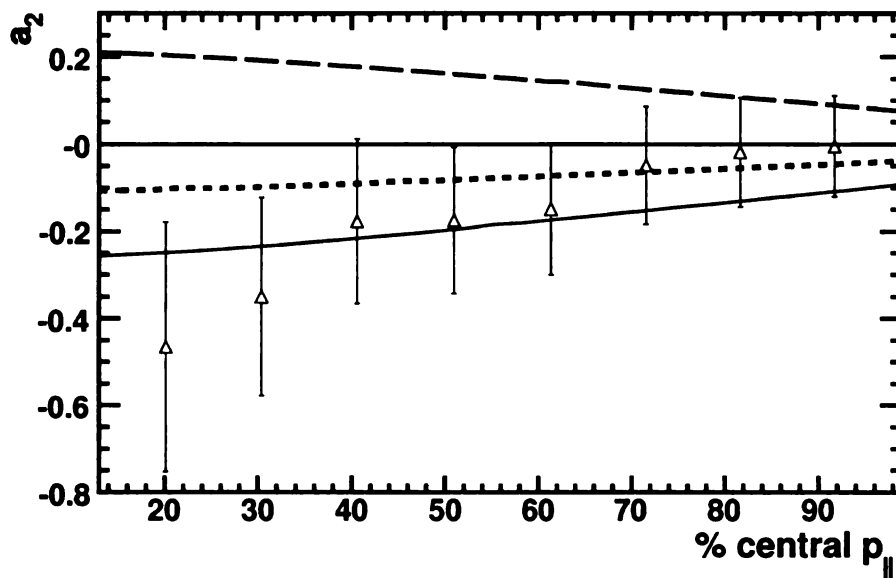


Figure 4.12: The angular distribution coefficient  $a_2$  determined from the experimental data (triangles) and theory (solid line) as a function of increasingly broader longitudinal momentum gates for a  $3/2 \rightarrow 3/2$  623 keV pure dipole transition. Theoretical curves are also shown for a  $5/2 \rightarrow 3/2$  transition for a dipole (long dashed) and quadrupole (short dashed) multipolarity. The abscissa describes the percentage of central momentum counts included.

angular distribution is a good indicator of the sign of the  $a_2$  coefficient. This is independent of any systematic errors introduced by uncertainties in the determination of the efficiency of the gamma-ray detectors. Considering the whole momentum distribution includes this uncertainty in normalization of the detectors but also allows the use of all the statistics which makes it the most conclusive for some of the gamma-ray transitions. The  $\gamma$ -ray angular distribution coefficients extracted from the whole residue momentum distribution are quoted in Table 4.2.

#### 4.2.6 Linear polarization of gamma rays

With the presence of spin alignment in the system, gamma rays emitted from  $^{31}\text{Mg}$  should exhibit linear polarization. Determination of the sign of the linear polarization alone allows for the measurement of the parity of the excited states provided the par-

ity of one of the states in the transition is known. The sensitivity of SeGA to linear polarization was discussed in Sec. 3.3 by examining the Compton scattering within the crystal. Polarization measurements benefit from greater consistency in terms of the normalization of the scattering data since the normalization for a ring is only dependent on the scattering of unpolarized gamma rays in that ring whereas effects in both rings must be accounted for in angular distribution measurements. In addition, only a relative normalization of the two directions of scattering is needed. Furthermore, angular distribution measurements depend on an accurate determination of the efficiency of the array which varies rapidly with energy (see Fig. 3.2) as compared to the Compton scattering asymmetry which varies more slowly (Fig. 3.8). In addition, the relativistic effects play less of a dramatic role. The polarization of gamma rays is also maximized at a center-of-mass angle of  $90^\circ$  which is close to the backward ring in the classic setup of SeGA which has  $\theta_{\text{c.m.}} = 114^\circ$  for residues moving at  $\beta = 0.4$ . Differences in the Compton scattering (Fig. 4.13) were clearly observed for the peaks in the 600 keV energy region. Note that the  $\gamma$ -ray background in the figure shows no presence of polarization which adds credibility to the in-beam normalization of the scattering. However, due to the low statistics, the linear polarization measurements have significant uncertainty as shown in Table 4.2.

#### 4.2.7 Spin and parity assignments

With an accurate measurement of the linear polarization and angular distribution coefficients, the multipolarities of the transitions can be determined. The linear polarizations were extracted using the known 18% relative sensitivity of SeGA discussed in Section 3.3. To reduce the statistical uncertainty, the whole momentum distribution of the reaction products was considered. Combining the  $\gamma$ -ray multipolarity assignment with the selection rules for knockout reactions (Eq. 1.3) allows for firm spin and parity assignments. In particular, the selection rules imply the states fed

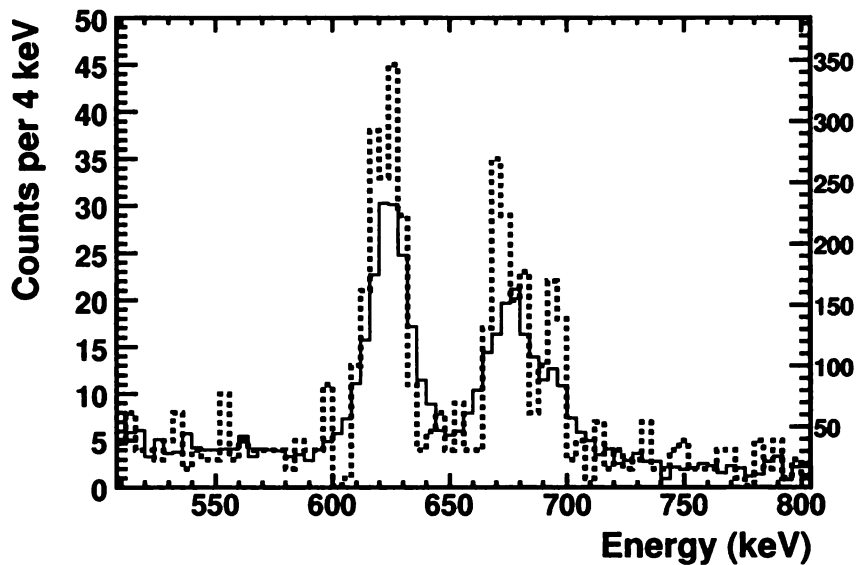


Figure 4.13: The Compton scattering of gamma rays relative to the reaction plane defined by the beam axis and the gamma ray propagation direction in  $^{31}\text{Mg}$ : (dashed, left axis) scattering perpendicular to the plane, (solid, right axis) scattering parallel to the plane, normalized (by a factor of 0.13) to the intrinsic scattering from a gamma ray emitted by a  $^{152}\text{Eu}$  source with no spin alignment

directly in the production of  $^{31}\text{Mg}$  have a positive parity.

The results discussed in Subsec. 4.2.5 allowed the spin assignment of the 673 keV state. Two of the gamma ray transitions from the 673 keV state have sufficient statistics to determine  $\gamma$ -ray Compton scattering asymmetries and angular distributions as shown in Table 4.2. When including the full statistics across the momentum distribution, the 673 keV gamma ray shows evidence of angular distribution. For this case, the linear polarization measurement is not consistent with zero and suggests a mixed  $M1$  transition with  $\Delta J = 1$  or a stretched quadrupole transition to the ground state; the comparison to theoretical values is shown in Fig. 4.14 for a final spin of  $1/2^+$ . While the measurement is closer to the values for a stretched quadrupole, the momentum-constrained angular distribution analysis for the 623 keV transition (see Fig. 4.12) indicates an initial spin of  $3/2$  for this state. This supports the assignment of a mixed  $M1/E2$   $\Delta J = 1$  transition with  $\delta \approx 2$  for the 673 keV gamma ray. The

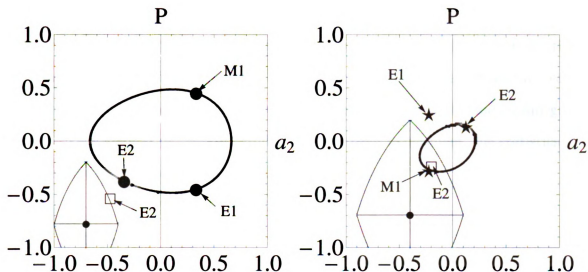


Figure 4.14: (left) Experimental angular distribution coefficient and polarization for 673 keV gamma ray with  $1\sigma$  confidence interval compared to theoretical values of a decay to a final spin state of  $1/2^+$  from an initial 66% prolate-aligned spin state of  $3/2$  (circles) or  $5/2$  (squares) for different multipolarities as indicated - lines of  $M1/E2$  mixing are also shown; (right) Measurements for 693 keV gamma ray compared to values for a final spin state of  $7/2^-$  postulated by Mach et al. [65] assuming a 33% initial prolate alignment for an initial spin of  $11/2$  (squares) or  $7/2$  (stars).

information for the 623 keV gamma ray is less conclusive when including the entire residue momentum distribution. However, the negative scattering asymmetry (and thus negative polarization) is more in agreement with a  $M1$  transition suggesting  $J^\pi = 3/2^{(+)}$  for the final 50 keV state with the parity remaining tentative due to the substantial uncertainty in the Compton scattering asymmetry.

The linear polarizations and angular distribution coefficients for the 693 keV transition also deviate sizably from zero despite the significant uncertainties. Only the final spins which have expected values near the experimental data are shown for clarity in the exclusionary plot in Fig. 4.14 (see Appendix A for further information) which compares the measured angular distribution coefficients and linear polarizations to those calculated by transitions of different multipolarities and initial spins. Here, the spin and parity for the final state are not certain but have been previously postulated to be  $7/2^-$  [65]. Generally,  $a_2 < 0$  and  $P < 0$  agrees best however with unstretched

$M1$  or stretched  $E2$  transitions; however, an  $E1$  multipolarity is not too far removed from the experimental confidence interval. The normalization of the angular distribution can add considerable systematic uncertainty to this analysis. Truly, one would want to investigate the evolution of the linear polarization with momentum gates similar to the angular momentum study. In the current experiment, the statistics are too prohibitive to do such an analysis.

## 4.3 $^{33}\text{Mg}$

### 4.3.1 Beam characteristics and particle ID

In the case of the  $^{33}\text{Mg}$  study, the production cross section for the  $^{34}\text{Al}$  secondary beam was significantly reduced. To achieve enough statistics within the allocated time, a thicker secondary reaction target of 2 mm beryllium ( $370 \text{ mg/cm}^2$ ) was used at the target position of the S800. The purity of the secondary beam was also significantly lower (50%) with the major contaminants being  $^{35}\text{Si}$  and  $^{37}\text{P}$ . Similar to the study of  $^{31}\text{Mg}$ , the components of the secondary beam can be cleanly selected based on the time of flight from the A1900 to the object box of the S800 as displayed in Fig. 4.15. The reaction products shown in Fig. 4.16 were then identified in the S800 using the same method as in Section 4.2 where the unreacted secondary beam was removed in the S800 by  $B\rho$  selection. Two normalization runs with the unreacted beam transmitted to the focal plane of the S800 were taken with a lower intensity to establish the properties of the incoming beam.

For the  $^{33}\text{Mg}$  residues, the mean mid-target velocity was found to be  $\beta = 0.402 \pm 0.002$ . At this velocity, the forward ring of SeGA lies at a center-of-mass angle of  $54^\circ$  limiting the effects of angular distribution given  $P_2(\cos \theta_{\text{c.m.}}) = 0.011(3)$ . With a thicker target than for the  $^{31}\text{Mg}$  experiment, the energy resolution of the gamma ray detection was worse. An in-beam gamma-ray resolution of 2.7% relative to the  $\gamma$ -ray

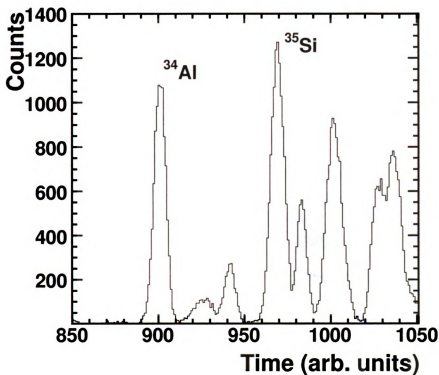


Figure 4.15: Incoming  $^{34}\text{Al}$  particles identified by the time of flight from the extended focal plane of the A1900 magnetic separator to the object box of the S800 spectrograph.

energy was obtained for both rings. Corrections based on the S800 information allow a better determination of the velocity and improve the relative resolution to 2.5% in the backward ring. The improved resolution in the backward ring was used for determination of all energies of the gamma ray transitions observed in the experiment.

### 4.3.2 Level scheme

The gamma ray spectrum resulting from the knockout reaction to  $^{33}\text{Mg}$  is displayed in Fig. 4.17. Information about the transitions observed in the experiment is summarized in Table 4.4. None of the transitions show any indication of lifetime effects as discussed in Subsec. 4.2.2 which suggests these states are all short-lived so the decay



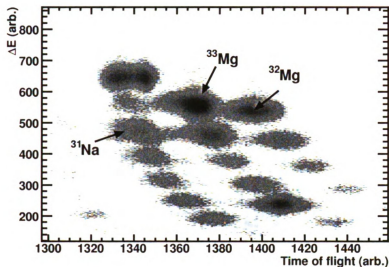


Figure 4.16: Outgoing residues for the reactions of an incoming  $^{34}\text{Al}$  beam identified by the S800 spectrophograph based on the energy loss in the ion chamber and their time of flight with selected isotopes of interest labeled.

Table 4.4: Gamma-ray transitions observed for  $^{33}\text{Mg}$  in the current experiment with their intensities normalized to the 483 keV transition as well as their angular distribution coefficients and Compton scattering asymmetries.

$E_i$ (keV)	$E_f$ (keV)	$E_\gamma$	$I_\gamma$	$a_2$	$A$
484.1	0.0	483.1 (9)	100	0.36 (17)	-0.03 (8)
705.0	484.1	219.7 (10)	1.8 (7)		
	0.0	704.4 (14)	6.7 (12)	0.9 (8)	
780.4	484.1	297.3 (6)	57 (3)	0.33 (21)	-0.08 (9)
	0.0	780.7 (18)	15.2 (19)		
1242.4	484.1	758.1 (16)	12.6 (18)	0.1 (7)	
	0.0	1240 (3)	16 (3)		
unplaced		1069.6 (24)	5.0 (17)		
		1523 (4)	12 (3)		
		1856 (5)	7 (4)		
		1929 (6)	7 (3)		

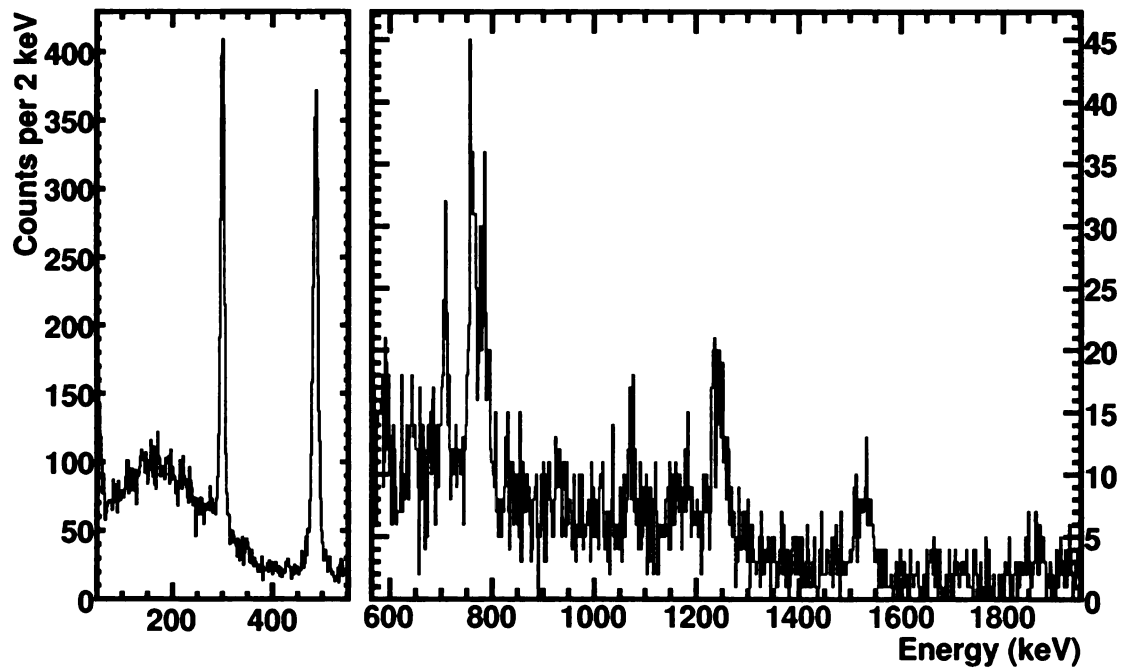
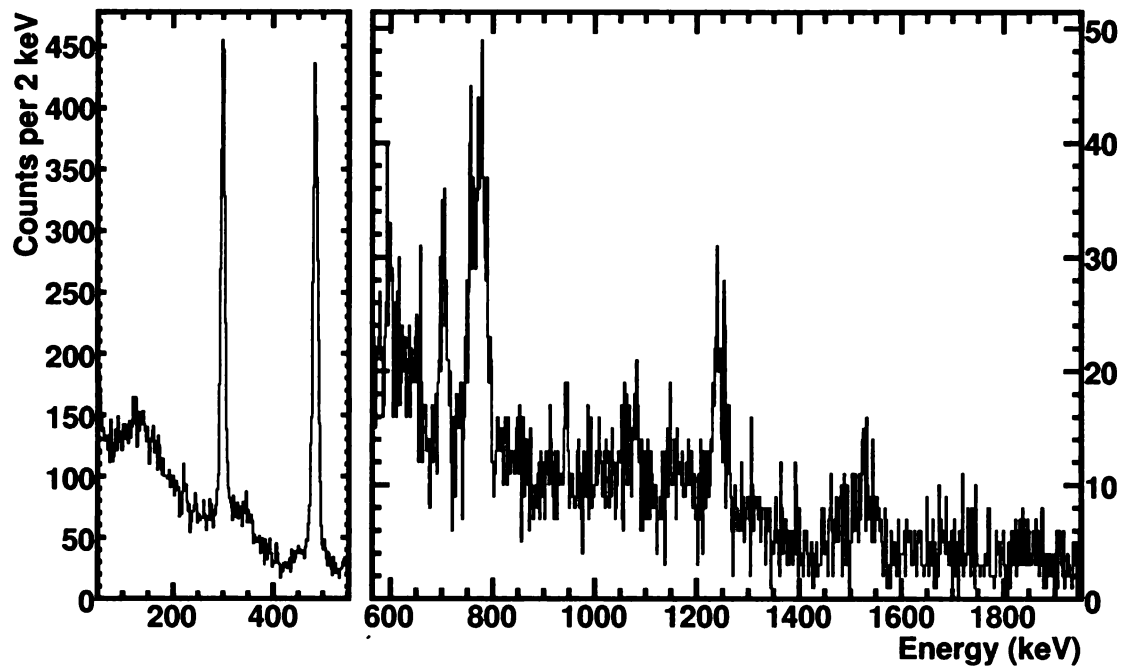


Figure 4.17: Gamma-ray spectrum of  $^{33}\text{Mg}$  detected in SeGA for the forward (top) and backward (bottom) rings.

occurs near the target ( $\tau \lesssim 10$  ps). None of the levels established in previous experiments have any information about their lifetimes. The energies of these transitions in general agree with those observed in an earlier  $\beta$ -decay experiment [69] as well as other recent measurements [70, 71]. The  $\gamma$ -ray branching ratios from the 1242.4 keV state also agree, within the uncertainties, with those in the  $\beta$ -decay experiment.

The decays from the 705 keV state warrant additional discussion. The weak 219.7 keV transition could only be clearly observed when summing the spectra from both rings of SeGA. Motivated by the previous branching ratio from the  $\beta$ -decay experiment [69] and the number of counts observed for the 704 keV gamma ray, the expected counts in the two rings would be  $192 \pm 22$  counts assuming isotropic angular distribution. On top of the large background ( $S/N \approx 0.1$ ), a small peak is indeed observed at the right energy with a total of  $135 \pm 54$  counts which is within the margin of error of the previous experiment. However, the  $\beta$ -decay experiment also tentatively placed a 546.2 keV transition emanating from the 705.0 keV state. This had a significantly higher intensity observed following  $\beta$ -decay, and while approximately 300 counts would be expected in the  $^{33}\text{Mg}$  gamma-ray spectrum, no evidence of a peak is observed. A gamma ray consistent with the energy of 546.2 keV was also seen in the proton inelastic scattering experiment [71] without observing the other gamma rays associated with the 705 keV state in the  $\beta$ -decay experiment. This suggests this gamma ray does not originate from the 705 keV state, but most likely feeds the ground state directly from an unassigned level of 546 keV.

A new level could also be placed in the  $^{33}\text{Mg}$  level scheme based on the information provided by  $\gamma$ - $\gamma$  coincidences. The 483 keV decay was seen to be in clear coincidence with the 297 keV gamma ray (see Fig. 4.18) allowing for the placement of a level at 780 keV. The coincidence is also seen taking the reverse gate on the 483 keV transition. Incidentally, a 780.7 keV gamma ray is also observed for the first time in the current experiment. This transition has an energy which agrees with the decay

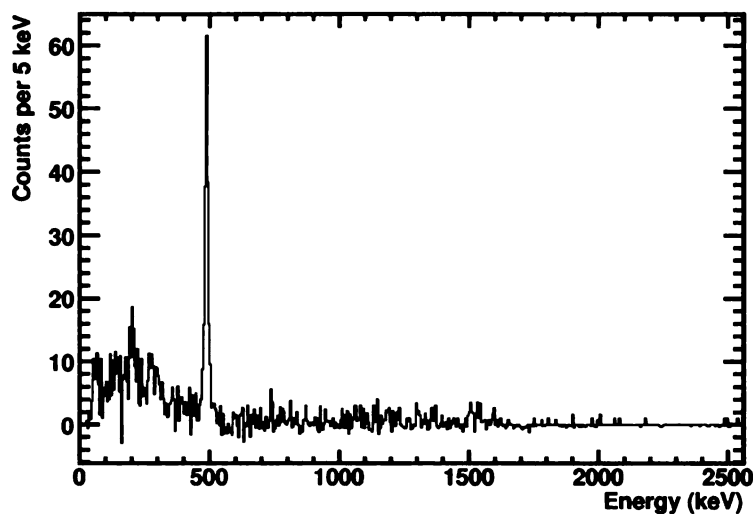


Figure 4.18: Background-subtracted gamma-ray spectrum coincident with the 297 keV gamma-ray transition in  $^{33}\text{Mg}$ .

of the newly placed state to the ground state and has been placed in the level scheme accordingly. Theoretically, the established 758 keV decay from the 1242 keV state that feeds the 484 keV state should also be observed in the  $\gamma$ - $\gamma$  coincidence measurement. However, given the intensity in the singles spectra and the efficiency of the detectors, the coincidence spectrum would only show approximately 23 counts for the 758 keV coincident decay which is within the background fluctuations. With the additional information from the  $\gamma$ - $\gamma$  coincidences, the level scheme observed in this experiment can be found in Fig. 4.19.

Several other transitions seen in the proton knockout experiment remain unplaced in the level scheme. These five transitions mentioned in Table 4.4 have a total intensity which is 31(6)% of the 483 keV gamma ray transition. These are mostly high energy transitions which cannot be placed due to the lack of coincidence information.

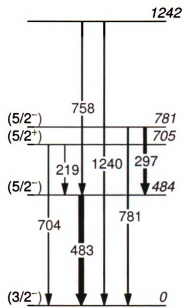


Figure 4.19:  $^{33}\text{Mg}$  level scheme observed in the present experiment with suggested spin and parity assignments.

### 4.3.3 Inclusive and partial cross sections

The inclusive cross section was determined similar to the method established in Section 4.2. However, during the experiment, a sudden change in the transmission was observed following a retuning of the primary beam. The normalization of the incoming beam was based on the rate on the object scintillator in order to provide the greatest consistency in the extracted cross section on a run-by-run basis. The normalization factor was determined from two different runs with the S800  $B\rho$  tuned to select the unreacted incoming  $^{34}\text{Al}$  particles in the spectrograph. Fluctuations in this normalization add an additional 5% systematic uncertainty in the cross section measurement. The width of the momentum distribution once again led to a cut in the angular acceptance in the dispersive direction (Fig. 4.20) which accounts for another 2.5% of systematic uncertainty to the cross section measurements.

The inclusive proton knockout cross section was determined to be 4.32 millibarns. For the  $^{33}\text{Mg}$  case, the additional systematic uncertainties from the normalization and acceptance determination are much more significant. The cross section on a run-

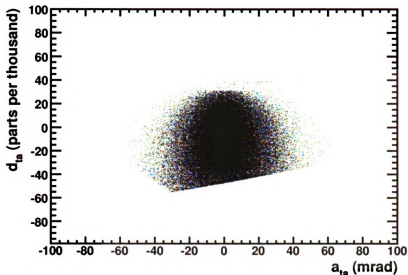


Figure 4.20: Focal plane measurements of  $a_{ta}$  and  $d_{ta}$  showing the acceptance cut for low momentum  $^{33}\text{Mg}$  residues from an incoming  $^{34}\text{Al}$  beam.

by-run basis is shown in Fig. 4.21. The variation in the cross-section on a run-by-run basis adds a systematic uncertainty of 2.5% giving a total systematic uncertainty in the measurement of 0.4 millibarns. Here, the inclusive cross section is significantly decreased in comparison to the  $^{31}\text{Mg}$  case. As the neutron separation threshold in  $^{33}\text{Mg}$  is 0.2 MeV lower, there is an increased possibility that highly-excited states populated in the reaction decay rapidly by neutron emission and thus do not make it to the focal plane of the S800 which could account for the decreased cross section.

The cross sections to the excited states were extracted from the particle-gamma information along with the balancing of the gamma-ray intensities. The partial cross section to the ground state was determined by subtracting all the excited state partial cross sections from the inclusive cross section. The results are summarized in Table 4.5. There was some feeding to all the states which emitted gamma rays though most of the feeding populated the newly discovered 780.4 keV state. Unassigned gamma transitions amount to a maximal adjustment to the cross section of

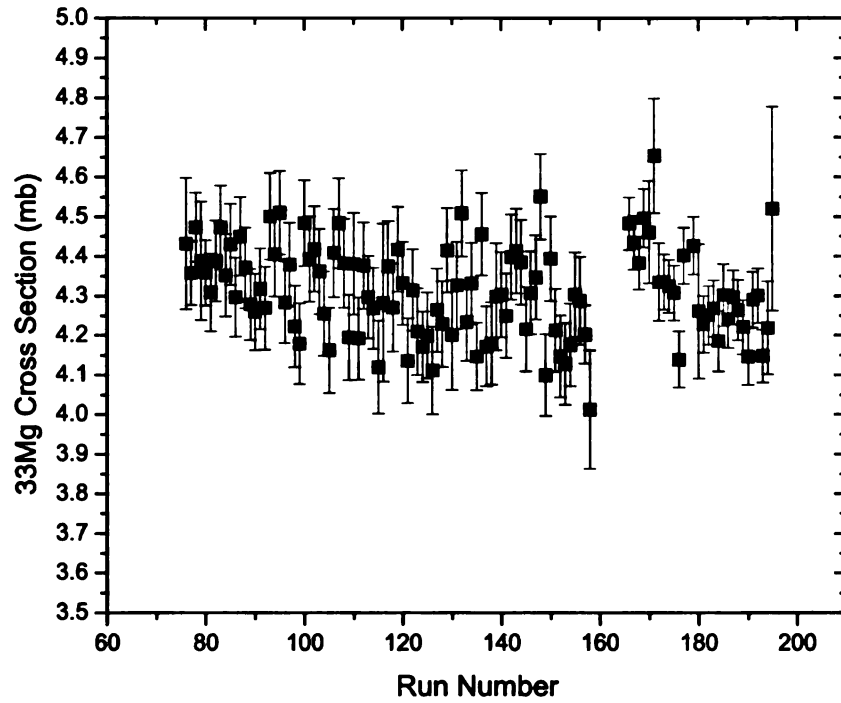


Figure 4.21: Inclusive cross section of  $^{34}\text{Al} \rightarrow ^{33}\text{Mg}$  calculated on a run-by-run basis chronologically from left to right.

Table 4.5:  $^{33}\text{Mg}$  states with direct feeding from the proton knockout from  $^{34}\text{Al}$ .

$E$ (keV)	$J^\pi$	$\sigma_{\text{exp}}$ (mb)
0.0	$(3/2^+)$	$0.42 \pm 0.16$
484.1	$(3/2^-)$	$0.79 \pm 0.13$
705.0	$(5/2^+)$	$0.24 \pm 0.04$
780.4	$(3/2^-)$	$2.05 \pm 0.12$
1242.4	$(1/2^+)$	$0.81 \pm 0.09$

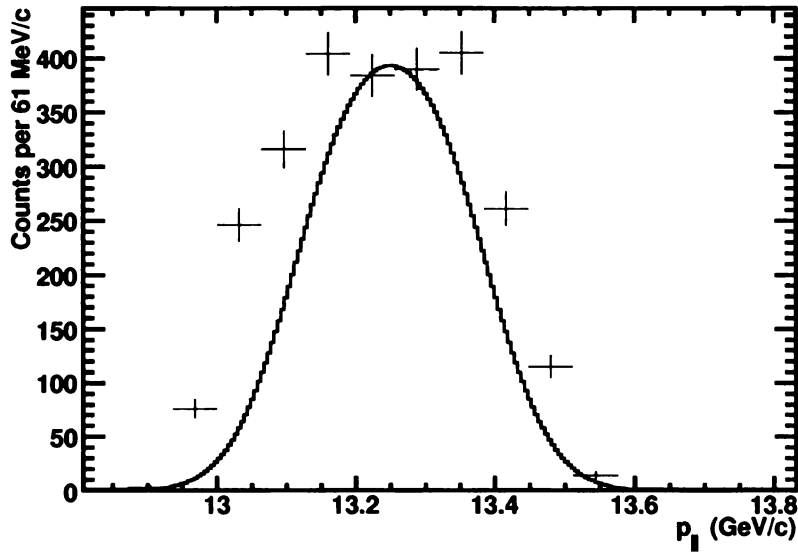


Figure 4.22: (Points) The measured momentum distribution coincident with the 297 keV gamma ray, (Line) Predicted momentum distribution based on the removal of a  $d_{5/2}$  proton from  $^{34}\text{Al}$  including effects from the loss of energy in the target as well as the incoming momentum spread.

$0.88 \pm 0.17$  mb. Though this likely will not highly impact any individual partial cross section, it removes certainty of the feeding of the weakly populated ground state and 705.0 keV state in the knockout reaction.

#### 4.3.4 Momentum distribution of residues

The longitudinal momentum distribution associated with the gamma rays is similar to the situation in  $^{31}\text{Mg}$ , which suggests the removal of a  $\ell = 2$  proton from the incoming  $^{34}\text{Al}$  isotopes. However the experimental width is broadened due to the increased thickness of the target and cannot be well-described with typical input parameters for the reaction. The background-subtracted momentum distribution coincident with the observed 297 keV gamma ray is shown in Fig. 4.22. This is once again representative of the momentum distributions of all the states directly fed in the reaction, including the particle singles detected in the S800.



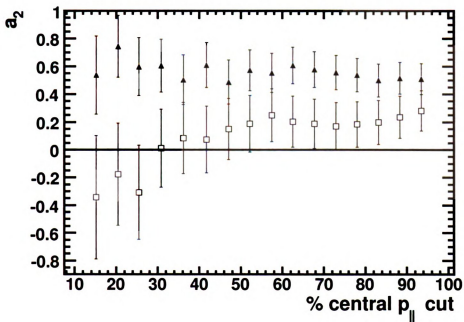


Figure 4.23: Angular distribution coefficients extracted for  $^{33}\text{Mg}$  as a function of increasingly broader momentum gates for the 297 keV transition (squares) and the 483 keV transition (triangles).

### 4.3.5 Angular distribution of gamma rays

The gamma rays emitted by the  $^{33}\text{Mg}$  nuclei were also examined for the presence of angular distribution. Only the two most intense gamma rays in the spectrum had enough statistics to perform a significant analysis. Both of the peaks were clearly separated enough to perform a systematic investigation based on the gating of the longitudinal momentum distribution shown in Fig. 4.23. Only the 297 keV shows strong evidence of variation in the momentum-constrained  $\gamma$ -ray angular distribution. It is important to reiterate here that based on a prolate alignment in the center of the momentum distribution the slope as a function of broader momentum gates is directly related to the sign and magnitude of the angular distribution coefficient. This is independent of any systematic error in the absolute normalization.

As the calculated angular distribution coefficient for the 483 keV transition is

relatively flat as more momentum is included, it is suggestive of an  $a_2$  coefficient close to zero. However, the coefficient extracted from the gamma-ray intensity and efficiency is significantly positive ( $2\sigma$ ) which should also appear in the slope of the momentum-gated angular distribution analysis. This provides an estimate of the systematic uncertainty in the absolute normalization of the gamma-ray intensities in the rings of roughly 10% based on the deviation from  $a_2 \approx 0$  and the difference between the  $P_2(\cos\theta_{\text{c.m.}})$  in the two rings. The uncertainty in the absolute normalization is avoided in the momentum-constrained analysis.

For the low-energy 297 keV gamma ray with no evidence of lifetime effects, the Weisskopf estimates limit the transition to dipole multipolarity. The evolution of this transition clearly resembles the trend observed for the 623 keV transition in  $^{31}\text{Mg}$  discussed in Section 4.2. The trend combined with the Weisskopf estimates suggests that the 297 keV gamma ray corresponds to an unstretched dipole transition. On the other hand, the 483 keV transition shows no evidence of a variation in the momentum-gated angular distribution. This suggests one of two possibilities. The nuclear spin alignment has been reduced by the gamma rays which feed the state from above, or the properties of the transition are such that no spin alignment can be observed. Since the feeding states likely have significant prolate alignment in the most central part of the momentum distribution, some degree of alignment is expected as well in the fed 484 keV state. This seems to make the second interpretation more likely where the lack of angular distribution is a property of the  $\gamma$ -ray transition. This means either the 484 keV state could be a  $J = 1/2$  with no possible spin alignment or the transition is such that there is only a small effect in the angular distribution such as a  $\Delta J = 1$  strongly mixed transition originating from a high spin (e.g.  $7/2 \rightarrow 5/2$ ). Here the significant deformation of the  $^{33}\text{Mg}$  nucleus [70, 71] can create a sizable enhancement of the  $E2$  transition probability which would explain this strong mixing for the low lying 484 keV transition.

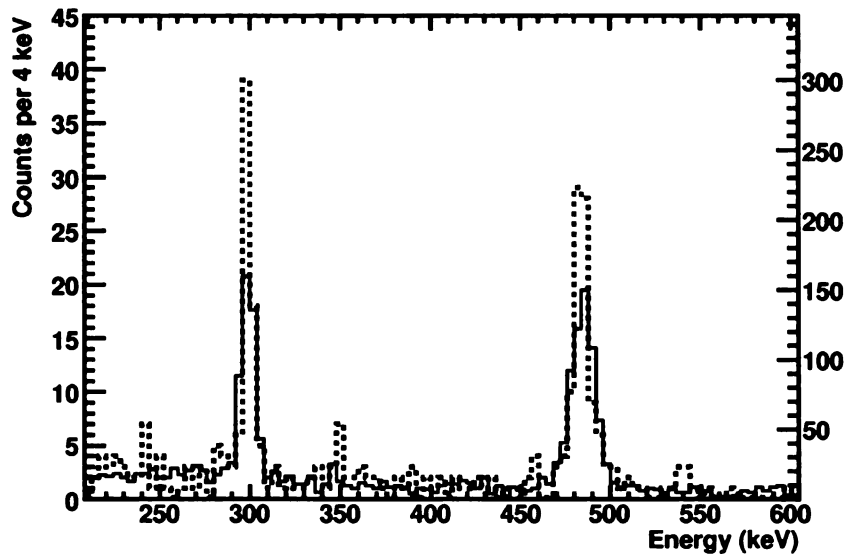


Figure 4.24: The Compton scattering of gamma rays relative to the reaction plane defined by the beam axis and the gamma ray propagation direction in  $^{33}\text{Mg}$ : (dashed, left axis) scattering perpendicular to the plane, (solid, right axis) scattering parallel to the plane, normalized (by a factor of 0.13) to the intrinsic scattering from a gamma ray emitted by a  $^{152}\text{Eu}$  source with no spin alignment.

### 4.3.6 Linear polarization of gamma rays

Information was also extracted about the linear polarization of the gamma rays emitted by the reaction residues. Similar to the case of  $^{31}\text{Mg}$ , the backward ring lies at  $\theta_{\text{c.m.}} = 114^\circ$  given the measured velocity of the particles. This is close to where the linear polarization is maximized, however with the reduced statistics the evidence is less clear in the  $^{33}\text{Mg}$  case. Only the two low energy transitions have enough statistics to be sensitive to the  $\gamma$ -ray linear polarization. The resultant spectrum is shown in Fig. 4.24. Though the asymmetry looks quite large, this is reduced by the increased widths of the gamma rays which scatter parallel to the plane. The decreased resolution of the parallel scattering  $\gamma$ -rays is likely attributed to small inaccuracies in the Doppler reconstruction. Perpendicular scattering is completely confined within a longitudinal slice of the SeGA detector (see Fig. 3.7) which constrains the angle more

precisely than in the parallel scattering case. With the low statistics, the uncertainties in the measured asymmetries are sizable. For the 297 keV and 483 keV transitions, the Compton scattering asymmetries are  $A = -0.08 \pm 0.09$  and  $A = -0.03 \pm 0.08$  respectively. With significantly more statistics, one could investigate the evolution of the asymmetries as a function of longitudinal momentum; however that remains intractable here.

### 4.3.7 Spin and parity assignments

Through analysis of the linear polarization and angular distribution of the gamma rays, the transition multipolarities can be established. With sufficient precision, some knowledge about the mixing ratios as well as the actual final and initial spins can be determined. However, often experiments must rely on prior knowledge about either the initial or final spin and parity of the transition. In  $^{33}\text{Mg}$  unfortunately, there are no firm previous assignments of spin and parity. Furthermore, the range of spins allowed to be populated by the knockout selection rules covers a wide range from  $3/2^-$  to  $13/2^-$  based on the removal of a  $d_{5/2}$  proton from the ground state of  $^{34}\text{Al}$  with known  $J^\pi = 4^-$  [72]. Given the uncertainties in the current experiment, strong support cannot be given to a given multipolarity; however, the polarization and angular distribution measurements suggest certain multipolarities, while excluding others.

For the 484 keV transition which feeds the ground state, the positive  $a_2$  coefficient supports a stretched dipole transition. The polarization measurement does not constrain this to electric or magnetic character, but would suggest a strong  $M1/E2$  mixing as shown in Fig. 4.25 which compares the measured angular distribution coefficients and linear polarization with predictions for different multipolarities and initial spins. Previous Coulomb excitation work [70] indeed suggests that this transition has a considerable  $E2$  contribution with an initial spin of  $7/2^+$  assuming a ground

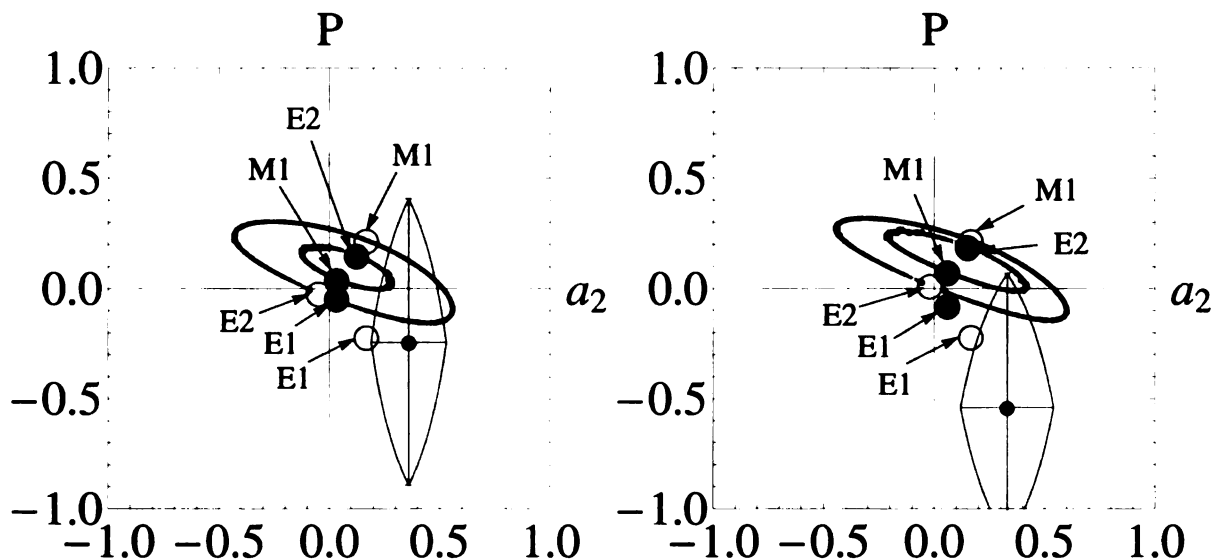


Figure 4.25: (left) Experimental angular distribution coefficient and polarization for 484 keV gamma ray with error bars and  $1\sigma$  confidence interval compared to theoretical values of a decay to a final spin state of  $5/2^+$  (from Pritychenko et al. [70]) from an initial 33% prolate-aligned spin state of  $7/2$  (empty circles) or  $3/2$  (filled circles) for different multiplicities as indicated – lines of  $M1/E2$  mixing are also shown; (right) Measurements for 297 keV gamma ray compared to values for a final spin state of  $7/2^+$  assuming a 66% initial prolate alignment for an initial spin of  $9/2$  (empty circles) or  $5/2$  (circles).

state spin of  $5/2^+$ . The current experiment agrees with this interpretation, especially if one considers the possibility of a systematic uncertainty in the angular distribution measurement discussed in Subsec. 4.3.5. As the measurement only determines the spin and parity differences, this could also be interpreted as a  $7/2^- \rightarrow 5/2^-$  transition which agrees better with the presence of direct feeding in the knockout reaction shown in Table 4.5. However, a possibility that this partial cross section could be affected by feeding from unplaced and/or unresolved transitions cannot be excluded.

For the 297 keV transition from the strongly populated 780 keV state, the data once again suggest a  $\Delta J = 1$  transition which likely also has considerable mixing. Here the final spin state has been assumed to have  $J^\pi = 7/2^{(-)}$ . From the calculated points in Fig. 4.25, this seems to support a similar situation as the 484 keV gamma ray; here with initial  $J^\pi = 9/2^-$  favored slightly. Here, the knockout selection rules

clearly constrain the parity of the initial state. The spin assignment depends on the assignment of the lower-lying states, but a  $\Delta J = 1$  transition remains the most likely. Further discussion regarding other possibilities considered in previous work will follow in Sec. 5.2.

# Chapter 5

## Commentary

### 5.1 $^{31}\text{Mg}$

#### 5.1.1 Calculation of momentum distribution

The momentum distribution of the fragments following the proton removal shown in Figure 4.9 can be described well in a three-body reaction model based on the eikonal and sudden approximation [27, 73]. For the standard shell ordering for the protons in the incoming  $^{32}\text{Al}$  nucleus with  $Z = 13$ , the valence proton would occupy the  $d_{5/2}$  orbital, which is consistent with the momentum distribution of the residues observed in the reactions. The calculations considered this valence  $d_{5/2}$  proton outside of the  $J^\pi$  core of the  $^{31}\text{Mg}$  residue in its excited state. The core and the valence proton were coupled to the known ground state spin of  $^{32}\text{Al}$  [14],  $J^\pi = 1^+$ . It is important to note that the incoming  $^{32}\text{Al}$  fragments were assumed to impinge upon the secondary fragmentation target while they were in their ground state. An isomeric state with  $J^\pi = 4^+$  does exist in  $^{32}\text{Al}$  with a half-life of 200 ns, which was previously observed by Robinson et al. [74]. However, the population of this isomer from the fragmentation reaction would have decayed considerably over the  $\sim 80$  m flight path which corresponds to roughly four half-lives. Based on the selection rules (Eq. 1.3),

direct removal of a  $d_{5/2}$  proton from the  $^{32}\text{Al}$  nucleus would populate states with  $J^\pi = (3/2, 5/2, 7/2)^+$  in the residues. Population of the  $1/2^+$  ground state is small since it could only proceed by the removal of a deeply bound  $s_{1/2}$  proton or a  $d_{3/2}$  proton which is an unfilled orbital with standard shell ordering.

### 5.1.2 Structure of observed excited states

The structure of the excited states was interpreted in the framework of several theoretical models. A calculation using the USD shell model interaction was used for the analysis of the  $0p1h$  states. As the USD interaction is truncated above the  $N = 20$  shell gap, its application to states with excitations across the shell gap is intractable. Since the ground state is dominated by a  $2p3h$  configuration, the relative excitation energies of the  $0p1h$  states cannot be addressed by the calculations. To assess the intruder states, the technique using AMD+GCM [67] employing the Gogny D1S interaction [75] was used. The excitation energies in both calculations were shifted to reproduce the observed energy of the  $0p1h$   $3/2_1^+$  in Fig. 4.5. As the current work predominately populated these  $0p1h$  states, the theoretical predictions related to these states are the main subject of the commentary. In the two calculations, there is a significant difference in the energy spacing of the  $0p1h$  states due to the different approach used in determining the effective interaction.

The levels at 673 keV and 2015 keV present themselves as candidates for the  $0p1h$   $3/2^+$  and  $5/2^+$  states respectively, which are the two lowest  $0p1h$  states predicted theoretically [67]. The reaction preferentially populates these states since  $^{32}\text{Al}$  has been established to lie outside of the “island of inversion”. The ground state of  $^{32}\text{Al}$  is well described by the  $sd$ -shell with its  $1^+$  ground state having a dominant configuration of  $\pi d_{5/2}^{-1} \otimes \nu d_{3/2}^{-1}$  [76]. The theoretical partial cross sections to individual states shown in Table 4.3 have spectroscopic factors calculated from the  $sd$ -shell wavefunctions for the ground state of  $^{32}\text{Al}$  and for the excited  $0p1h$  states  $^{31}\text{Mg}$



labelled in Fig. 4.5. The spectroscopic factors for the  $0p1h$  ground state in  $^{32}\text{Al}$  to any states in  $^{31}\text{Mg}$  with population in the  $fp$ -shell is considered to be zero. The inclusive cross section of 8.7(5) mb has a reduction of spectroscopic strength of  $R_s = 0.46(2)$  which agrees well with previous trends for removal of a deeply-bound nucleon [77] characterized by the difference between proton and neutron separation energies in  $^{32}\text{Al}$ ,  $\Delta S = 11$  MeV [78]. If the tentatively placed  $\gamma$ -ray transitions discussed in Chapter 4 are disregarded, this would reduce the partial cross section to the 2015 keV state from 4.27 to 3.33 mb. This would agree better with the theoretical relative cross sections assuming a fixed reduction of spectroscopic strength.

The cross section to the expected  $0p1h$   $7/2^+$  state is calculated to be  $\sigma_{\text{sp}}C^2S = 5.9$  mb. While the 2015 keV state could be attributed to this  $7/2^+$  state, the data argue strongly against it. With a reduction factor consistent with that of the inclusive cross section, the expected experimental cross section would be  $\sigma_{\text{sp}}C^2SR_s = 2.7$  mb which is significantly lower than the observed partial cross section. Furthermore, this would leave no evidence for the  $5/2^+$  state which both calculations predict to lie lower in energy and which has a higher expected cross section from the reaction calculations. The 2015 keV state also predominately decays to a state which has  $J_\pi = 3/2^{(-)}$  with the parity taken from the level ordering of Kimura et al. [67] which seems to agree with previous experiments [65, 66]. The multipolarity of the  $\gamma$ -ray transition from the 2015 keV state would then be significantly hindered based on the selection rules for a  $J^\pi = 7/2^+$  assignment. The Weisskopf estimate for a  $7/2^+ \rightarrow 3/2^-$   $M2$  transition would be 170 ps which would exhibit lifetime effects similar to that seen in the lineshape for the 221 keV state which has a 133 ps half-life. Even considering some enhancement of the  $M2$  transition using the recommended upper limit for the transition rate of 3 Weisskopf units [41], the spectral lineshape would still be affected by the lifetime. These three factors argue against a  $J = 7/2$  assignment for the 2015 keV state and support the interpretation of this state as the  $J = 5/2$  single-hole state.

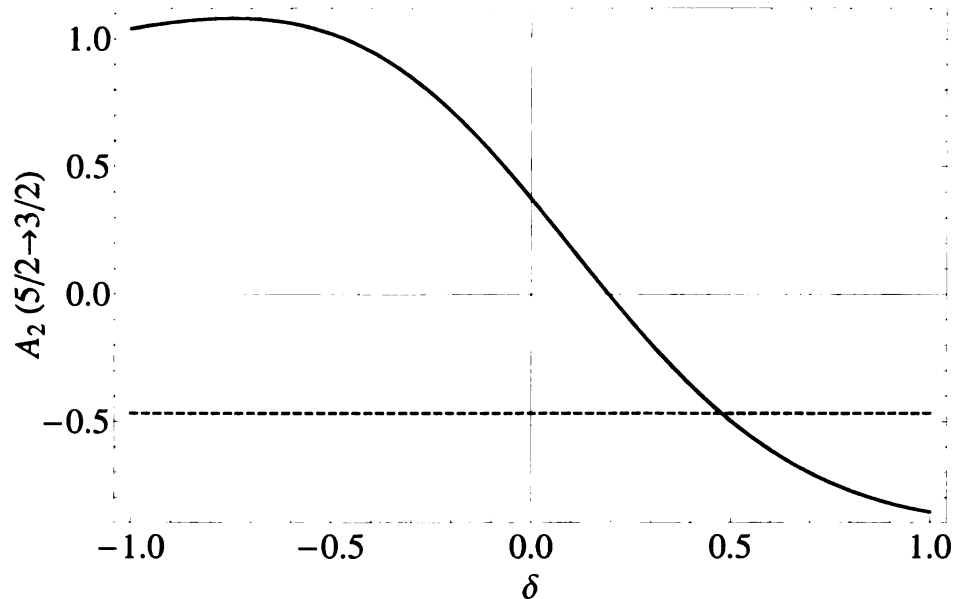


Figure 5.1: (solid) The effect of quadrupole mixing on the angular distribution coefficient  $A_2$  for a  $5/2 \rightarrow 3/2$   $M1/E2$  transition; (dashed) The angular distribution coefficient for an unmixed  $7/2 \rightarrow 3/2$   $E2$  transition.

Angular distribution data would corroborate this assignment, but the experiment was not sensitive enough due to possible quadrupole mixing in the transition (see Fig. 5.1). Mixing ratios as small as  $\delta \sim 0.2$  render sizable effects on the angular distribution as illustrated in Fig. 5.1. With the 2015 keV assigned the  $J = 5/2^+$  single-hole state, this leaves no firm observation of the  $0p1h$   $7/2^+$  state. The USD calculation predicts the  $0p1h$   $7/2^+$  state to lie 2.11 MeV above the  $3/2^+$   $0p1h$  state. This would place it at an excitation energy 2.78 MeV which would lie above the measured neutron separation energy of 2.38 MeV [78]. This explains the non-observance of the  $7/2^+$  as it would decay by neutron emission, supporting the energy spacing between  $0p1h$  states predicted by the USD interaction. However, unplaced  $\gamma$ -ray transitions could have a significant intensity to suggest decay from a higher lying unassigned  $7/2^+$  state. Placing these transitions in the level scheme would clarify the situation.

The USD calculations are incapable of producing information about the states with intruder-like configurations. The other excited states were thus interpreted in

the framework of the AMD+GCM calculations [67]. Information from previous experiments [23, 65, 66, 79, 80] also provide an important insight into the nature of these states. In particular, the neutron-knockout experiment [23] populated the  $3/2^-$  and  $7/2^-$  states located at 221 and 481 keV respectively. These are labeled as  $1p2h$  states in the AMD+GCM calculation which agrees well with the removal of a  $fp$ -shell neutron from the known  $2p2h$  ground state of  $^{32}\text{Mg}$ . These  $1p2h$  states are populated in the present experiment through the decay of the  $0p1h$  states with no excitations across the shell gap. The other populated states in Fig. 4.5 are most likely higher lying states in the  $2p3h$  rotational band based on the level ordering in the AMD+GCM calculation. There is no clear evidence for the population of the low-lying state ( $J^\pi = 3/2_2^-$ ) of the highly deformed  $3p4h$  rotational band which has a calculated deformation parameter  $\beta \sim 0.6$  [67]. This suggests that the 1155 keV state is more likely to correspond to the  $7/2^+$  state in the  $2p3h$  rotational band.

### 5.1.3 Spin alignment calculation and angular distribution

The nuclear spin alignment along the beam axis was compared to calculations using the reaction theory discussed in Sec. 1.4. Following the knockout reaction, the partial cross section to each individual  $^{31}\text{Mg}$  magnetic substate  $m$  was calculated with the component of the total angular momentum along the beam axis  $J_z = m$ . The population of the substates was compared across the entire range of the longitudinal momentum. Incoming  $^{32}\text{Al}$  fragments were assumed to have no initial spin alignment. A previous experiment with fragmentation showed no sizable alignment in the residual nucleus  $^{12}\text{B}$  after many nucleons were removed from the  $^{22}\text{Ne}$  projectile [81]. In the fragmentation reaction which produced  $^{32}\text{Al}$ , 16 nucleons were stripped off; this leaves little expectation for a non-zero initial spin alignment in the projectile. Furthermore, any spin alignment that would have been produced would have had time to relax during the time of flight to the secondary fragmentation target.

Alignment of the residues was calculated following the proton knockout reaction of the incoming  $^{32}\text{Al}$  fragments on a secondary reaction target which preferentially populated certain magnetic substates in  $^{31}\text{Mg}$ . The relative population of the magnetic substates defined the spin alignment according to Eq. A.3. Based on this alignment, the angular distribution of gamma rays relative to the alignment direction was calculated. The predicted  $\gamma$ -ray angular distribution for the 623 keV transition is consistent with the data from the experiment, as displayed in Fig. 4.12, with regards to a range of longitudinal momentum cuts. Since the gamma ray is emitted promptly (on the order of picoseconds) after the reaction, effects which dealign the spins are calculated to be negligible. In addition, higher orders of alignment were calculated to be negligible in the reaction, i.e.  $B_4 \ll B_2$ . The spin alignment was also calculated for the higher-lying  $0p1h$  states predicted by the shell model. This includes the  $5/2^+$  state at 2015 keV which has a significant feeding in the reaction. For different spin states in the  $^{31}\text{Mg}$  nucleus, the theory predicts a comparable amount of spin alignment  $B_\lambda$  in the residue. At the peak of the momentum distribution,  $B_2 \approx 0.5$  is predicted. The angular distribution effect is significantly reduced to  $B_2 \approx 0.2$  when considering the whole momentum distribution. This amount of alignment is sufficient to determine spins and parities accurately from the resulting  $\gamma$ -ray angular distribution and linear polarization, especially if an experimental setup that is more optimized for the task is utilized.

## 5.2 $^{33}\text{Mg}$

### 5.2.1 Calculation of the momentum distribution

The momentum distribution was calculated in a similar manner as in  $^{31}\text{Mg}$ . The comparison to the measured experimental values is shown in Fig. 4.22. The width of the distribution was somewhat underpredicted using typical input parameters for the

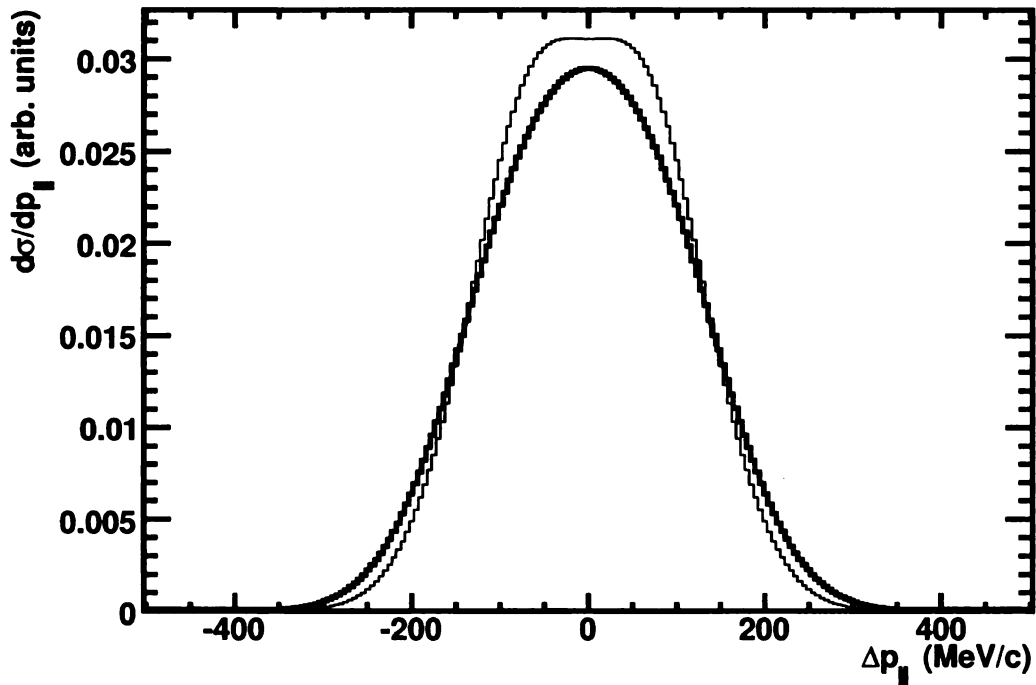


Figure 5.2: The theoretical momentum distribution of  $^{33}\text{Mg}$  after the knockout reaction relative to the central momentum before (thin) and after (thick) the convolution of experimental effects.

calculation. The calculation was convoluted with the effects from the energy loss in the target and the momentum spread of the incoming beam. Due to the thicker target, the experimental effects modified the distribution as shown in Fig. 5.2. However, the effect of the target remained small compared to the momentum spread introduced by the knockout reaction.

### 5.2.2 Structure of populated states

The discussion of the structure of populated states in the present experiment relies on the interpretation of previous experiments. In particular, the spin assignment of the ground state in  $^{33}\text{Mg}$  is a subject of significant debate. Also, the extent of the island of inversion and its behavior has undergone substantial revision since it was

originally postulated and observed.

The ground state spin and parity assignment in  $^{33}\text{Mg}$  has been previously probed using several different techniques. Beta-decay experiments [69] provided the first information about the configuration of the ground state. This experimental interpretation is dependent on the information about the parent's ground state, which has been assumed based on systematics of Na isotopes. For the ground state of  $^{33}\text{Na}$ , the spin is determined by the odd unpaired  $d_{5/2}$  proton which occupies the Nilsson orbital with  $\Omega^\pi = 3/2^+$  for prolate deformations using typical values of the nuclear potential [82]. For the  $\beta$ -decay experiment, the possibility of a  $5/2^+$  ground state spin was also considered based on the proximity of energy levels using shell-model calculations [83] with a reduction of the gap between the  $1f_{7/2}$  and  $2p_{3/2}$  neutron orbitals [84] resulting in a  $0p0h$  ground state in  $^{33}\text{Na}$ . The  $\beta$  decay was seen to have sizable feeding of  $20\pm 10\%$  to the  $^{33}\text{Mg}$  ground state suggesting a Gamow-Teller allowed transition where a  $d_{3/2}$  neutron decays into a  $d_{5/2}$  proton populating positive-parity  $1p1h$  states in  $^{33}\text{Mg}$  with spins from  $1/2$  to  $7/2$ . The associated shell-model calculations favor a  $3/2^+$  ground state for  $^{33}\text{Mg}$ . Meanwhile, a Coulomb excitation experiment [70] suggested that the 484 keV transition had  $E2$  character with  $\Delta J = 1$ . When considering the observed feeding in the  $\beta$ -decay experiment, the ground state spin had to be considered to be  $5/2^+$  to explain the experimental data which was later corroborated by a proton inelastic scattering measurement [71]. However, a recent measurement [21] instead suggests that the ground state of  $^{33}\text{Mg}$  is dominated by a  $2p2h$  configuration with  $J^\pi = 3/2^-$  bringing into question the interpretation of the previous results. Further discussion follows the assumption that this recent measurement is accurate.

The interpretation of the states populated by the current knockout study is affected by the more complicated structure of the incoming  $^{34}\text{Al}$  isotope which lies on the border of the island of inversion. To reproduce the ground state spin and parity

of  $4^-$  measured using  $\beta$ -NMR [72], the neutrons in the ground state must have a configuration which includes excitations across the  $N = 20$  shell gap. In fact, the  $2p2h$  component of the ground state needs to have a magnitude of at least 50% for the measured magnetic moment to explain the observations. In addition, the interpretation of Himpe et al. [72] needed to reduce the single-particle energy of the  $p_{3/2}$  orbital by 500 keV to describe the magnitude of the magnetic moment. This results in significant mixing of  $\pi(sd)\nu p_{3/2}$  components in the ground state wave function.

Coming from a  $^{34}\text{Al}$  nucleus where there are three active neutron orbitals ( $d_{3/2}, f_{7/2}$ , and  $p_{3/2}$ ), the neutron configuration in the resulting  $^{33}\text{Mg}$  nucleus after the knockout also should show a complicated structure of states. In fact, it is seen in Table 4.5 that the reaction feeds a number of low-lying states, which could each have their own unique neutron configuration. However, the spin and parity are still clearly limited by the knockout selection rules (Eq. 1.3).

The most strongly populated state at 780 keV has a significant cross section beyond the maximal uncertainty based on unassigned transitions. As the  $2p2h$  configurations in  $^{33}\text{Mg}$  likely have a considerable number of low-lying states, the cross section to these states would be considerably fragmented, especially if contributions from the  $\nu p_{3/2}$  orbital are significant in the ground state of  $^{34}\text{Al}$ . This makes the 780 keV state the most likely candidate for the low-lying  $0p0h$  in  $^{33}\text{Mg}$  which has negative parity based on the knockout selection rules. To make a clear spin assignment, one must utilize the information about the states which the 780 keV state feeds through gamma-ray transitions. A prompt 780 keV transition feeds the ground state of  $^{33}\text{Mg}$  which is known to have  $J^\pi = 3/2^-$  from the  $\beta$ -NMR experiment utilizing laser spectroscopy [21]. The Weisskopf transition rate for the 780 keV  $\gamma$  ray limits the spin of the 780 keV state from  $1/2$  to  $7/2$ . Knockout selection rules reject the spin assignment of  $1/2$ . The 297 keV gamma ray to the 484 keV state is indicative of an unstretched dipole transition based on the momentum-constrained angular distri-

bution analysis in Subsec. 4.3.5. The previous Coulomb excitation work [70] requires that the 484 keV state decay by a  $\Delta J = 1$  quadrupole transition to the ground state which is consistent with the current experiment as discussed in Subsec. 4.3.7. Given the measured  $3/2^-$  ground state, this suggests that both the 484 keV and 780 keV state have  $J^\pi = 5/2^-$ . This assignment agrees with the previous experimental data excluding that from  $\beta$  decay [69]. The  $\beta$ -decay information however makes assumptions based on the spin and parity of the parent  $^{33}\text{Na}$ . No direct measurements of  $^{33}\text{Na}$  have been performed to date. Also, recent measurements suggest a larger extent of the island of inversion [24] bringing into question the assumption that the parent has a  $0p0h$  configuration as assumed in Numella et al. [69].

In a spherical shell model with regular ordering, the last neutron in  $^{33}\text{Mg}$  would fill the  $f_{7/2}$  single-particle orbital. A deformed shell model [85] tailored to reproduce the  $2p2h$   $3/2^-$  ground state of  $^{33}\text{Mg}$  shows that the unpaired valence nucleon would occupy the  $[330\ 1/2]$  Nilsson orbital for moderate deformations ( $\beta \lesssim 0.3$ ) as seen in Fig. 5.3 with  $\Omega^\pi = 1/2^-$ . There is no clear evidence of this  $1/2^-$  state based on the knockout data. This certainly cannot be attributed to the 780 keV state as this is inconsistent with the observed angular distribution of the emitted 297 keV gamma rays as discussed in Subsec. 4.3.5 as well as being forbidden by the knockout selection rules. It is suggested that the  $3/2^-$  rotational state built upon this orbital could be the lowest lying in energy due to a large negative decoupling parameter as in the  $1p2h$  band in  $^{31}\text{Mg}$  calculated by Kimura et al. [67] This presents the low-lying rotational excitations with  $J^\pi = (3/2, 5/2)^-$  as candidates for the 780 keV state. The momentum-constrained analysis for the 297 keV suggests a transition that is more likely unstretched as discussed above. This supports the assignment of  $5/2^-$  to this state assuming the final total angular momentum of  $5/2$  for the 484 keV state. The assignment of  $3/2^-$  cannot be ruled out and is consistent with the evidence in Subsec. 4.3.7. However, the magnitude and nature of the alignment in the wings of the



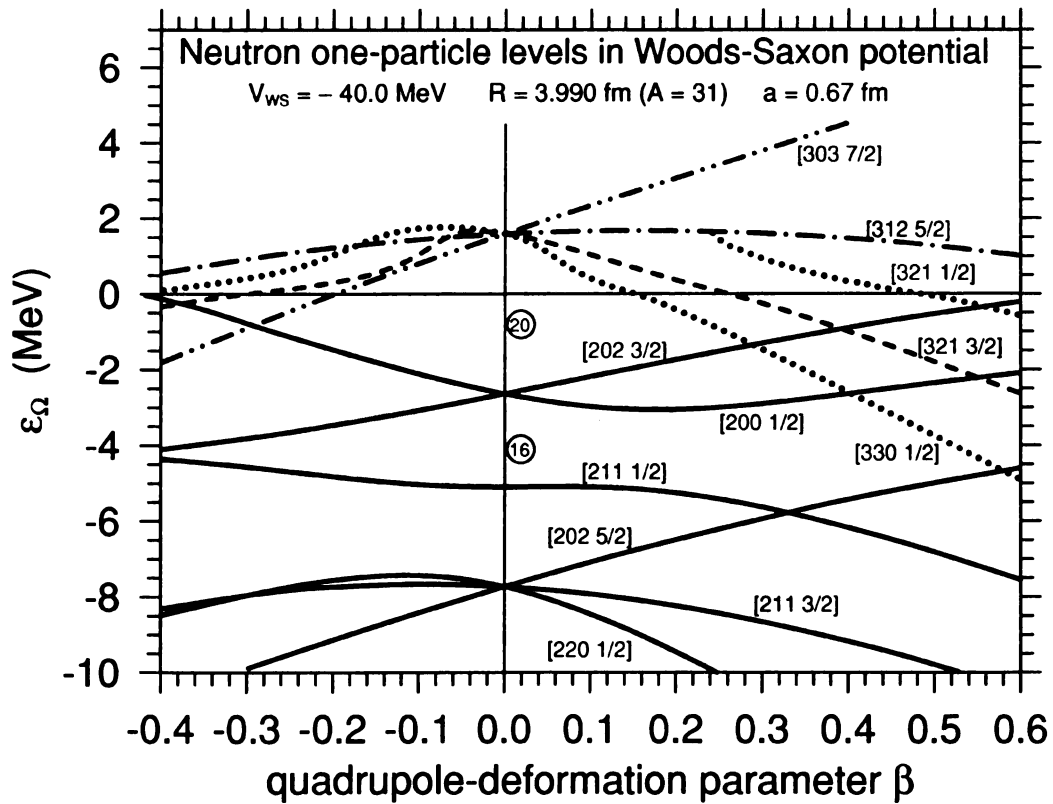


Figure 5.3: Neutron one-particle levels calculated in Hamamoto [85] with the parameters of the Woods-Saxon potential tailored to reproduce the ground state spins of  $^{31}\text{Mg}$  [22] and  $^{33}\text{Mg}$  [21].

momentum distribution is not certain, so the statements deduced without momentum gating on the residues are considerably weaker. Since the measurement using the whole distribution is also subject to normalization uncertainties, it is possible that the  $a_2$  calculation is marginally high. A smaller  $a_2$  would bring the measurement in accordance with the momentum-constrained analysis suggesting a  $\Delta J = 0$  mixed  $M1/E2$  transition.

The other states populated are likely dominated by  $2p2h$  configurations. In particular, since the ground state and 484 keV state both show signs of direct feeding, they have a negative parity. This agrees with the interpretation of Yordanov et al. [21]. Furthermore, the authors suggest that the 705 keV state has an opposite parity from the ground state. While the direct feeding in the current work seems to discredit this, the uncertainties which remain due to unplaced transitions surely could reduce the partial cross section to this weakly populated state. The only other state observed in the present experiment is at 1242 keV with a sizable direct feeding in the reaction which excludes the assignment based on  $\beta$ -decay of  $1/2^+$ ; however no clear alternative is present from the analysis.

# Chapter 6

## Outlook

The current work establishes the possibility of performing  $\gamma$ -ray angular distribution and linear polarization measurements with intermediate energy beams. Several opportunities present themselves to improve the quality and consistency of the current work. To perform accurate measurements, experiments need to improve the resolution and sensitivity of the experimental setup and obtain higher statistics for the gamma rays of interest.. Fruition of these goals is within the reach of next-generation  $\gamma$ -ray detector arrays such as GRETA [68] and AGATA [86, 87].

In experiments using beams at intermediate energies, these improvements require a balance between different aspects of the array's performance. For example, as detectors are placed further away from the target position, the angular resolution is improved. This allows for better Doppler correction of the energies and decreases the solid-angle attenuation factor for angular distribution and linear polarization effects. The trade-off lies in the decreased detection efficiency of the array as the detectors now cover a smaller solid angle. On the other hand, detectors could be moved closer to increase efficiency in exchange for a decrease in the energy resolution. Furthermore, due to the relativistic kinematics and angular distribution effects, the observed properties of the gamma rays in the lab reference frame depend on the angle

of emission relative to the beam axis. It is important to choose angles accordingly such that the sensitivity to properties of interest is maximized. This also must consider how the lab angles are related to the angle in the center-of-mass frame which varies with the velocity of the incoming beam. All these factors must be balanced accordingly when designing the detector setup, which is often limited by additional physical constraints.

The next generation of  $\gamma$ -ray spectroscopy will try to tackle these issues by implementing digital data acquisition for the arrays. This will allow for signal decomposition and  $\gamma$ -ray tracking in the detectors bringing about an improved interaction position resolution for the gamma ray. In turn, the detectors could have an increased energy resolution or could be brought closer to the target for an increased efficiency. While the next-generation arrays plan to implement digital acquisition, recently SeGA was outfitted with digital processing capabilities [88,89] to instrument the 18 central contact channels as well as the 576 segments, including interfacing this with the existing electronics for auxiliary detectors at NSCL.

## 6.1 Signal decomposition and gamma-ray tracking

Digital data acquisition systems record the waveforms associated with the gamma-ray detection to memory and/or disk of a computer allowing for further processing. Signal decomposition deconstructs the waveforms to determine precisely where the gamma-ray interacted within a given segment. The position determination is based on the Shockley-Ramo theorem [90] where the induced charge on the electrodes is related to the moving charges within the germanium semiconductor as a function of time. In particular, the electron-hole pairs generated when a gamma-ray interacts within the crystal induces charges on the segment where it interacts as well as neighboring segments. Here, the segment electrode which collects the drifting charges is identified as the segment where the interaction occurred, and the shape of the wave-

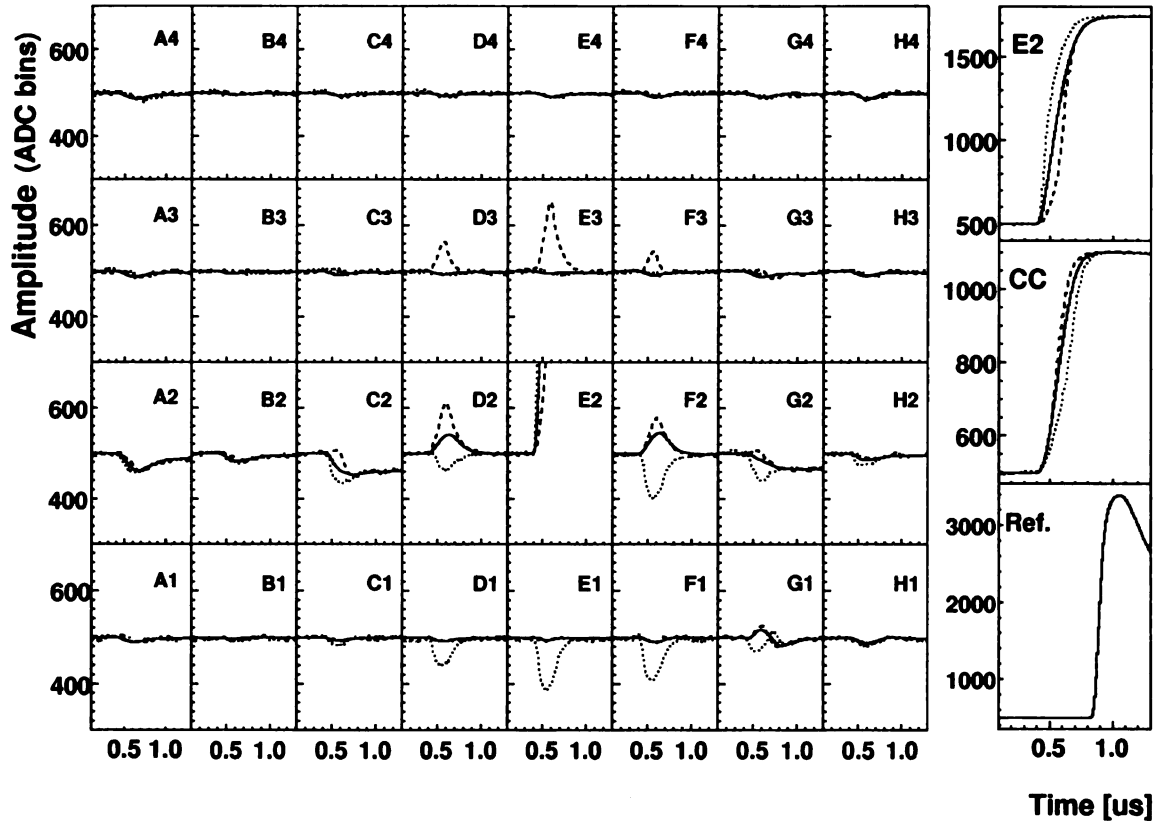


Figure 6.1: Induced signals recorded in the 32 segments and central contact of a SeGA detector for several events where a 1332 keV gamma ray from  $^{60}\text{Co}$  interacts in single segment E2 at different positions.  $\gamma$ - $\gamma$  coincidences are recorded in a CsF detector; this serves as a timing reference for the measurement [91].

forms induced in all of the segments carry information about the interaction position. The magnitude of these signals is related to the energy deposited by the gamma ray in the detector (see Fig. 6.1).

To understand how the signal changes in time, one must be able to understand the motion of the charge carriers within the crystal. This requires both an accurate determination of the electric field in the detector as well as the mobility of the charge carriers within the crystal structure. The induced signals can then be calculated using weighting potentials  $\phi_0$  which consider the solution to Maxwell's equations with boundary conditions such that only one electrode has a non-zero fixed potential.

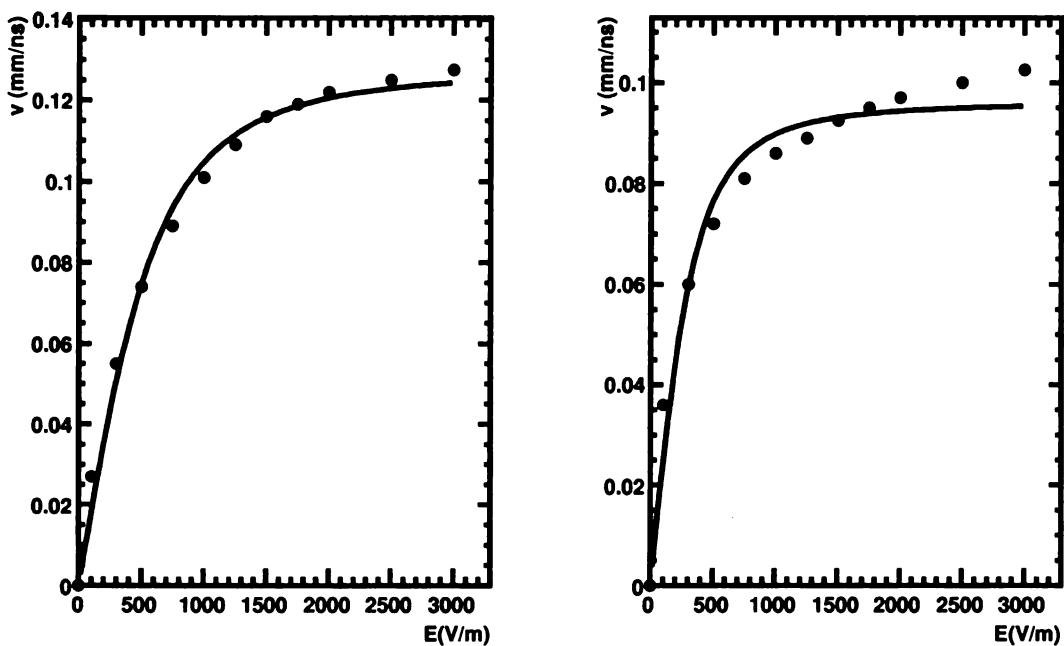


Figure 6.2: Drift velocities as a function of electric field for (left) electrons and (right) holes along the [100] axis in germanium with corresponding model calculations for a HPGGe detector [93].

The signal  $Q(t)$  induced in the electrode with a given weighting potential is then:

$$Q(t) = -q\phi_0(x(t)) \quad (6.1)$$

for a drifting charge  $q$  whose position  $x(t)$  as a function of time depends on the electric field in the device. The motion of the charge carrier depends on its mobility within the crystal which can be fundamentally different for the electrons and holes. This also depends on the orientation of the crystallographic axes. The mobility along one crystallographic axis can be related to the drift velocity for different electric fields in a relatively simple model [92] as shown in Fig. 6.2. Since this is anisotropic given the crystal structure of germanium, additional effects must be considered as discussed in further detail in Mihailescu et al. [94]. Once the motion of the charge carrier is

known, the resulting signals on the electrode for an interaction at a given position can be calculated.

After the interaction positions are well known within the detector,  $\gamma$ -ray tracking can be used to determine the ordering of these interactions. The ordering of interactions is vital because the first interaction point determines the angle in the Doppler correction formula; knowledge of this angle is the primary limit on the energy resolution for experiments with intermediate-energy beams. Combined with the second interaction point, this also determines the first scattering of the gamma ray which is intrinsically related to its linear polarization (see Subsec. 2.4.1). This tracking is generally based on the Compton scattering formula (Eq. 2.5) by comparing the scattered experimental energies of the photon to the calculated energies determined by the scattering angle. Given a chosen ordering of interactions, the tracking gives a figure-of-merit based on the deviation in energy. Especially poor figure-of-merits could be an effect of incomplete absorption in the detector and can be rejected, reducing the signal-to-noise ratio in the spectrum. In the end, the ordering of interactions with the best figure-of-merit is taken to be the true ordering; though this is not guaranteed to be a unique solution [95]. Here, information about the cross-sections of the Compton and photoelectric effect can provide further information about the most likely ordering of events. Further information is available about a number of algorithms in the literature [96–98], including methods of reconstructing gamma-ray interactions which occur across several detectors.

## 6.2 SeGA digital electronics

While digital acquisition is an integral part of future  $\gamma$ -ray detector arrays, significant improvement can be made through developing instrumentation to acquire digital data for current arrays. Such an implementation has been done with SeGA where

digital data acquisition modules were developed in collaboration with XIA LLC with the particular details of the Digital Data Acquisition System (DDAS) discussed in previous works [88, 89, 91]. The system is comprised of 39 Pixie-16 modules with 100 MHz 12-bit digitizers arranged in 4 custom compact PCI/PXI crates each with its own dedicated computer for event processing (and eventually signal decomposition). With a conservative goal of improving the position resolution by a factor of two, the energy resolution could be improved two-fold or the efficiency of the array quadrupled (subject to experimental space constraints). For intermediate-energy beam experiments, one should note that the angle of gamma-ray emission relative to the beam axis is dominantly determined by the longitudinal interaction position in a given detector. An increase by two in resolution should be feasible if one can discern if an event interacted in one longitudinal half or the other for a given event. Simple algorithms which only incorporate the integrated induced signals have been shown to generate this magnitude of improvement for a 662 keV gamma ray from a collimated  $^{137}\text{Cs}$  source [99].

One aspect that is especially important for the successful integration is the timing in the system. The waveforms acquired by DDAS should be able to be synchronized. Small constant offsets which can result from cable delays can be compensated for. To assess the constancy of this offset, tests were performed by giving DDAS a sinusoidal waveform from a high-precision signal generator. The relative phases between different channels gives information about the delay. If the frequency of the signal is well known, the  $\chi^2$  analysis to determine the phase is linearized [100] making the analysis for the  $\sim 600$  channels significantly less computationally intensive. DDAS was shown to consistently capture synchronous waveforms with jitter less than 300 ps as shown in Fig. 6.3; note that this resolution is significantly below the 10 ns time step based on the 100 MHz clock of the Pixie-16 cards. Timing between detectors in SeGA and auxiliary detectors must also be established. For in-beam runs, a fast plastic scintilla-



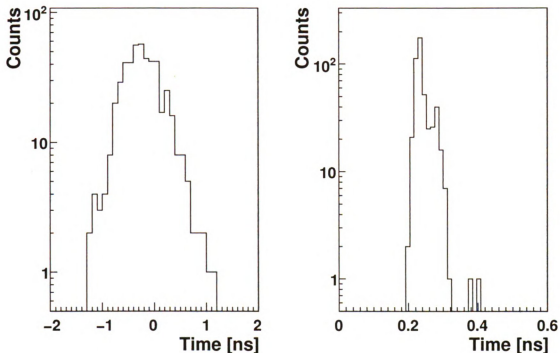


Figure 6.3: (left) The mean delay of signals for segments in SeGA and (right) the standard deviation of the delay for events in a given channel [91].

tor detects the residue and produces the reference signal. This signal has a rapid rise time and decay time which is beyond the resolution of a 100 MHz ADC. To address this, each master trigger derived from the fast scintillator also creates a pulse with similar characteristics to that from a germanium detector to use for timing in DDAS. The time is then determined on an event-by-event basis using the information about the time to cross the constant fraction amplitudes of 10% and 20% from the energy sums calculated for each event on the Pixie-16 card. This results in a 10 ns timing resolution for the 1332 keV peak emitted from a  $^{60}\text{Co}$  source in coincidence with the 1173 keV gamma rays detected in a fast CsF detector [91] as shown in Fig. 6.4.

Once the waveforms can be properly synchronized and correlated with events in external detectors, the next step is to develop a database of calculated waveforms to which experimental waveforms can be compared in order to determine the most likely

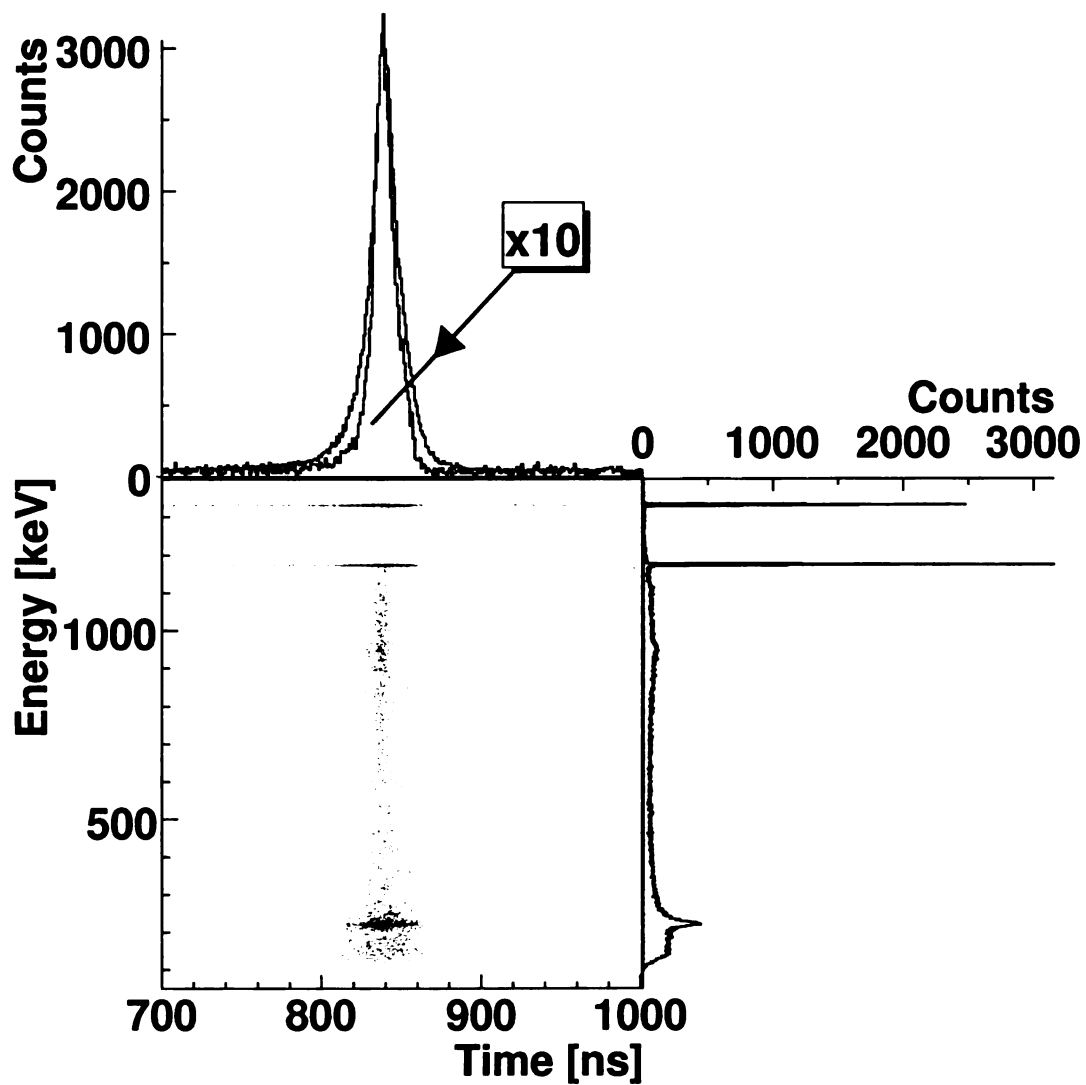


Figure 6.4: (lower left) Energy-time two-dimensional plot for a SeGA detector with coincident gamma rays in a CsF detector. (above) Time projections for all the events (shaded) as well as gated on the 1332 keV transition (clear). (right) Full energy projection [91].

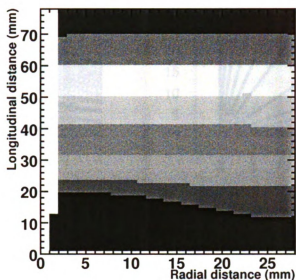


Figure 6.5: Segment division in a SeGA detector for a  $r$ - $z$  plane based on the drifting of holes to a given electrode. The longitudinal distance is measured from the “A” segment (0 mm) to the “H” segment (80 mm).

position of interaction. Algorithms designed for GRETINA were adapted to the SeGA geometry and utilized to investigate the sensitivity of the array. First, the division between segments was investigated based on the movement of the holes to a given segment electrode. The result of the calculation is shown in Fig. 6.5. The uniform 1 cm physical division of the electrodes is evident at the outermost radius as the holes drift to the nearby contact. Further away from the segment electrode though, the holes are subject to greater effects from the field. This especially is evident near the central contact which ends before the “A” segments. The fringe fields resulting from this create a much larger volume where interactions occur in what is identified as the “A” segment and decreased volume for “B” segment interactions. This change in volume should be accounted for when determining the interaction position within a segment based on the centroid of the spatial distribution. For lower energy gamma rays, this must be convoluted with the fact that gamma rays are also more likely to

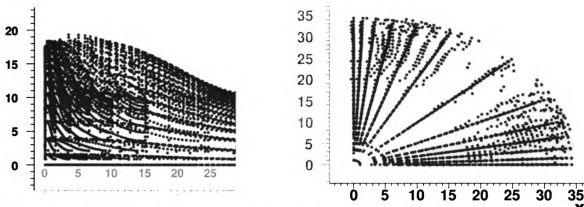


Figure 6.6: Calculated grid points for an “A” segment of a SeGA detector in the  $x$ - $z$  plane (left) and  $x$ - $y$  plane (right) which sample the segment volume to maximize the sensitivity to the changing shape of the waveform.

interact in the detector on the side closer to the source. Considering the centroid from a naïve uniform physical division clearly does not account for these effects.

The database of calculated waveforms should maximize the position sensitivity for each individual calculation point. To achieve this, an iterative technique is applied to an originally uniform cylindrical grid. In a given iteration, the grid is adapted to make the  $\chi^2$  uniform between any two neighboring grid points. The adaptive grid thus takes finer samples where the waveform changes rapidly, for example near segment boundaries and electrodes. An example grid is shown in Fig. 6.6 for an “A” segment. A given waveform can then be compared to the database waveforms with a  $\chi^2$  analysis to assign the position of interactions.

The signal calculations have been developed to a preliminary stage to demonstrate the sensitivity for SeGA detectors. To maximize the position resolution, other effects must be considered. The calculated signals need to be folded with the electronic response of the detector including the preamplifier as well as the cross talk (both differential and integral) between different electronics channels. Anisotropies in the drift velocity and charge trapping also are not accounted for in the current calculations. Source experiments to characterize the detectors of SeGA are necessary to constrain parameters such as the crystal orientation and the mobility of the charge carriers.

These topics will be addressed in future work.

### 6.3 GREYINA impact

While DDAS will allow considerable improvements of the position resolution of SeGA, the detectors are not ideally designed for sensitivity of the produced waveforms to the interaction position. Next generation arrays such as GREYINA [68] and its prototype GREYINA have incorporated this sensitivity directly into the design of the detectors, for example by minimizing cross talk between channels. The goal of the detector and electronics design was to achieve a position resolution of less than 2 mm RMS in three dimensions which has been recently demonstrated [101]. This is a five-fold improvement on the position resolution currently given by the segmentation of SeGA detectors. The possibilities with the GREYINA prototype alone are monumental, especially for experiments at fragmentation facilities. This superior position resolution will greatly enhance the sensitivity of the array to angular distribution and correlation effects.

GREYINA is proposed to cover the full  $4\pi$  solid angle with 30 detector clusters each of which house 4 HPGe detectors in a common cryostat. The GREYINA prototype under current construction will have  $1\pi$  coverage and will demonstrate all the necessary aspects of implementing the entire array. The physical design of GREYINA places the 30 clusters in five angular rings ( $32^\circ$ ,  $58^\circ$ ,  $90^\circ$ ,  $122^\circ$ , and  $148^\circ$ ) to cover the entire solid angle. GREYINA will consist of 7 clusters which will be distributed among the forward angles to maximize the sensitivity of the intended experiment. The implications for  $\gamma$ -ray angular distribution and linear polarization measurements are discussed here.

The sensitivity to these effects depend on the values of the Legendre polynomials at the center-of-mass angle for a given velocity as well as the efficiency of the detectors

Table 6.1: Relevant quantities for angular distribution measurements for GRETA angles assuming  $\beta = 0.4$ .

$\theta_{\text{lab}}$	$\theta_{\text{c.m.}}$	$P_2(\cos \theta_{\text{c.m.}})$	$P_2^{(2)}(\cos \theta_{\text{c.m.}})$	$d\Omega_{\text{c.m.}}/d\Omega_{\text{lab}}$	$E_{\text{mult}}$
$32^\circ$	$47^\circ$	0.190	1.62	1.92	1.39
$58^\circ$	$81^\circ$	-0.459	2.92	1.35	1.16
$90^\circ$	$114^\circ$	-0.260	2.52	0.84	0.92
$122^\circ$	$140^\circ$	0.383	1.23	0.57	0.76
$148^\circ$	$159^\circ$	0.803	0.39	0.47	0.68

taking into account the effects of the Lorentz boost. The relevant quantities are expressed in Table 6.1. To maximize the sensitivity to angular distribution for a measurement in two rings, the detectors should be placed to maximize the difference in  $P_2(\cos \theta_{\text{c.m.}})$ . At the same time, the efficiency should be optimized so the requisite statistics can be collected taking into account the forward boost in the solid angle for the Doppler effect as well as considering that gamma-rays emitted forward are Doppler shifted to higher energies and thus are detected with less efficiency. For angular distributions, the figure-of-merit,  $F$ , calculated from the statistical analysis is:

$$F = (P_2(x_1) - P_2(x_2)) \left( \frac{1}{\epsilon_1} + \frac{1}{\epsilon_2} \right)^{-1/2}, \quad (6.2)$$

where  $x_{1,2} = \cos \theta_{\text{c.m.},1,2}$  and  $\epsilon_{1,2}$  is the efficiency of detectors at that angle. The largest difference in  $P_2$  is clearly between the two angles for the GRETA setup in the forward hemisphere. From this alone, GRETA has at least a two-fold increase in angular distribution sensitivity compared to SeGA. This does not consider the four-fold efficiency increase, which will improve the sensitivity by another factor of two. Figure 6.7 shows the figure-of-merit for a two angle measurement with one of the angles fixed at  $32^\circ$ . This does not consider other effects which may be of experimental importance such as the energy resolution necessary to resolve the gamma transition as well as increased signal-to-noise for the forward angles. For reactions which only result in moderate spin alignment, a two-point measurement is sufficient as only  $a_2$  needs

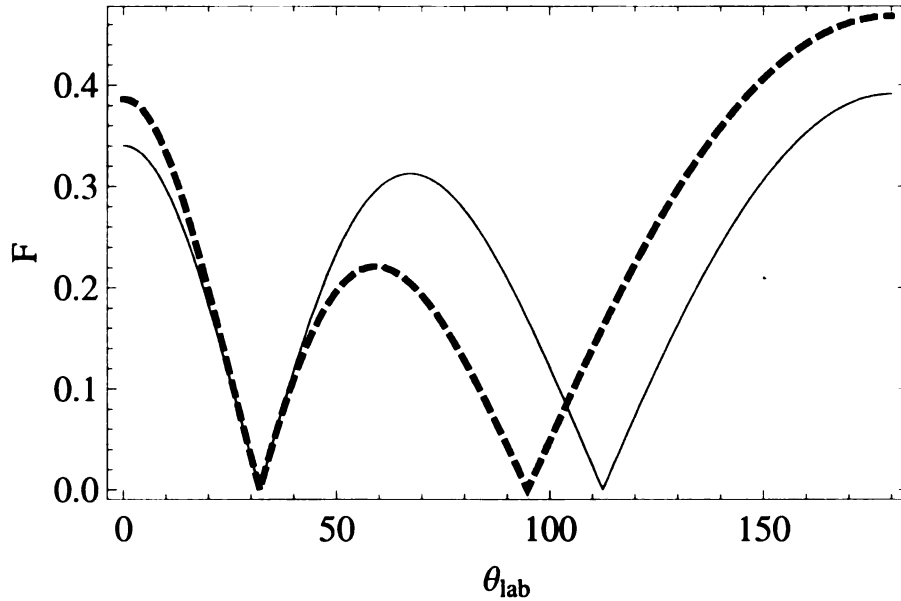


Figure 6.7: Angular distribution sensitivity for residues with  $\beta = 0.4$  (solid) and  $\beta = 0.525$  (dashed) considering placement of a second ring with the first ring fixed at  $32^\circ$ .

to be determined. Detectors should be focused in two rings to maximize the statistics and extract the most precise measurement. It is also useful to extract branching ratios for transitions in detectors which have angular distribution effects minimized. For the GRETA angles, effects from angular distribution are present in all rings for current typical intermediate beam energies. At the next generation Facility for Rare Isotope Beams (FRIB) [102] which will upgrade NSCL's capabilities, primary beam energies of 200 MeV/u will be obtainable for elements as heavy as uranium. For these energies, velocities of nuclei near  $\beta = 0.525$  will result in gamma-ray emission with minimal angular distribution effects in the  $32^\circ$  ring of GRETA while preserving significant sensitivity in other rings. At these higher beam energies, measurements at backward angles become increasingly important as shown in Fig. 6.7.

GRETINA will also significantly improve the linear polarization sensitivity. This is a result of the array geometry as well as the abilities of  $\gamma$ -ray tracking. The polarization is maximized at  $90^\circ$  in the center-of-mass frame. GRETINA's detectors

at  $58^\circ$  are quite suitable for polarization measurements. Using segment information to determine the scattering angle alone, the sensitivity of the GRETINA detectors would be comparable to SeGA (See Table 3.1). Better resolution of the scattering angle based on the better position resolution from signal decomposition increases the sensitivity by a factor of two based on simulations [96]. Greater benefit comes from the ability to track gamma rays through the detector. Current limitations on the sensitivity stem from limiting the analysis to gamma rays which only interact in two segments which reduces the detection efficiency markedly and does not consider the possibility of multiple interactions within a segment which could be resolved by signal decomposition. The gamma-ray tracking algorithms discussed by Schmid et al. [96] would deduce the correct ordering of the first and second interaction points  $\sim 80\%$  of the time for a 2 mm position resolution. This increases the efficiency of detecting the relevant Compton scattering events by a factor of three. The combined improvements in sensitivity and detection efficiency will result in a figure-of-merit roughly 12 times better than SeGA. Furthermore, this does not consider the benefits from measuring the continuous distribution of the first scattering angle.

With these improvements, angular distribution and linear polarization measurements will become accessible for many more transitions. With the increased efficiency, one can even consider the possibility going further and consider  $\gamma$ - $\gamma$  angular correlations to give more information. A sizable piece of this improvement is also available to detectors in SeGA by using the Digital Data Acquisition System. This opens the opportunity to probe the spins and parities of excited states in many exotic nuclei.



# Chapter 7

## Conclusions

Knockout reactions are a powerful spectroscopic tool to explore the structure of exotic nuclei. In particular, proton knockout reactions on neutron-rich nuclei access even more rare isotopes. Furthermore, the nuclear spins of the reaction residues are aligned following the removal of the proton. This results in the angular distribution and linear polarization of the emitted gamma rays. Measurement of the distribution and polarization allows for spin and parity assignment of the populated states when combined with the information from the knockout selection rules or from previous experiments.

For  $^{31}\text{Mg}$ , two levels were identified as the normal shell model states with no excitations across the  $N = 20$  shell gap. The spacing between these levels agrees with those produced by a USD shell model calculation. Assignment of the spins of the populated states was possible by examining the angular distribution of the gamma rays in a momentum-constrained analysis which removes the possible systematic uncertainty related to the efficiency of the gamma-ray detector. Parities could also be tentatively assigned based on linear polarization measurements, knockout selection rules, and Weisskopf estimates of transition rates. A quenching of spectroscopic strength was observed in the reaction which agrees well with trends for the removal

of a deeply-bound nucleon [77].

The lowest-lying state with normal shell ordering was also identified in the  $^{33}\text{Mg}$  nucleus after a proton was stripped from the  $^{34}\text{Al}$  nucleus. Due to the more complicated structure of the incoming  $^{34}\text{Al}$ , a fragmentation of strength was also identified to several  $2p2h$  states in the residue. As no prior spins and parities are firmly established in  $^{33}\text{Mg}$ , absolute spin and parity assignments are not possible. However, information from the gamma-ray transitions suggests certain multipolarities for the decays from the low-lying states. A level scheme is proposed which agrees well with a recent measurement of the ground-state spin [69] as well as Coulomb excitation data [70].

The identification of the states with no excitations across the  $N = 20$  shell gap contributes to the knowledge of the “island of inversion”. The qualitative location of these states in the level schemes are predicted well by calculations, but true quantitative agreement for all the states is difficult to reproduce. For  $^{31,33}\text{Mg}$ , the excitation energy of the lowest-lying state with a normal configuration above the inverted ground state remains relatively constant showing the similarity between these two isotopes. Similar investigations into more neutron-rich magnesium isotopes (as well as neon isotopes) would add additional understanding about this region and the interactions which are responsible for the inversion.

Future improvements will make a wide swath of exotic nuclei accessible for exploration. As the shell structure evolves, methods of making model-independent spin and parity assignments are especially critical. Gamma-ray angular distribution and linear polarization measurements will be an essential part to probe this evolving structure. Next-generation arrays of gamma ray detectors implementing digital data acquisition will have an increased sensitivity for making these measurements. The techniques established in the present work will allow future experiments to effectively harness this sensitivity to enrich our knowledge about the atomic nucleus.

# Appendix A

## Gamma-ray angular distribution

Many different styles of notation exist in the literature; here we rely on the definitions of Krane [103] as in Olliver et al. [43]. In this notation, the angular distribution is decomposed into a series of Legendre polynomials,  $P_\lambda$ , in the angle  $\theta$  with respect to the beam axis:

$$W(\theta) = \sum_{\lambda=0}^{2l'} A_\lambda(J_i, J_f, \delta) B_\lambda(J_i, \sigma) P_\lambda(\cos \theta) \quad (\text{A.1})$$

for a gamma ray transition between an initial state with spin  $J_i$  and a final state  $J_f$ . This depends on a quantity  $B_\lambda$  that characterizes the initial spin orientation in the nucleus described by the parameter  $\sigma$  (see Eq. A.4).  $A_\lambda$  captures the characteristics of the transition including the mixing ratio  $\delta$  of electric and magnetic matrix elements. The expansion is taken up to order  $l' = l + 1$  where  $l$  is the minimum multipolarity of the transition dictated by the triangle relation.

$$l = |J_i - J_f| \quad (\text{A.2})$$

The transition probability for different multiplicities is roughly proportional to  $(Er_0/\hbar c)^{2l+1}$ . For typical gamma ray energies  $E$  and nuclear densities  $r_0 \approx 1.2\text{fm}$ ,  $Er_0 \ll \hbar c$ , so higher orders of the angular distribution are negligible. Furthermore,

for spin orientation along an axis that is azimuthally symmetric, only even order Legendre polynomials contribute.

The spin alignment depends on the reaction mechanism. Each reaction mechanism preferentially populates different magnetic substates in the reaction residues, where the magnetic substate  $m$  is the projection of the total nuclear spin,  $J$ , along the beam axis, i.e.  $m = J_z$ . The reaction thus populates a distribution  $w(m)$  of the magnetic substates which is then normalized to unity. The coefficients  $B_\lambda$  depend on this substate distribution

$$B_\lambda(J_i, \sigma) = \sqrt{(2\lambda + 1)(2J_i + 1)} \sum_{m=-J_i}^{J_i} (-1)^{J_i+m} \begin{pmatrix} J_i & J_i & \lambda \\ -m & m & 0 \end{pmatrix} w(m; \sigma). \quad (\text{A.3})$$

Typically, the substate distribution is taken to fit according to some model parameterized by  $\sigma$ . In a given reaction, there is either a tendency to produce spins aligned with the quantization axis (prolate alignment,  $m = \pm J_i$ ) or perpendicular to it (oblate alignment,  $m = 0$ ). A reasonable approximation to the substate distribution in the case of the oblate alignment is a Gaussian with zero mean as studied by Yamazaki [104] based upon work done by Diamond et al. [105]. With the proper normalization, the distribution has the form

$$w(m) = \frac{e^{-m^2/2\sigma^2}}{\sum_{m'=-J_i}^{J_i} e^{-m'^2/2\sigma^2}}. \quad (\text{A.4})$$

Note that this takes into account the azimuthal symmetry of the reaction, so  $w(m) = w(-m)$ . The Gaussian distribution has a width  $\sigma$  which is connected to the amount of oblate alignment in the system. The maximal alignment happens when  $\sigma \rightarrow 0$  where only  $m = 0$  is populated in the reaction. This results in a maximal alignment

Table A.1: Maximum alignment coefficients for different types of alignment.

$$\rho_{20}^{\max}(J_i) = \frac{B_2^{\max}(J_i)}{\sqrt{5}} \left| \begin{array}{c} \text{prolate} \\ \sqrt{\frac{J_i(2J_i-1)}{(J_i+1)(2J_i+3)}} \end{array} \right| \begin{array}{c} \text{oblate (half-integer J)} \\ -\frac{1}{4} \sqrt{\frac{(2J_i-1)(2J_i+3)}{J_i(J_i+1)}} \end{array} \left| \begin{array}{c} \text{oblate (integer J)} \\ -\sqrt{\frac{J_i(J_i+1)}{(2J_i-1)(2J_i+3)}} \end{array} \right|$$

for a given spin from Eq. A.3 of

$$B_{\lambda,\text{ob}}^{\max}(J_i) = \sqrt{(2\lambda+1)(2J_i+1)}(-1)^{J_i} \begin{pmatrix} J_i & J_i & \lambda \\ 0 & 0 & 0 \end{pmatrix} \quad (\text{A.5})$$

$$B_{\lambda,\text{ob}}^{\max}(J_i) = \sqrt{(2\lambda+1)(2J_i+1)}(-1)^{J_i+1/2} \begin{pmatrix} J_i & J_i & \lambda \\ -1/2 & 1/2 & 0 \end{pmatrix}$$

for integer and half-integer spins respectively. Similarly, for prolate alignment, the formula can be extended to favor the states  $m = \pm J_i$  [44] with a Gaussian distribution about both. Accordingly, the substate distribution is

$$w(m) = \frac{e^{-(J_i-|m|)^2/2\sigma^2}}{\sum_{m'=-J_i}^{J_i} e^{-(J_i-|m'|)^2/2\sigma^2}} \quad (\text{A.6})$$

which leads to a maximal alignment coefficient of

$$B_{\lambda,\text{pro}}^{\max}(J_i) = \sqrt{(2\lambda+1)(2J_i+1)} \begin{pmatrix} J_i & J_i & \lambda \\ -J_i & J_i & 0 \end{pmatrix}. \quad (\text{A.7})$$

The amount of alignment is often cited in terms of the percentage of this maximum,  $B_{\text{rel}}(J_i, \sigma) = B_2(J_i, \sigma)/B_2^{\max}(J_i)$ . This is related to  $B_2$  since the higher order terms in the angular distribution have a considerably smaller effect on the experimental observables for the typical experiment. The reduced form of the maximum alignment coefficient is shown in Table A.1 where  $\rho_{\lambda 0} = B_{\lambda 0}/(2\lambda+1)$  is another coefficient of alignment commonly used in the literature. It is important to note that  $B_2(J_i) > 0$

for prolate alignment while  $B_2(J_i) < 0$  for oblate alignment.

Once there exists some degree of alignment in the nucleus, the gamma rays emitted will exhibit an angular distribution with respect to the alignment axis. The alignment condition automatically precludes angular distribution from  $J_i = 0$  and  $J_i = 1/2$  states for axially symmetric arrangements. The distribution of the gamma rays is related to the properties of the transition. This is described by the coefficient  $A_\lambda(J_i, J_f, \delta)$  which has the form

$$A_\lambda(J_i, J_f, \delta) = \frac{1}{1 + \delta^2} \left( F_\lambda(L, L, J_f, J_i) + 2\delta F_\lambda(L, L + 1, J_f, J_i) + \delta^2 F_\lambda(L + 1, L + 1, J_f, J_i) \right) \quad (\text{A.8})$$

for a transition of a given multipolarity  $L$  expressed in terms of generalized  $F$ -coefficients. For a specific transition, magnetic and electric matrix elements can contribute to the transition. These must have the same change in parity though. For magnetic transitions, the parity change is  $\Delta\pi = (-1)^{L+1}$ , and for electric transitions we have  $\Delta\pi = (-1)^L$ . That is to say that a transition with a given character of multipolarity  $L$  mixes with the transition of opposite character with multipolarity  $L + 1$ . As higher multipolarity transitions are often greatly hindered due to the energy dependence of the transition rate, higher order contributions to the mixing are ignored. The mixing is quantified by the mixing ratio  $\delta$  with

$$\delta = \frac{\langle J_f | T(\pi(L + 1)) | J_i \rangle}{\langle J_f | T(\pi' L) | J_i \rangle} \quad (\text{A.9})$$

defined in terms of the rates  $T$  for transitions with character  $\pi$  or opposite character  $\pi'$ . For a pure transition of multipolarity  $L$  (i.e.  $\delta = 0$ ), the angular distribution coefficient in Eq. A.8 becomes  $A_\lambda = F_\lambda(L, L, J_f, J_i)$ . The  $F$  coefficients are defined according to the generalized  $F$  coefficients [106] where only one gamma ray is observed

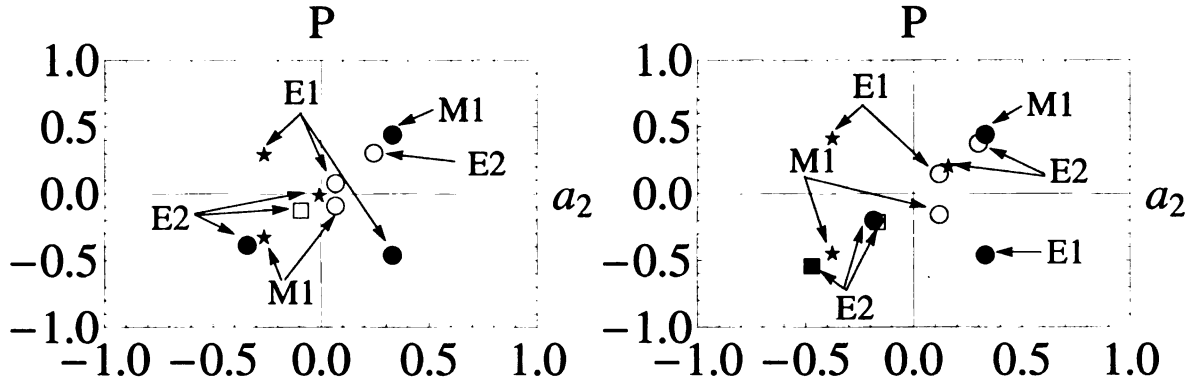


Figure A.1: Angular distribution coefficients and linear polarizations at  $\theta_{c.m.} = 113^\circ$  relevant to the current work for transitions with  $\Delta J = -2, -1, 0, 1, 2$  (filled squares, filled circles, stars, hollow circles, hollow squares respectively) given an initial 66% prolate alignment in a nucleus with initial spin  $3/2$  (left) or  $5/2$  (right).

with relation to the alignment axis. These coefficients are then

$$F_\lambda(L, L', J_f, J_i) = (-1)^{J_i + J_f + 1} \sqrt{(2\lambda + 1)(2L + 1)(2L' + 1)(2J_i + 1)} \\ \times \begin{pmatrix} L & L' & \lambda \\ 1 & -1 & 0 \end{pmatrix} \begin{Bmatrix} L & L' & \lambda \\ J_i & J_i & J_f \end{Bmatrix}. \quad (\text{A.10})$$

A table of  $F$  coefficients can be found in the compilation by Wapstra [107]. Angular distribution is also accompanied by linear polarization of the gamma rays. For mixed dipole transitions, the resulting polarization at a given angle is:

$$P(\theta) = \pm \left( 3a_2 \sin^2 \theta + a_4 \left( \frac{5}{4} \sin^2 \theta - \frac{35}{16} \sin^2 2\theta \right) - 8 \sin^2 \theta \right) \\ \times \sum_m w(m) (-1)^{J+m} \sqrt{5(2J+1)} \begin{pmatrix} J & J & 2 \\ m & -m & 0 \end{pmatrix} * \frac{\delta}{1 + \delta^2} \quad (\text{A.11}) \\ \div \left( 2 + a_2(2 - 3 \sin^2 \theta) + a_4 \left( 2 - \frac{5}{4} \sin^2 \theta - \frac{35}{16} \sin^2 2\theta \right) \right).$$

Determination of  $a_2$  and  $P$  identifies the multipolarity of the transition. For similar nuclear alignments, pure transitions of the same multipolarity and  $\Delta J$  lie in a similar position in the  $a_2$ - $P$  plane irrespective of initial spin as shown in Fig. A.1 and often

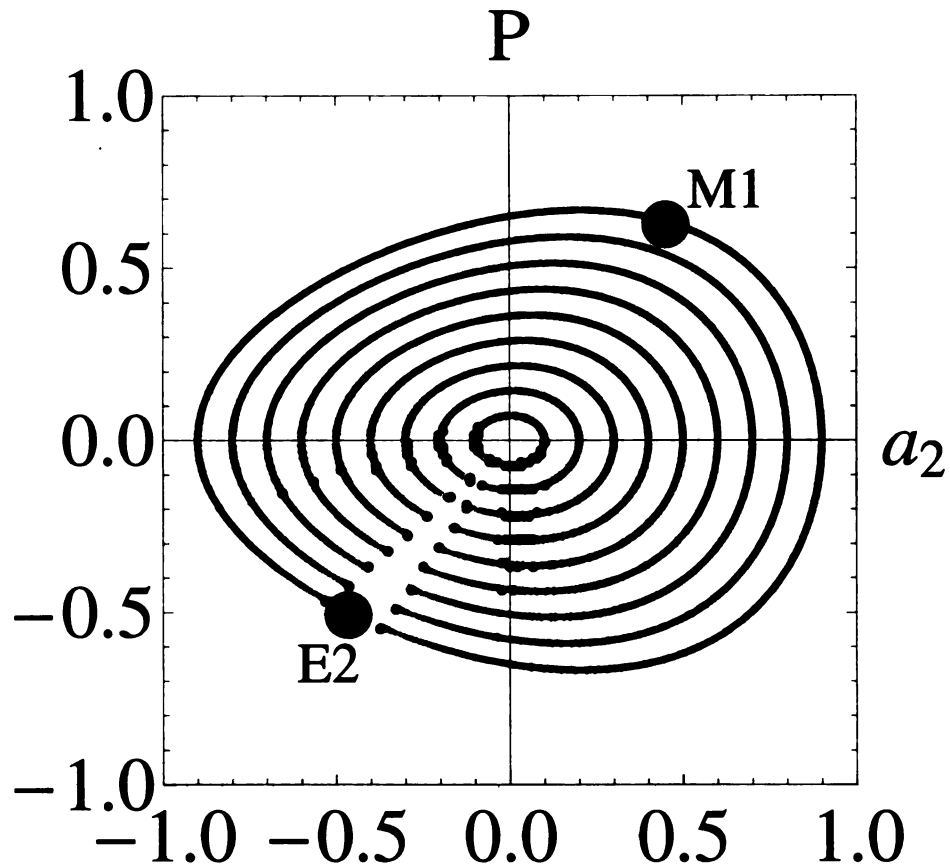


Figure A.2: Angular distribution coefficients and linear polarizations for a mixed  $M1/E2$  transition ( $3/2 \rightarrow 1/2$ ) for different initial alignments from 10% (innermost) to 90% (outermost) prolate alignment. The curves represent mixed transitions with  $\delta \in [-20, 20]$ .

determination of solely the signs of  $a_2$  and  $P$  provides the necessary information about the multipolarity. The magnitude of these observables is also dependent on the amount of spin alignment in the initial nucleus as well as the mixing angle for the gamma-ray transition (see Fig. A.2).

If several gamma rays are emitted in a cascade, their directions of propagation are also related. If only one of these is detected, then the correlation must be integrated over the possible directions of any intermediate unobserved gamma rays. In general, this has an effect of dealigning the nucleus. The reduction of the alignment coefficient



$B_\lambda$  is given by the deorientation coefficient  $U_\lambda$  as

$$U_\lambda(L, L', \delta, J_1, J_2) = \frac{U_\lambda(L, J_1, J_2) + \delta^2 U_\lambda(L', J_1, J_2)}{1 + \delta^2} \quad (\text{A.12})$$

for an unobserved transition ( $J_1 \rightarrow J_2$ ) with mixed multipolarity  $L, L'$  with a known mixing ratio  $\delta$ . The appropriate  $U_\lambda$  for the pure transitions are

$$U_\lambda(L, J_1, J_2) = (-1)^{J_1+J_2+L+\lambda} \sqrt{(2J_1+1)(2J_2+1)} \begin{Bmatrix} J_1 & J_1 & \lambda \\ J_2 & J_2 & L \end{Bmatrix}. \quad (\text{A.13})$$

The final alignment parameter for  $N$  unobserved intermediate transitions between levels  $J_i$  and  $J_{i+1}$  would be

$$B'_\lambda(J_{N+1}, \sigma) = U_\lambda(L_1, L'_1, \delta_1, J_1, J_2) \dots U_\lambda(L_n, L'_n, \delta, J_N, J_{N+1}) B_\lambda(J_i, \sigma), \quad (\text{A.14})$$

given the known multipolarities  $L_i, L'_i$  and mixing ratios  $\delta_i$  of the intermediate transitions.

# Appendix B

## Relativistic Kinematics

The gamma rays emitted from a source with a relativistic velocity can display asymmetries in the lab frame where none exist in the intrinsic frame. Understanding the relativistic effects is necessary to make statements about the asymmetries in the intrinsic frame from the lab measurements. If we consider the coordinate system with the particle moving with velocity  $\beta c$  along the  $z$ -axis, the photon emitted in a direction  $\theta_{\text{lab}}$  frame can be related back to the intrinsic frame through the Lorentz transformation of the four-vectors.

$$\Lambda_{\mu}^{\nu} = \begin{pmatrix} \gamma & 0 & 0 & \beta\gamma \\ 0 & 1 & 0 & 0 \\ 0 & 0 & 1 & 0 \\ \beta\gamma & 0 & 0 & \gamma \end{pmatrix} \quad (\text{B.1})$$

where  $\gamma = (1 - \beta^2)^{-1/2}$ . This influences important observables of the gamma ray including energy and angle of emission as well as the lifetimes of excited states in nuclei. However, the transformation of polarization is simply connected to the difference of the angle of emission in the two reference frames.

## B.1 Lifetime

The Lorentz transformation on the standard position four-vector at time  $t$  and location  $\mathbf{x}$

$$x^\mu = (ct, \mathbf{x}) \quad (\text{B.2})$$

results in time dilation in the lab frame. Lifetimes measured in the lab frame are simply related through the  $\gamma$  factor.

$$\tau_{\text{cm}} = \tau_{\text{lab}}/\gamma \quad (\text{B.3})$$

## B.2 Angle

The related between angles in the lab frame versus the center-of-mass frame can be determined by Lorentz boosting the four-frequency

$$N^\mu = 2\pi\omega(1, \hat{\mathbf{n}}) \quad (\text{B.4})$$

for a photon with frequency  $\omega$  propagating in the  $\hat{\mathbf{n}}$  direction. This gives the result:

$$\begin{aligned} \cos \theta_{\text{CM}} &= \frac{\cos \theta_{\text{lab}} - \beta}{1 - \beta \cos \theta_{\text{lab}}} \\ \sin \theta_{\text{CM}} &= \frac{\sin \theta_{\text{lab}}}{\gamma(1 - \beta \cos \theta_{\text{lab}})} \end{aligned} \quad (\text{B.5})$$

This transformation of angle also impacts the solid angle  $d\Omega = d(\cos \theta)$  effectively boosting the gamma rays forward in the lab frame.

$$\frac{d\Omega_{\text{CM}}}{d\Omega_{\text{lab}}} = \frac{1 - \beta^2}{(\beta \cos \theta_{\text{lab}} - 1)^2} \quad (\text{B.6})$$

### B.3 Energy

The familiar relativistic Doppler shift equation can also be obtained by transformation of the four-frequency (Eq. B.4) With the energy  $E$  proportional to the frequency, the intrinsic energy is

$$E_{\text{lab}} = E_{\text{cm}}\gamma(1 + \beta \cos \theta_{\text{cm}}). \quad (\text{B.7})$$

Utilizing the relation B.5, the intrinsic gamma ray energy can be expressed in terms of the lab measurements

$$E_{\text{cm}} = \gamma E_{\text{lab}}(1 - \beta \cos \theta_{\text{lab}}). \quad (\text{B.8})$$

### B.4 Polarization

The linear polarization of light could also be affected by the relativistic kinematics. Here, the measured quantity of interest is the asymmetry of Compton scattering. This is directly related to the magnitude of the electric fields  $\mathbf{E}$  parallel and perpendicular to the scattering plane in the lab frame.

$$A = \frac{E_{\parallel}^2 - E_{\perp}^2}{E_{\parallel}^2 + E_{\perp}^2} \quad (\text{B.9})$$

To investigate the components of the electric field relative to the scattering plane, we must utilize the field-strength tensor containing the electric and magnetic fields,

$$F_{\mu\nu} = \begin{pmatrix} 0 & E_x & E_y & E_z \\ -E_x & 0 & -B_z & B_y \\ -E_y & B_z & 0 & -B_x \\ -E_z & -B_y & B_x & 0 \end{pmatrix}. \quad (\text{B.10})$$

Applying the Lorentz transformation for a boost of velocity  $\boldsymbol{\beta}c$ , we obtain the result for the transformed field-strength tensor  $F_{\lambda\rho} = \Lambda_{\rho}^{\nu}F_{\mu\nu}\Lambda_{\lambda}^{\mu}$  which gives us the desired transformation of the electric field.

$$\mathbf{E} = \gamma(\mathbf{E}' - \boldsymbol{\beta} \times \mathbf{B}') - \frac{\gamma^2}{\gamma + 1}\boldsymbol{\beta}(\boldsymbol{\beta} \cdot \mathbf{E}') \quad (\text{B.11})$$

However, the scattering angles are also transformed between the lab frame and the intrinsic frame. If we consider the scattering to occur in the  $xz$ -plane, then the parallel and perpendicular components for a photon scattering in the  $\hat{\mathbf{n}}$  direction are related to the basis vectors in the intrinsic frame

$$\begin{aligned} \hat{\mathbf{n}}' &= \sin \theta' \hat{\mathbf{e}}'_x + \cos \theta' \hat{\mathbf{e}}'_z \\ \hat{\mathbf{e}}'_{\parallel} &= \cos \theta' \hat{\mathbf{e}}'_x - \sin \theta' \hat{\mathbf{e}}'_z \\ \hat{\mathbf{e}}'_{\perp} &= \hat{\mathbf{e}}'_y \end{aligned} \quad (\text{B.12})$$

with similar definitions with unprimed quantities for the lab frame. We then can relate the perpendicular component of the electric field measured in the lab to that in the intrinsic frame.

$$E_{\perp} = \mathbf{E} \cdot \hat{\mathbf{e}}_{\perp} = E_y = \gamma(E'_y - \beta B'_x) \quad (\text{B.13})$$

For the electromagnetic radiation of the photon, the magnetic field can be expressed in terms of the electric field and direction of propagation via  $\mathbf{B}' = \hat{\mathbf{n}}' \times \mathbf{E}'$ . This gives us the simple result

$$E_{\perp} = E'_{\perp} \cdot \gamma(1 + \beta \cos \theta'). \quad (\text{B.14})$$

Likewise if we perform the transformation on the parallel component of the electric field, we can obtain a similar relation. This requires the more involved task of

transforming the angles accordingly, but it can be shown that we achieve

$$E_{\parallel} = E'_{\parallel} \cdot \gamma(1 + \beta \cos \theta'). \quad (\text{B.15})$$

Combining equations B.14 and B.15, the asymmetry of the electric field (B.9) is invariant under Lorentz transformation. Thus the measured polarization in the lab frame is related to the intrinsic frame solely through the transformation of the according angle of emission,  $P(\theta) = P(\theta')$ , given a linear relationship between the asymmetry and the linear polarization.

# BIBLIOGRAPHY

- [1] Aage Bohr and Ben R. Mottelson. *Nuclear Structure*, volume 1. World Scientific, Singapore, 3rd edition, 1998.
- [2] T. Hamada and I. D. Johnston. A potential model representation of two-nucleon data below 315 MeV. *Nucl. Phys.*, 34:382–403, 1962.
- [3] R. B. Wiringa, V. G. J. Stoks, and R. Schiavilla. Accurate nucleon-nucleon potential with charge-independence breaking. *Phys. Rev. C*, 51:38–51, 1995.
- [4] M. G. Mayer and H. D. Jensen. *Elementary Theory of Nuclear Shell Structure*. John Wiley and Sons, inc., New York, 1955.
- [5] B. A. Brown. The nuclear shell model towards the drip lines. *Prog. Part. Nucl. Phys.*, 47:517–599, 2001.
- [6] P. D. Cottle and K. W. Kemper. Evolution of shell closures in neutron-rich  $Z = 10$ – $20$  nuclei. *Phys. Rev. C*, 66:061301, 2002.
- [7] R. V. F Janssens. Nuclear physics: Unexpected doubly magic nucleus. *Nature*, 459:1069–1070, 2009.
- [8] P. G. Hansen. Nuclear halos: Structure and reactions. *Nucl. Phys. A*, 588:c1 – c9, 1995. Proceedings of the Fifth International Symposium on Physics of Unstable Nuclei.
- [9] J. R. Terry, D. Bazin, B. A. Brown, J. Enders, T. Glasmacher, P. G. Hansen, B. M. Sherrill, and J. A. Tostevin. Absolute spectroscopic factors from neutron knockout on the halo nucleus  $^{15}\text{C}$ . *Phys. Rev. C*, 69:054306, 2004.
- [10] B. A. Brown. New Skyrme interaction for normal and exotic nuclei. *Phys. Rev. C*, 58:220–231, 1998.
- [11] B.H. Wildenthal. Empirical strengths of spin operators in nuclei. *Prog. Part. Nucl. Phys.*, 11:5, 1984.

- [12] T. Otsuka, R. Fujimoto, Y. Utsuno, B. A. Brown, M. Honma, and T. Mizusaki. Magic numbers in exotic nuclei and spin-isospin properties of the  $NN$  interaction. *Phys. Rev. Lett.*, 87:082502, 2001.
- [13] E. K. Warburton, J. A. Becker, and B. A. Brown. Mass systematics for  $A = 29 - 44$  nuclei: The deformed  $A \sim 32$  region. *Phys. Rev. C*, 41:1147, 1990.
- [14] D. Guillemaud-Mueller, C. Detraz, M. Langevin, F. Naulin, M. De Saint-Simon, C. Thibault, F. Touchard, and M. Epherre.  $\beta$ -decay schemes of very neutron-rich sodium isotopes and their descendants. *Nucl. Phys.*, A426:37-76, 1984.
- [15] T. Motobayashi, Y. Ikeda, Y. Ando, K. Ieki, M. Inoue, N. Iwasa, T. Kikuchi, M. Kurokawa, S. Moriya, S. Ogawa, H. Murakami, S. Shimoura, Y. Yanagisawa, T. Nakamura, Y. Watanabe, M. Ishihara, T. Teranishi, H. Okuno, and R. F. Casten. Large deformation of the very neutron-rich nucleus  $^{32}\text{Mg}$  from intermediate-energy Coulomb excitation. *Phys. Lett. B*, 346:9-14, 1995.
- [16] B. V. Pritychenko, T. Glasmacher, P. D. Cottle, M. Fauerbach, R. W. Ibbotson, K. W. Kemper, V. Maddalena, A. Navin, R. Ronningen, A. Sakharuk, H. Scheit, and V. G. Zelevinsky. Role of intruder configuration in  $^{26,28}\text{Ne}$  and  $^{30,32}\text{Mg}$ . *Phys. Lett. B*, 461:322-328, 1999.
- [17] D.J. Viera, J. M. Wouters, K. Vaziri Jr., R. H. Kraus, H. Wollnik, G. W. Butler, F. K. Wohn, and A. H. Wapstra. Direct mass measurement of neutron-rich light nuclei near  $N = 20$ . *Phys. Rev. Lett.*, 57:3253, 1986.
- [18] A. Navin, D. W. Anthony, T. Aumann, T. Baumann, D. Bazin andd Y. Blumenfeld, B. A. Brown, T. Glasmacher, P. G. Hansen, R. W. Ibbotson, P. A. Lofy, V. Maddalena, K. Miller, T. Nakamura, B. V. Pritychenko, B. M. Sherrill, E. Spears, M. Steiner, J. A. Tostevin, J. Yurkon, and A. Wagner. Direct evidence for the breakdown of the  $N = 8$  shell closure in  $^{12}\text{Be}$ . *Phys. Rev. Lett.*, 85:266-269, 2000.
- [19] S. D. Pain, W. N. Catford, N. A. Orr, J. C. Angélique, N. I. Ashwood, V. Bouchat, N. M. Clarke, N. Curtis, M. Freer, B. R. Fulton, F. Hanappe, M. Labiche, J. L. Lecouey, R. C. Lemmon, D. Mahboub, A. Ninane aond G. Normand, N. Soić, L. Suttge, C. N. Timis, J. A. Tostevin, J. S. Winfield, and V. Ziman. Structure of  $^{12}\text{Be}$ : Intruder  $d$ -wave strength at  $N = 8$ . *Phys. Rev. Lett.*, 96:032502, 2006.
- [20] G. Neyens, M. Kowalska, D. Yordanov, K. Blaum, P. Himpe, P. Lievens, S. Mallion, R. Neugart, N. Vermeulen, Y. Utsuno, and T. Otsuka. Measurement of the spin and magnetic moment of  $^{31}\text{Mg}$ : Evidence for a strongly deformed intruder ground state. *Phys. Rev. Lett.*, 94:022501, 2005.
- [21] D. T. Yordanov, M. Kowalska, K. Blaum, M. De Rydt, K. T. Flanagan, P. Lievens, R. Neugart, G. Neyens, and H. H. Stroke. Spin and magnetic



- moment of  $^{33}\text{Mg}$ : Evidence for a negative-parity intruder ground state. *Phys. Rev. Lett.*, 99:212501, 2007.
- [22] M. Kowalska, D. T. Yordanov, K. Blaum, P. Himpe, P. Lievens, S. Mallion, R. Neugart, G. Neyens, and N. Vermeulen. Nuclear ground-state spins and magnetic moments of  $^{27}\text{Mg}$ ,  $^{29}\text{Mg}$ , and  $^{31}\text{Mg}$ . *Phys. Rev. C*, 77:034307, 2008.
- [23] J. R. Terry, B. A. Brown, C. M. Campbell, J. M. Cook, A. D. Davies, D.-C. Dinca, A. Gade, T. Glasmacher, P. G. Hansen, B. M. Sherrill, H. Zwahlen, D. Bazin, K. Yoneda, J. A. Tostevin, T. Otsuka, Y. Utsuno, and B. Pritychenko. Single-neutron knockout from intermediate energy beams of  $^{30,32}\text{Mg}$ : Mapping the transition into the “island of inversion”. *Phys. Rev. C*, 77:014316, 2008.
- [24] A. Gade, P. Adrich, D. Bazin, M. D. Bowen, B. A. Brown, C. M. Campbell, J. M. Cook, S. Ettenauer, T. Glasmacher, K. W. Kemper, S. McDaniel, A. Obertelli, T. Otsuka, A. Ratkiewicz, K. Siwek, J. R. Terry, J. A. Tostevin, Y. Utsuno, and D. Weisshaar. Spectroscopy of  $^{36}\text{Mg}$ : Interplay of normal and intruder configurations at the neutron-rich boundary of the “island of inversion”. *Phys. Rev. Lett.*, 99:072502, 2007.
- [25] H. Iwasaki, T. Motobayashi, H. Sakurai, K. Yoneda, T. Gomi, N. Aoi, N. Fukuda, Zs. Flp, U. Futakami, Z. Gacsi, Y. Higurashi, N. Imai, N. Iwasa, T. Kubo, M. Kunibu, M. Kurokawa, Z. Liu, T. Minemura, A. Saito, M. Serata, S. Shimoura, S. Takeuchi, Y.X. Watanabe, K. Yamada, Y. Yanagisawa, and M. Ishihara. Quadrupole collectivity of  $^{28}\text{Ne}$  and the boundary of the island of inversion. *Phys. Lett. B*, 620:118 – 124, 2005.
- [26] P. G. Hansen and J. A. Tostevin. Direct reactions with exotic nuclei. *Annual Review of Nuclear and Particle Science*, 53:219–261, 2003.
- [27] J.A. Tostevin. Single-nucleon knockout reactions at fragmentation beam energies. *Nucl. Phys. A*, 682:320c, 2001.
- [28] P. G. Hansen and B. M. Sherrill. Reactions and single-particle structure of nuclei near the drip lines. *Nucl. Phys. A*, 693:133–168, 2001.
- [29] A. S. Goldhaber. Statistical models of fragmentation processes. *Phys. Lett. B*, 53:306–308, 1974.
- [30] Peter A. Zavodsky, Hannu Koivisto, Dallas Cole, and Peter Miller. Emittance studies of ARTEMIS – the new ECR ion source for the Coupled Cyclotron Facility at NSCL/MSU. In J.L. Duggan and I.L. Morgan, editors, *The CAARI 2000: Sixteenth international conference on the application of accelerators in research and industry*, volume 576, pages 619–622. American Institute of Physics, 2001.
- [31] X. Wu, H. Blosser, D. Johnson, F. Marti, and R.C. York. The K500-to-K1200 coupling line for the Coupled Cyclotron Facility at the NSCL. In *Proceedings of the 1999 Particle Accelerator Conference*, pages 1318–1320, New York, 1999.

- [32] D. J. Morrissey, B. M. Sherrill, M. Steiner, A. Stolz, and I. Wiedenhoever. Commissioning the A1900 projectile fragment separator. *Nucl. Instrum. Meth. B*, 204:90–96, 2003.
- [33] W.-M. Yao, C. Amsler, D. Asner, R.M. Barnett, J. Beringer, P.R. Burchat, C.D. Carone, C. Caso, O. Dahl, G. D’Ambrosio, A. DeGouvea, M. Doser, S. Eidelman, J.L. Feng, T. Gherghetta, M. Goodman, C. Grab, D.E. Groom, A. Gurtu, K. Hagiwara, K.G. Hayes, J.J. Hernández-Rey, K. Hikasa, H. Jawahery, C. Kolda, Kwon Y., M.L. Mangano, A.V. Manohar, A. Masoni, R. Miquel, K. Mönig, H. Murayama, K. Nakamura, S. Navas, K.A. Olive, L. Pape, C. Patrignani, A. Piepke, G. Punzi, G. Raffelt, J.G. Smith, M. Tanabashi, J. Terning, N.A. Törnqvist, T.G. Trippe, P. Vogel, T. Watari, C.G. Wohl, R.L. Workman, P.A. Zyla, B. Armstrong, G. Harper, V.S. Lugovsky, P. Schaffner, M. Artuso, K.S. Babu, H.R. Band, E. Barberio, M. Battaglia, H. Bichsel, O. Biebel, P. Bloch, E. Blucher, R.N. Cahn, D. Casper, A. Cattai, A. Cecucci, D. Chakraborty, R.S. Chivukula, G. Cowan, T. Damour, T. DeGrand, K. Desler, M.A. Dobbs, M. Drees, A. Edwards, D.A. Edwards, V.D. Elvira, J. Erler, V.V. Ezhela, W. Fetscher, B.D. Fields, B. Foster, D. Froidevaux, T.K. Gaisser, L. Garren, H.-J. Gerber, G. Gerbier, L. Gibbons, F.J. Gilman, G.F. Giudice, A.V. Gritsan, M. Grünewald, H.E. Haber, C. Hagmann, I. Hinchliffe, A. Höcker, P. Igo-Kemenes, J.D. Jackson, K.F. Johnson, D. Karlen, B. Kayser, D. Kirkby, S.R. Klein, K. Kleinknecht, I.G. Knowles, R.V. Kowalewski, P. Kreitz, B. Krusche, Yu.V. Kuyanov, O. Lahav, P. Langacker, A. Liddle, Z. Ligeti, T.M. Liss, L. Littenberg, L. Liu, K.S. Lugovsky, S.B. Lugovsky, T. Mannel, D.M. Manley, W.J. Marciano, A.D. Martin, D. Milstead, M. Narain, P. Nason, Y. Nir, J.A. Peacock, S.A. Prell, A. Quadt, S. Raby, B.N. Ratcliff, E.A. Razuvaev, B. Renk, P. Richardson, S. Roesler, G. Rolandi, M.T. Roman, L.J. Rosenberg, C.T. Sachrajda, S. Sarkar, M. Schmitt, O. Schneider, D. Scott, T. Sjöstrand, G.F. Smoot, P. Sokolsky, S. Spanier, H. Spieler, A. Stahl, T. Stanev, R.E. Streitmatter, T. Sumiyoshi, N.P. Tkachenko, G.H. Trilling, G. Valencia, K. van Bibber, M.G. Vincter, D.R. Ward, B.R. Webber, J.D. Wells, M. Whalley, L. Wolfenstein, J. Womersley, C.L. Woody, A. Yamamoto, O.V. Zenin, J. Zhang, and R.-Y. Zhu. Review of Particle Physics. *J. Phys. G.*, 33:1, 2006.
- [34] D. Bazin, J. A. Caggiano, B. M. Sherrill, J. Yurkon, and A. Zeller. The S800 spectrograph. *Nucl. Instrum. Meth. B*, 204:629–633, 2003.
- [35] J. Yurkon, D. Bazin, W. Benenson, D. J. Morrissey, B. M. Sherrill, D. Swan, and R. Swanson. Focal plane detector for the S800 high-resolution spectrometer. *Nucl. Instrum. Meth. A*, 422:291, 1999.
- [36] C. Scheidenberger, Th. Stöhlker, W. E. Meyerhof, H. Geissel, P. H. Mokler, and B. Blank. Charge states of relativistic heavy ions in matter. *Nucl. Instrum. Meth. A*, 142:441–462, 1998.

- [37] Kyoko Makino and Martin Berz. Cosy infinity version 8. *Nucl. Instrum. Meth. A*, 427:338–343, 1999.
- [38] S. Agostinelli, J. Allison, K. Amako, J. Apostolakis, H. Araujo, P. Arce, M. Asai, D. Axen, S. Banerjee, G. Barrand, F. Behner, L. Bellagamba, J. Boudreau, L. Brogna, A. Brunengo, H. Burkhardt, S. Chauvie, J. Chuma, R. Chytracsek, G. Cooperman, G. Cosmo, P. Degtyarenko, A. Dell’Acqua, G. Depaola, D. Dietrich, R. Enami, A. Feliciello, C. Ferguson, G. Folger, Foppiano. F., A. Forti, S. Garelli, S. Giani, R. Giannitrapani, D. Gibin, J. J. Gómez Cadenas, I. González, G. Gracia Abril, G. Greeniaus, W. Greiner, V. Grichine, A. Grossheim, S. Guatelli, P. Gumplinger, R. Hamatsu, K. Hashimoto, H. Hasei, A. Heikkinen, A. Howard, V. Ivanchenko, A. Johnson, F. W. Jones, J. Kallenbach, N. Kanaya, M. Kawabata, Y. Kawabata, M. Kawaguti, S. Kellner, P. Kent, A. Kimura, T. Kodama, R. Kokoulin, M. Kossov, H. Kurashige, E. Lamanna, T. Lampién, V. Lara, V. Lefebure, F. Lei, M. Liendl, W. Lockman, F. Longo, S. Magni, M. Maire, E. Medernach, K. Minamimoto, P. Mora de Freitas, Y. Morita, K. Murakami, M. Nagamatu, R. Nartallo, P. Nieminen, T. Nishimura, K. Ohtusbo, M. Okamura, S. O’Neale, Y. Oohata, K. Paech, J. Perl, A. Pfeiffer, M. G. Pia, F. Ranjard, A. Rybin, S. Sadilov, E. Di Salvo, G. Santin, T. Sasaki, N. Savvas, Y. Sawada, S. Scherer, S. Sei, V. Sirotenko, D. Smith, N. Starkov, H. Stoecker, J. Sulkimo, M. Takahata, S. Tanaka, E. Tcherniaev, E. Safai Tehrani, M. Tropeano, P. Truscott, H. Uno, L. Urban, P. Urban, M. Verderi, A. Walkden, W. Wander, H. Weber, V. P. Wellisch, T. Wenaus, D. C. Williams, D. Wright, T. Yamada, H. Yoshida, and D. Zschesche. Geant4 - a simulation toolkit. *Nucl. Instrum. Meth. A*, 506:250–303, 2003.
- [39] M.J. Berger, J.H. Hubbell, S.M. Chang, J.S. Coursey, R. Sukumar, and D.S. Zucker. *XCOM: Photon Cross Section Database (version 1.3)*. National Institute of Standards and Technology, Gaithersburg, MD, 2005.
- [40] K. Alder and R. M. Steffen. Emission of gamma radiation and nuclear structure. In J.D. Hamilton, editor, *The electromagnetic interaction in nuclear spectroscopy*, pages 39–54. North-Holland, Amsterdam, 1975.
- [41] P. M. Endt. Strengths of gamma-ray transitions in  $a = 6-44$  nuclei (iii). *Atomic Data and Nuclear Data Tables*, 23:3 – 61, 1979.
- [42] P. J. Twin. Gamma ray angular distribution and correlation measurements (ii) experimental methods following nuclear reactions. In J.D. Hamilton, editor, *The electromagnetic interaction in nuclear spectroscopy*, chapter 15, pages 701–733. North-Holland, Amsterdam, 1975.
- [43] H. Olliver, T. Glasmacher, and Andrew E. Stuchbery. Angular distributions of  $\gamma$  rays with intermediate-energy beams. *Phys. Rev. C*, 68:044312, 2003.
- [44] Andrew E. Stuchbery.  $\gamma$ -ray angular distributions and correlations after projectile-fragmentation reactions. *Nucl. Phys. A*, 723:69–92, 2003.

- [45] O. Klein and Y. Nishina. über die Streuung von Strahlung durch freie Elektronen nach der neun relativistischen Quantendynamik von Dirac. *Z. Phys.*, 52:853, 1929.
- [46] Y. Nishina. Die Polarisation der Comptonstreuung nach der Diracschen Theorie des Elektrons. *Z. Phys.*, 52:869, 1929.
- [47] W. Heitler. *The Quantum Theory of Radiation*. Oxford University Press, London, 1944.
- [48] L. S. Fagg and S. S. Hanna. Polarization measurements on nuclear gamma rays. *Rev. Mod. Phys.*, 31:711–758, 1959.
- [49] A. von der Werth, F. Becker, J. Eberth, S. Freund, U. Hermkens, T. Mylaeus, S. Skoda, H. G. Thomas, and W. Teichert. Two Compton polarimeter constructions for modern standard  $\gamma$ -spectroscopy. *Nucl. Instrum. Meth. A*, 357:458 – 466, 1995.
- [50] G. Duchêne, F. A. Beck, P. J. Twin, G. de France, D. Curien, L. Han, C. W. Beausang, M. A. Bentley, P. J. Nolan, and J. Simpson. The clover: a new generation of composite Ge detectors. *Nucl. Instrum. Meth. A*, 432:90 – 110, 1999.
- [51] B. Schlitt, U. Maier, H. Friedrichs, S. Albers, I. Bauske, P. von Brentano, R.D. Heil, R.-D. Herzberg, U. Kneissl, J. Margraf, H.H. Pitz, C. Wesselborg, and A. Zilges. A sectored Ge-Compton polarimeter for parity assignments in photon scattering experiments. *Nucl. Instrum. Meth. A*, 337:416 – 426, 1994.
- [52] D. Miller, A. Chester, V. Moeller, K. Starosta, C. Vaman, and D. Weisshaar. Linear polarization sensitivity of SeGA detectors. *Nucl. Instrum. Meth. A*, 581:713–718, 2007.
- [53] G. D. Jones. Calibration of Compton polarimeters. *Nucl. Instrum. Meth. A*, 491:452–459, 2002.
- [54] W. F. Mueller, J. A. Church, T. Glasmacher, D. Gutknecht, G. Hackman, P.G. Hansen, Z. Hu, K. L. Miller, and C. Quirin. Thirty-two fold segmented germanium detectors to identify  $\gamma$ -rays from intermediate-energy exotic beams. *Nucl. Instrum. Meth. A*, 466:492–498, 2001.
- [55] O. Wieland, F. Camera, B. Million, A. Bracco, and J. van der Marel. Pulse distributions and tracking in segmented detectors. *Nucl. Instrum. Meth. A*, 487:441 – 449, 2002.
- [56] O.B. Tarasov and D. Bazin. LISE++: Radioactive beam production with in-flight separators. *Nucl. Instrum. Meth. B*, 266:4657 – 4664, 2008. Proceedings of the XVth International Conference on Electromagnetic Isotope Separators and Techniques Related to their Applications.

- [57] Jens Lindhard and Allan H. Sorensen. Relativistic theory of stopping for heavy ions. *Phys. Rev. A*, 53:2443–2456, 1996.
- [58] Z. Hu, T. Glasmacher, W.F. Mueller, and I. Wiedenhöver. An automatic energy-calibration method for segmented germanium detectors. *Nucl. Instrum. Meth. A*, 482:715–719, 2002.
- [59] R. Venturelli, D. Bazzaco, M. Bellato, A. Pullia, and Th. Kröll. Fold-dependent energy correction in segmented germanium detectors. In *LNL Annual Report 2002, INFN-LNL (REP)*, volume 198, pages 156–157. 2003.
- [60] F. Falk, A. Linnfors, B. Orre, and J.E. Thun. Alpha-gamma angular correlation and hyperfine interaction in the decay of  $^{249}_{98}\text{Cf}$ . *Phys. Scripta*, 1:13–19, 1970.
- [61] B.A. Logan, R.T. Jones, and A. Ljubičić. A figure of merit for gamma-ray polarimeters. *Nucl. Instrum. Meth.*, 108:603 – 604, 1973.
- [62] J. Simpson, P.A. Butler, and L.P. Ekström. Application of a sectored Ge(Li) detector as a Compton polarimeter. *Nucl. Instrum. Meth.*, 204:463 – 469, 1983.
- [63] K. Starosta, T. Morek, Ch. Droste, S. G. Rohoziński, J. Srebrny, A. Wierzchucka, M. Bergström, B. Herskind, E. Melby, T. Czosnyka, and P. J. Napiorkowski. Experimental test of the polarization direction correlation method (PDCO). *Nucl. Instrum. Meth. A*, 423:16 – 26, 1999.
- [64] M. Devlin, L. G. Sobotka, D. G. Sarantites, and D. R. LaFosse. Simulated response characteristics of Gammasphere. *Nucl. Instrum. Meth. A*, 383:506 – 512, 1996.
- [65] H. Mach, L. M. Fraile, O. Tengblad, R. Boutami, C. Jollet, W. A. Plóciennik, D. T. Yordanov, M. Stanoiu, M. J. G. Borge, P. A. Butler, J. Cederkäll, Ph. Dessagne, B. Fogelberg, H. Fynbo, P. Hoff, A. Jokinen, A. Korgul, U. Köster, W. Kurcewicz, F. Marechal, T. Motobayashi, J. Mrazek, G. Neyens, T. Nilsson, S. Pedersen, A. Poves, B. Rubio, E. Ruchowska, and the ISOLDE Collaboration. New structure information on  $^{30}\text{Mg}$ ,  $^{31}\text{Mg}$ , and  $^{32}\text{Mg}$ . *Eur. Phys. A*, 25:105–109, 2005.
- [66] G. Klotz, P. Baumann, M. Bounajma, A. Huck, A. Knipper, G. Walter, G. Marguier, C. Richard-Serre, A. Poves, and J. Retamosa. Beta decay of  $^{31,32}\text{Na}$  and  $^{31}\text{Mg}$ : Study of the  $N = 20$  shell closure. *Phys. Rev. C*, 47:2502–2516, 1993.
- [67] M. Kimura. Intruder features of  $^{31}\text{Mg}$  and the coexistence of many-particle and many-hole states. *Phys. Rev. C*, 75:041302(R), 2007.
- [68] I.-Y. Lee, J.T. Anderson, J. Bercovitz, A. Biocca, J. Comins, M. Cromaz, M. Descovich, D. Doering, P. Fallon, J.M. Joseph, C. Larsen, C. Lionberger, T. Loew, A.O. Macchiavelli, J. Pavan, D. Peterson, D. Radford, B.A. Savnik, C. Timossi, S. Virostek, H. Yaver, and S. Zimmermann. Greta white paper for

the 2007 nsac long range plan. Technical report, GRETINA Physics Working Group, 2007.

- [69] S. Nummela, F. Nowacki, P. Baumann, E. Caurier, J. Cederkäll, S. Courtin, P. Dessagne, A. Jokinen, A. Knipper, G. Le Scornet, L. G. Lyapin, Ch. Miehé, M. Oinonen, E. Poirier, Z. Radivojevic, M. Ramdhane, W. H. Trzaska, G. Walter, J. Äystö, and ISOLDE Collaboration. Intruder features in the island of inversion: The case of  $^{33}\text{Mg}$ . *Phys. Rev. C*, 64:054313, 2001.
- [70] B. V. Pritychenko, T. Glasmacher, P. D. Cottle, R. W. Ibbotson, K. W. Kemper, L. A. Riley, A. Sakharuk, H. Scheit, M. Steiner, and V. Zelevinsky. Structure of the "island of inversion" nucleus  $^{33}\text{Mg}$ . *Phys. Rev. C*, 65:061304, 2002.
- [71] Z. Elekes, Zs. Dombrádi, A. Saito, N. Aoi, H. Baba, K. Demichi, Zs. Fülöp, J. Gibelin, T. Gomi, H. Hasegawa, N. Imai, M. Ishihara, H. Iwasaki, S. Kanno, S. Kawai, T. Kishida, T. Kubo, K. Kurita, Y. Matsuyama, S. Michimasa, T. Minemura, T. Motobayashi, M. Notani, T. Ohnishi, H. J. Ong, S. Ota, A. Ozawa, H. K. Sakai, H. Sakurai, S. Shimoura, E. Takeshita, S. Takeuchi, M. Tamaki, Y. Togano, K. Yamada, Y. Yanagisawa, and K. Yoneda. Proton inelastic scattering studies at the borders of the "island of inversion":  $^{30,31}\text{Na}$  and  $^{33,34}\text{Mg}$  case. *Phys. Rev. C*, 73:044314, 2006.
- [72] P. Himpe, G. Neyens, D.L. Balabanski, G. Bélier, J.M. Daugas, F. de Oliveira Santos, M. De Rydt, K.T. Flanagan, I. Matea, P. Morel, Yu.E. Penionzhkevich, L. Perrot, N.A. Smirnova, C. Stodel, J.C. Thomas, N. Vermeulen, D.T. Yordanov, Y. Utsuno, and T. Otsuka.  $g$  factor of the exotic  $N = 21$  isotope  $^{34}\text{Al}$ : probing the  $N = 20$  and  $N = 28$  shell gaps at the border of the "island of inversion". *Phys. Lett. B*, 658:203 – 208, 2008.
- [73] J. Tostevin. personal communication.
- [74] M. Robinson, P. Halse, W. Trinder, R. Anne, C. Borcea, M. Lewitowicz, S. Lukyanov, M. Mirea, Yu. Oganessian, N. A. Orr, Yu. Penionzhkevich, M. G. Saint-Laurent, and O. Tarasov. New isomer  $^{32}\text{Al}^m$ . *Phys. Rev. C*, 53:R1465–R1468, 1996.
- [75] J. Dechargé and D. Gogny. Hartree-Fock-Bogolyubov calculation with the  $D1$  effective interaction on spherical nuclei. *Phys. Rev. C*, 21:1568–1593, 1980.
- [76] H. Ueno, D. Kameda, G. Kijima, K. Asahi, A. Yoshimi, H. Miyoshi, G. Kato, D. Nagae, S. Emori, T. Haseyama, H. Watanabe, and M. Tsukui. Magnetic moments of  $^{30}_{13}\text{Al}_{17}$  and  $^{32}_{13}\text{Al}_{19}$ . *Phys. Lett. B*, 615:186–192, 2005.
- [77] A. Gade, P. Adrich, D. Bazin, M. D. Bowen, C. M. Campbell, J. M. Cook, T. Glasmacher, P. G. Hansen, K. Hosier, S. McDaniel, D. McGlinchery,

- A. Obertelli, K. Siwek, L. A. Riley, J. A. Tostevin, and D. Weissarr. Reduction of spectroscopic strength: Weakly-bound and strongly-bound single-particle states studied using one-nucleon knockout reactions. *Phys. Rev. C*, 77:044306, 2008.
- [78] G. Audi, A. H. Wapstra, and C. Thibault. 2003 atomic mass evaluation (ii). tables, graphs and references. *Nucl. Phys. A*, 729:337–676, 2003.
- [79] V. Tripathi, S. L. Tabor, P. Bender, C. R. Hoffman, Sangjin Lee, K. Pepper, M. Perry, P. F. Mantica, J. M. Cook, J. Pereira, J. S. Pinter, J. B. Stoker, D. Weisshaar, Y. Utsuno, and T. Otsuka. Excited intruder states in  $^{32}\text{Mg}$ . *Phys. Rev. C*, 77:034310, 2008.
- [80] C. M. Mattoon, F. Sarazin, G. Hackman, E. S. Cunningham, R. A. E. Austin, G. C. Ball, R. S. Chakrawarthy, P. Finlay, P. E. Garrett, G. F. Grinyer, B. Hyland, K. A. Koopmans, J. R. Leslie, A. A. Phillips, M. A. Schumaker, H. C. Scraggs, J. Schwarzenberg, M. B. Smith, C. E. Svensson, J. C. Waddington, P. M. Walker, B. Washbrook, and E. Zganjar.  $\beta$  decay of  $^{32}\text{Na}$ . *Phys. Rev. C*, 75:017302, 2007.
- [81] G. Neyens, N. Coulier, S. Ternier, K. Vyvey, S. Michiels, R. Coussement, D. L. Balabanski, J. M. Casandjian, M. Chartier, D. Cortina-Gil, M. Lewitowicz, W. Mittig, A. N. Ostrowski, P. Roussel-Chomaz, N. Alamanos, and A. Lépine-Szily. Nuclear spin alignment and static moments of light projectile fragments measured with the level mixing resonance (LMR) method. *Phys. Lett. B*, 393:36–41, 1997.
- [82] Aage Bohr and Ben R. Mottelson. *Nuclear Structure*, volume 2. World Scientific, Singapore, 3rd edition, 1998.
- [83] J. Retamosa, E. Caurier, F. Nowacki, and A. Poves. Shell model study of the neutron-rich nuclei around  $N = 28$ . *Phys. Rev. C*, 55:1266–1274, 1997.
- [84] S. Nummela, P. Baumann, E. Caurier, P. Dessagne, A. Jokinen, A. Knipper, G. Le Scornet, C. Miehé, F. Nowacki, M. Oinonen, Z. Radivojevic, M. Ramdhane, G. Walter, and J. Äystö. Spectroscopy of  $^{34,35}\text{Si}$  by  $\beta$  decay: *sd-fp* shell gap and single-particle states. *Phys. Rev. C*, 63:044316, 2001.
- [85] Ikuko Hamamoto. Nilsson diagrams for light neutron-rich nuclei with weakly-bound neutrons. *Phys. Rev. C*, 76:054319, 2007.
- [86] J. Simpson, J. Nyberg, W. Korten, et al. Agata technical design report. Technical report, AGATA Collaboration, 2008.
- [87] Dino Bazzacco. The advanced gamma ray tracking array AGATA. *Nucl. Phys. A*, 746:248 – 254, 2004. Proceedings of the Sixth International Conference on Radioactive Nuclear Beams (RNB6).

- [88] W. Hennig, H. Tan, M. Walby, P. Grudberg, A. Fallu-Labruyere, W.K. Warburton, C. Vaman, K. Starosta, and D. Miller. Clock and trigger synchronization of digital data acquisition modules. *Nucl. Instrum. Meth. B*, 261:1000–1004, 2007.
- [89] H. Tan, W. Hennig, M. Walby, A. Fallu-Labruyere, J. Harris, D. Breus, P. Grudberg, W.K. Warburton, C. Vaman, T. Glasmacher, P. Mantica, D. Miller, K. Starosta, and P. Voss. Digital data acquisition modules for instrumenting large segmented germanium detector arrays. In *Nuclear Science Symposium Conference Record, 2008*, page 3196. IEEE, 2008.
- [90] Zhong He. Review of the Shockley-Ramo theorem and its application in semiconductor gamma-ray detectors. *Nucl. Instrum. Meth. A*, 463:250–267, 2001.
- [91] K. Starosta, C. Vaman, D. Miller, P. Voss, H. Crawford, D. Bazin, T. Glasmacher, P. Mantica, H. Tan, W. Hennig, M. Walby, A. Fallu-Labruyere, J. Harris, D. Breus, P. Grudberg, and K. Warburton. Digital data acquisition system for experiments with segmented detectors at National Superconducting Cyclotron Laboratory. In preparation.
- [92] M.A. Omar and L. Reggiani. Drift velocity and diffusivity of hot carriers in germanium: Model calculations. *Solid-State Electronics*, 30:1351–1354, 1987.
- [93] I.-Y. Lee. GRETINA technical note: electron and hole drift velocity in Ge. Technical Report GRT-6-061112, GRETINA physics working group, 2006.
- [94] L. Mihailescu, W. Gast, R. M. Lieder, H. Brands, and H. Jäger. The influence of anisotropic electron drift velocity on the signal shapes of closed-end HPGe detectors. *Nucl. Instrum. Meth. A*, 447:350 – 360, 2000.
- [95] N.J. Hammond, T. Duguet, and C.J. Lister. Ambiguity in gamma-ray tracking of “two-interaction” events. *Nucl. Instrum. Meth. A*, 547:535 – 540, 2005.
- [96] G. J. Schmid, M. A. Deleplanque, I. Y. Lee, F. S. Stephens, K. Vetter, R. M. Clark, R. M. Diamond, P. Fallon, A. O. Macchiavelli, and R. W. MacLeod. A  $\gamma$ -ray tracking algorithm for the GRETA spectrometer. *Nucl. Instrum. Meth. A*, 430:69 – 83, 1999.
- [97] L. Milechina and B. Cederwall. Improvements in  $\gamma$ -ray reconstruction with positive sensitive Ge detectors using the backtracking method. *Nucl. Instrum. Meth. A*, 508:394 – 403, 2003.
- [98] I. Piqueras, F. A. Beck, E. Pachoud, and G. Duchne. A probabilistic  $\gamma$ -ray tracking method for germanium detectors. *Nucl. Instrum. Meth. A*, 516:122 – 133, 2004.
- [99] D.-C. Dinca. *Study of the development of shell closures at  $N = 32, 34$  and approaches to sub-segment interaction-point determination in 32-fold segmented high-purity germanium detectors*. PhD thesis, Michigan State University, 2005.



- [100] T. Ahn. Digital signal processing for germanium detectors. Master's thesis, SUNY, Stony Brook, 2004.
- [101] M. Descovich, I.Y. Lee, P. Fallon, M. Cromaz, A.O. Macchiavelli, D.C. Radford, K. Vetter, R.M. Clark, M.A. Deleplanque, F.S. Stephens, and D. Ward. In-beam measurement of the position resolution of a highly segmented coaxial germanium detector. *Nucl. Instrum. Meth. A*, 553:535 – 542, 2005.
- [102] FRIB: MSU/FRIB proposal. <http://frib.msu.edu/about/msu-frib-proposal>, 2009.
- [103] K.S. Krane. In N.J. Stone and H. Postma, editors, *Low-temperature Nuclear Orientation*, chapter 2. Elsevier Science, Amsterdam, 1986.
- [104] T. Yamazaki. Tables of coefficients for angular distribution of gamma rays from aligned nuclei. *Nuclear Data Sheets. Section A*, 3:1 – 23, 1967.
- [105] R. M. Diamond, E. Matthias, J. O. Newton, and F. S. Stephens. Nuclear alignment in heavy-ion reactions. *Phys. Rev. Lett.*, 16:1205–1207, 1966.
- [106] K. Alder and A. Winther. *Electromagnetic Excitation Theory of Coulomb Excitation with Heavy Ions*. North-Holland, Amsterdam, 1975.
- [107] A.H. Wapstra. *Nuclear spectroscopy tables*. North-Holland, Amsterdam, 1959.